Spring 5-2021

Modeling, Design, and Fabrication of Plasmonic Coupling to a Silicon Nitride Waveguide-Photodetector

Jaehoon Jeong

Modeling, Design, and Fabrication of Plasmonic Coupling to a Silicon Nitride

Waveguide-Photodetector

A Thesis

Submitted to the Faculty

of

Rose-Hulman Institute of Technology

by

Jaehoon Jeong

In Partial Fulfillment of the Requirements for the Degree

of

Master of Science in Optical Engineering

May 2021

ROSE-HULMAN INSTITUTE OF TECHNOLOGY

Final Examination Report

Jaehoon Jeong

Name

Optical Engineering

Graduate Major

Thesis Title Modeling, Design, and Fabrication of Plasmonic Coupling to a Silicon Nitride

Waveguide-Photodetector

DATE OF EXAM: July 6, 2021

EXAMINATION COMMITTEE:

	Thesis Advisory Committee	Department
Thesis Advisor:	Azad Siahmakoun	PHOE
	Hoseein Alisafaee	PHOE
	Dong Hwan Kim	SNUST

PASSED _____X_____   FAILED _____

ABSTRACT

Jeong, Jaehoon

M.S.O.E.

Rose-Hulman Institute of Technology

May 2021

Modeling, Design, and Fabrication of Plasmonic Coupling to a Silicon Nitride Waveguide-Photodetector

Thesis Advisor: Dr. Azad Siahmakoun

This paper reports an evanescent coupling to silicon nitride-Germanium (SiN-Ge) photodetectors using surface plasmon polaritons (SPPs). Modeling, design, and fabrication of plasmonic coupling to Al nanoscale metal and light detection are included. Since 10 % of light coupled with surface plasmons is detected from poly-Si waveguides using lens fiber, Ge-photodetectors and SiN waveguides are utilized to detect light around 1550 nm wavelength with less insertion loss. Two plasmonic configurations with either Ag or Al nanoscale metal are simulated and analyzed using Lumerical FDTD simulation. Difficulty during fabricating SiN-Ge photodetectors are mentioned, and the best design and fabrication are suggested. The results in this paper can be applied to the design and fabrication of plasmonic systems with SiN-Ge photodetectors.

Keywords: Design, Modeling, Fabrication, Plasmonics, Surface Plasmon Polaritons, Plasmons, Nanoscale Metal, Photodetector, Photodiode, Lumerical

To my family . . .

ACKNOWLEDGEMENTS

TABLE OF CONTENTS

Contents

LIST OF FIGURES

LIST OF TABLES

LIST OF ABBREVIATIONS

BOE	Buffered Oxide Etch
BOX	Buried Oxide Layer
DI	Deionized
DWDM	Dense Wavelength Division Multiplexing
EM	Electro-Magnetic
EDFA	Erbium Doped Fiber Amplifier
FDTD	Finite-Difference Time-Domain
HF	Hydrofluoric Acid
IC	Integrated Circuit
MSE	Mean Squared Error
MZI	Mach-Zehnder Interferometer
PCB	Printed Curcuit Board
PM	Polarization Maintaining
PR	Photoresist
SOI	Silicon on Insulator
SPP	Surface Plasmon Polariton
TE	Transverse Electric
TIR	Total Internal Reflection
TM	Transverse Magnetic

LIST OF SYMBOLS

English Symbols

$\boldsymbol{E}$	Electric Field Vector
$\boldsymbol{H}$	Magnetic Field Vector
$\boldsymbol{D}$	Electric Displacement Vector
$\boldsymbol{B}$	Magnetic Induction Vector
$\boldsymbol{J}$	Electric Current Density
c	Speed of Light in Vacuum
t	Time
k_0	Wave Number
$\boldsymbol{k_x}$	Propagation Constant in x Direction
$\boldsymbol{k_d}$	Propagation Constant in Vertical Direction toward Dielectric
$\boldsymbol{k_m}$	Propagation Constant in Vertical Direction toward Metal
$\hbar$	Reduced Plank Constant
p	Momentum of a Photon
$\bar{r}$	Cartesian Coordinate Arbitrary Vector
i	Imaginary Unit
a_1, a_2	Field Amplitude of TE Mode
b_1, b_2	Field Amplitude of TM Mode

Greek Symbol

ε	Electric Permittivity
ε_0	Electric Permittivity in Vacuum
ε_r	Electric Relative Permittivity

ε_d	Electric Relative Permittivity in Dielectric
ε_m	Electric Relative Permittivity in Metal
μ_0	Magnetic Permeability in Vacuum
λ	Wavelength
ω	Angular Frequency
β	Propagation Constant

1. INTRODUCTION

Plasmonics is a research area that is actively studied and has much potential for improving the performance of devices. Plasmonic effects can be used to develop high-performance sensors, circuits, displays, and so forth [1].

Surface plasmon resonance (SPR) is one of the plasmonic effects and is classified into two groups. One group is surface plasmon polaritons (SPPs) propagating on nanoscale metal, and the other is localized SPR with metallic particles. The propagation length of SPP spans from a few nanometers to centimeters depending on materials. Light's penetration lengths into metals depend on materials and determine the minimum sizes of plasmonic devices [1]. Typical materials to excite SPP are silver and aluminum.

Silicon photonic integrated circuits (SPIC) achieves the lowest power consumption, delivering high performance in loss, bandwidth, and efficiency [2]. Researchers have developed high-performance photodetectors to detect light carried by waveguides or metals, absorbed into the intrinsic region, and then generate electron-hole pairs [3]. Among various configurations of photodiodes, Ge-photodiode is the one that shows cutting-edge performance, can be easily integrated with other silicon-on-insulator (SOI) components, and are compatible with transistor processes and tools [3].

Germanium has more free electrons, a higher refractive index, and greater absorption coefficients than silicon at a given temperature, as shown in Figure 1.1 [4]. As mentioned, germanium can be utilized in photodetectors, solar cells, and light-emitting diode (LED) [5]. However, germanium is challenging to handle, as it is vaporized when it interacts with oxygen at low temperatures. Therefore, spin-on-dopants are needed to fabricate photodetectors in PIN configuration [6]. Spin-

on-dopants help dope germanium and fabricate PIN Ge-photodiodes with lower dark current than metal-semiconductor-metal (MSM) photodetectors [3]. Most of all, PIN Ge-photodiodes facilitate efficient carrier collection and high bandwidth with low bias voltage, which MSM photodetectors cannot to achieve [3]. PIN photodetectors are classified into two types, as shown in Figure 1.2 [7]. Vertical PIN photodetector's dark current and responsivity are low since current travel across the germanium and silicon layers. A higher voltage is required for lateral PIN photodetector to sweep carriers out of the intrinsic region [7].

The base layer of PIN photodetectors is generally made of Si. However, silicon nitride (Si_3N_4 or is short SiN) can be used instead of Si. Si_3N_4 is a chemical compound of silicon and nitrogen. It is a very stable ceramic material that has been used to prevent ions from dissipating into the semi-conductor surface as a passivation layer in the semiconductor industry. Silicon nitride insulator shows higher performance than silicon oxide, which can be used as another insulator [9]. Films of SiN typically have high stresses and are deposited on a silicon oxide layer to reduce stresses to prevent cracking wafers. Due to complications during fabrication, SiN is challenging to handle
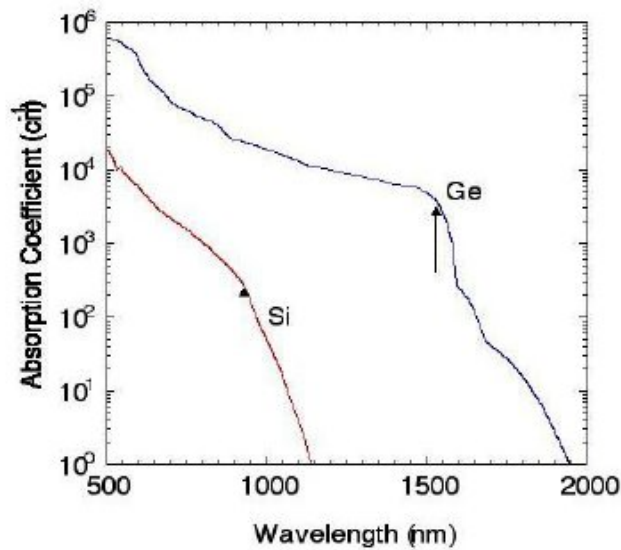
Figure 1.1: Absorption coefficients of Si and Ge. [4]

(a)

(b)
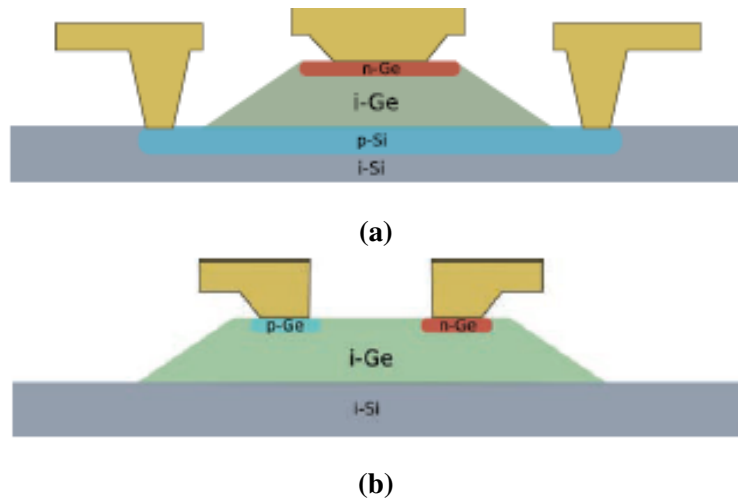
Figure 1.2: (a) Vertical and (b) Lateral PIN photodetectors. [7]
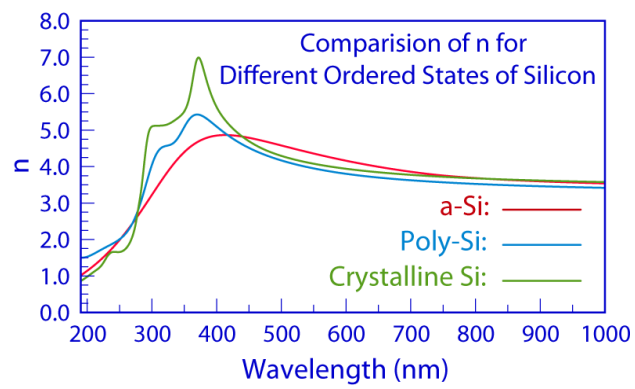
(a)
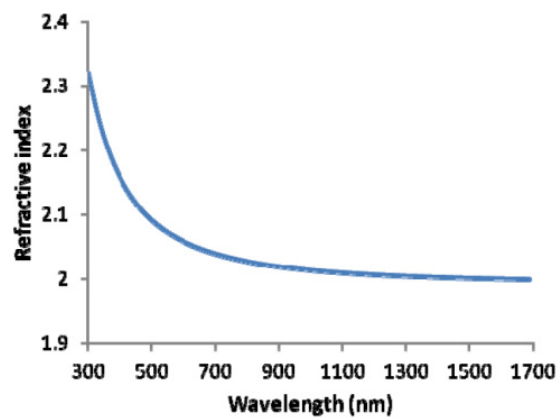
(b)

Figure 1.3: (a) Refractive indices of a-Si, Poly-Si, and Crystalline-Si and (b) Silicon nitride. [8]

since films of SiN react with oxygen gas and convert into silicon oxide [10]. Amorphous SiN can be p-doped with CVD or PECVD, using aluminum powder or boron, respectively [11], [12]. The refractive indices of a-Si, poly-Si, and crystalline-Si are larger than the refractive index of silicon nitride at around 1550 nm, as shown in Figure 1.3 [8].

In addition to the above features, SiN waveguide platforms, which demonstrate transmission over a wide wavelength range of 400-2350 nm, exhibit low-loss ($\leq$1 dB/m) integrated devices leading to high optical power and reducing power consumption [2]. As shown in Figure 1.4, SiN waveguides are compared with Silicon-on-insulator (SOI) and InP waveguides [2]. Therefore, SiN waveguide platforms are considered the next generation of SOI and III-V photonics [2].

Plasmonic effects, PIN Ge-photodiodes, and SiN waveguides are promising to develop state-of-the-art integrated devices in the future. This thesis covers the modeling, design, and fabrication of integrated devices, including the elements mentioned. Simulations of PIN Ge-photodiodes comparing two geometries and plasmonic coupling utilizing nanofilms of Ag or Al are reported in the Theory and Simulation chapter. The simulation aim is to design and model feasible devices which can be fabricated in the cleanroom. Fabrication processes for the integrated devices are reported in
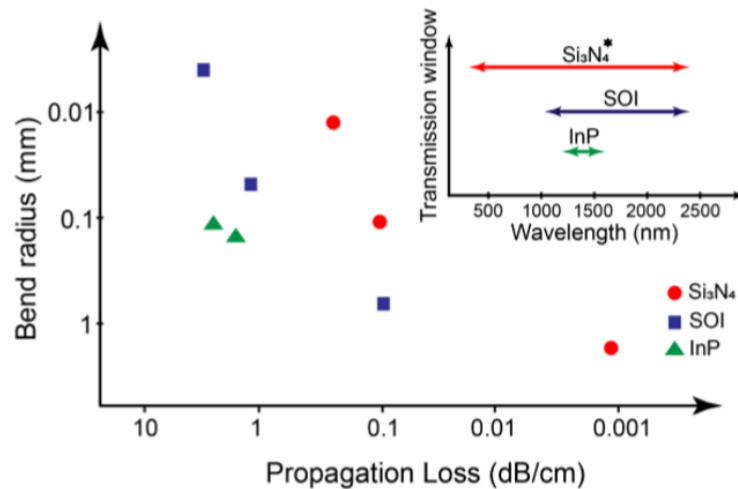
Figure 1.4: Comparison of propagation loss (dB/cm) in SiN, SOI, and InP. [2]

the Fabrication chapter. Characteristics of Ge and SiN and fabrication errors are explained. Testing

of the fabricated SiPh devices are covered in the Characterization of PIC chapter.

2. THEORY AND SIMULATION

2.1. Photodetectors

The photodetector converts photons (optical signal) into electrons (electrical signal). Silicon is not a good material to absorb light at telecommunication wavelengths, but germanium efficiently absorbs light in the NIR wavelength range. The NIR wavelength range is from 750 nm to 1500 nm. Therefore, this thesis focuses on the germanium photodetector with high responsivity and speed [7].

Three parameters influencing photodetectors' performance are responsivity, 3dB bandwidth, and dark current. The responsivity quantifies how much electrical current is produced per unit optical power (optical signal) over wavelength. The bandwidth is the second parameter and shows how fast a photodetector can respond to varying optical signals. The last parameter is the dark current. The dark current is the current when there is no optical input. Unfortunately, the dark current can generate noise in photodetectors which can result in inaccurate measurements.

The responsivity denotes the conversion of the optical power into an electrical current. Therefore, the responsivity is the ratio of the electrical current to optical power (Amperes per watt, A/W):

$$R = \frac{I}{P}$$

(2.1)

Another essential parameter is quantum efficiency (η), which is similar to responsivity. Quantum efficiency means conversion efficiency from optical power to electrical power and can be used instead of responsivity.

The quantum efficiency of one means that one photon absorbed by a photodetector generates one pair of an electron and a hole. There is a relationship between quantum efficiency and responsivity, as shown in Equation 2.2 [7]. In Equation 2.2, η is the quantum efficiency, q is the charge of electron, λ is wavelength of light, h is Plank's constant, and c is the speed of light. Quantum efficiency can be determined by dividing the measured responsivity by the maximum responsivity:

$$R = \eta \frac{q\lambda}{hc}$$
(2.2)

Figures 2.1 and 2.2 are results of responsivity using the Lumerical Device simulation program. The responsivity increases at the bias voltage of 1V as the area of the germanium becomes larger. The germanium's size is not directly related with the responsivity, but the geometry was adjusted and the number of electron charges in germanium became increased. As shown in Equation 2.2, the responsivity is associated with the number of electron charges, and this is the reason that Figure 2.1 and 2.2 have different values at the bias voltage of 1V. The responsivity in Figure 2.1 is 1.24 A/W at the bias voltage of 1V. The geometry for the simulation in Figure 2.1 is 3.5 μm × 0.3 μm (width × thickness). The responsivity in Figure 2.2 is 1.75 A/W at the bias voltage of 1V. The geometry for the simulation in Figure 2.2 is 15.5 μm × 0.2 μm (width × thickness). The geometry for the simulation in Figure 2.2 is relatively larger than the ideal geometry, and the result is distinct from the one in Figure 2.1.

As mentioned, the bandwidth determines how fast photodetectors react to incident optical power. Two factors, transit time and RC response, affect the bandwidth [7]. The transit time is how long it takes for electrons-hole pairs generated by incident photons.

As shown in Table 2.1, the carrier mobility and saturation velocity are all different for each material. E and μ are the electrical field and the carrier mobility, respectively, in Equation 2.3 [7].

When the electrical field becomes stronger, the carriers move faster. However, they do not move any faster if they reach saturation velocity.

Saturation mobility can be determined using Table 2.1 and the electric field, as shown in equation 2.4 [7].
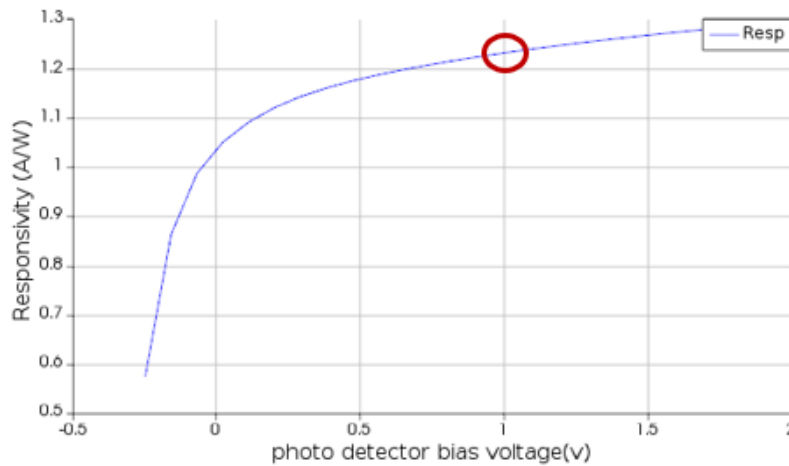
Figure 2.1: The ideal photodetector's responsivity was simulated. The germanium's geometry is $3.5\,\mu$m $\times$ $0.3\,\mu$m (width $\times$ thickness), and the light's wavelength is 1550 nm. The circle represents the responsivity is 1.24 A/W at the bias voltage of 1V.
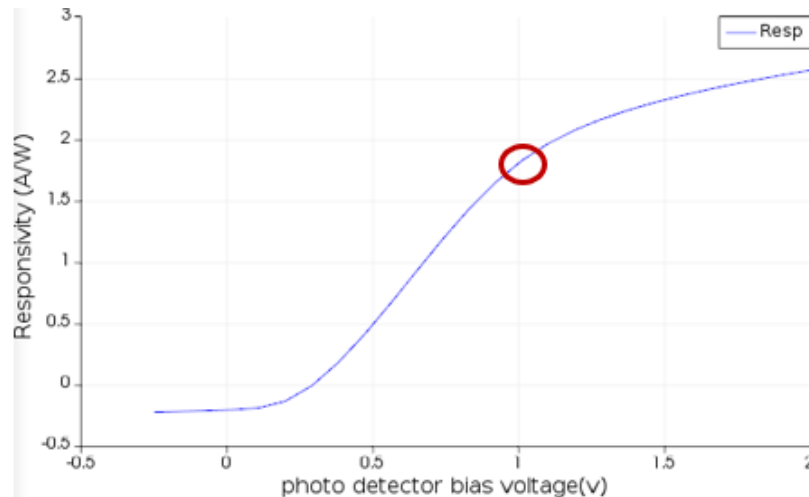
Figure 2.2: The large photodetector's responsivity was simulated. The germanium's geometry is $15.5\,\mu$m $\times$ $0.2\,\mu$m (width $\times$ thickness), and the light's wavelength is 1550 nm. The circle represents the responsivity is 1.75 A/W at the bias voltage of 1V.

	e$^-$ (Si)	h$^+$ (Si)	e$^-$ (Ge)	h$^+$ (Ge)
Mobility (cm^2/Vs)	1400	500	3900	1900
Sat. velocity (m/s)	1×10^5	0.7×10^5	0.7×10^5	0.63×10^5

Table 2.1: Mobility and saturation velocity [13].

$$v = \mu E$$
(2.3)

$$\mu_{sat} = \frac{\mu}{\sqrt{1 + \left(\frac{\mu E}{v_{sat}}\right)^2}}$$
(2.4)

The 3 dB bandwidth is the range of electrical frequencies that a photodetector supports. Therefore, the 3dB bandwidth should be measured to determine the performance of a photodetector. Figures 2.3 and 2.4 are the results of bandwidth using the Lumerical Device simulation program. The bandwidth in Figure 2.3 is between 10 GHz and 15 GHz. The geometry for the simulation in Figure 2.3 is $3.5\,\mu m \times 0.3\,\mu m$ (width $\times$ thickness). The bandwidth in Figure 2.4 is between 1 GHz and 1.5 GHz. The geometry for the simulation in Figure 2.4 is $15.5\,\mu m \times 0.2\,\mu m$ (width $\times$ thickness). The bandwidth decreases at the bias voltage of 1V as the area of the germanium becomes larger.

An equivalent circuit for a germanium photodetector is shown in Figure 2.5 [7]. Therefore, if C_{pd} = 40 pF, R_{pd} = 150 Ω, and R_{load} = 50 Ω are given, then τ_{RC} becomes 2 ps. Using those numbers, the frequency can be calculated as $f_{RC} = \frac{1}{2\pi RC} = 20 GHz$. If $f_{sat} = 0.38 \frac{v_{sat}}{h} = 60 GHz$ is given, the total bandwidth can be obtained using Equation 2.5:

$$f = \left(\frac{1}{f_{RC}^2} + \frac{1}{f_{transit}^2} \right)^{-\frac{1}{2}}$$

(2.5)

The dark current is considered an offset to the electric current. The dark current should be sub-
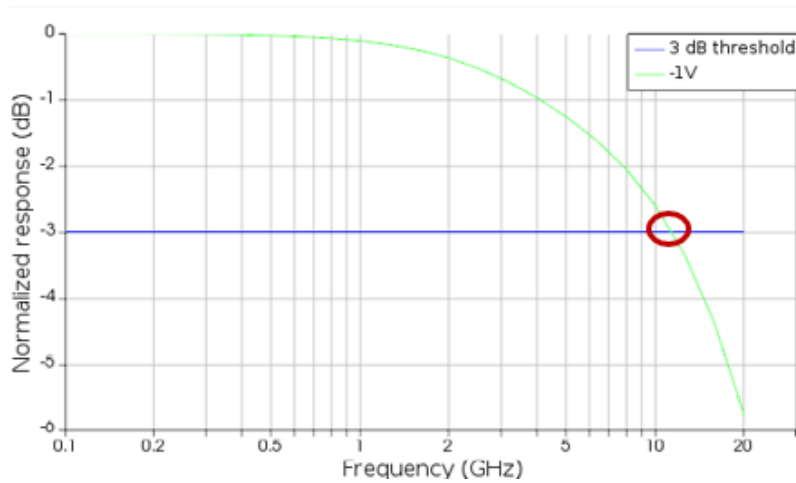
Figure 2.3: The ideal photodetector's 3dB bandwidth was simulated. The germanium's geometry is $3.5\,\mu\text{m} \times 0.3\,\mu\text{m}$ **(width $\times$ thickness), and the light's wavelength is 1550 nm. The circle represents the 3dB bandwidth is between 10GHz and 15GHz.**
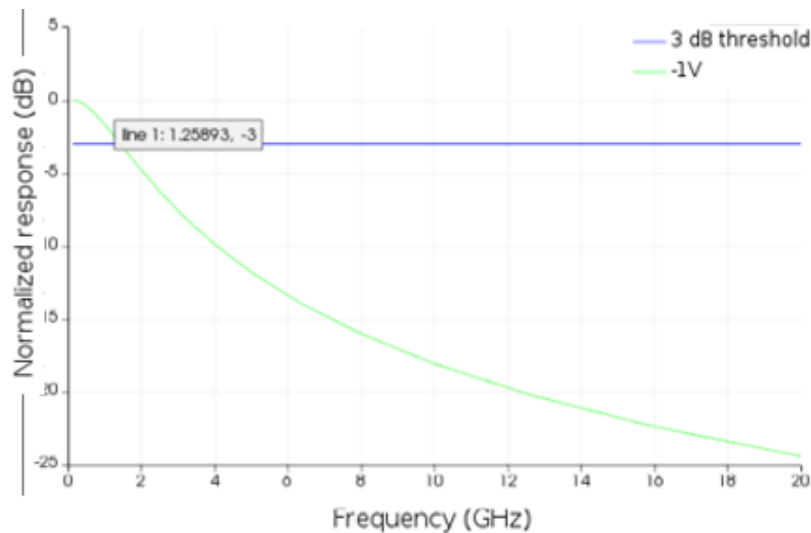
Figure 2.4: The large photodetector's 3dB bandwidth was simulated. The germanium's geometry is $15.5\,\mu\text{m} \times 0.2\,\mu\text{m}$ **(width $\times$ thickness), and light's wavelength is 1550 nm. The circle represents the 3dB bandwidth is between 1GHz and 1.5GHz.**

tracted from the total electric current. Both bulk generation and surface generation contribute to the

dark current. These two factors come from fabrication errors. In silicon-germanium photodiodes,

the lattice mismatch between silicon and germanium results in threading dislocations. The bulk

dark current is insignificant in the low electrical voltage. However, the bulk dark current becomes

higher as the voltage is raised. The surface generation comes from surface defects such as dangling

bonds. As seen in Equation 2.6 [7], the bulk dark current and surface generation contribute to the

dark current. The photodetector's area also contributes to the dark current.

$$I_{dark} = J_{bulk} \cdot A + J_{surf} \sqrt{4\pi} \sqrt{A}$$

(2.6)

Figures 2.6 and 2.7 are the results of dark current using the Lumerical Device simulation pro-

gram. The blue color means lower dark current than yellow and red colors. As the voltage in-

creases, the dark current becomes higher. As presented in equation 2.6, the area of germanium

contributes to the dark current. As the temperature increases, the dark current becomes higher.

Temperature influences the performance of photodetectors since electrons and holes come to move
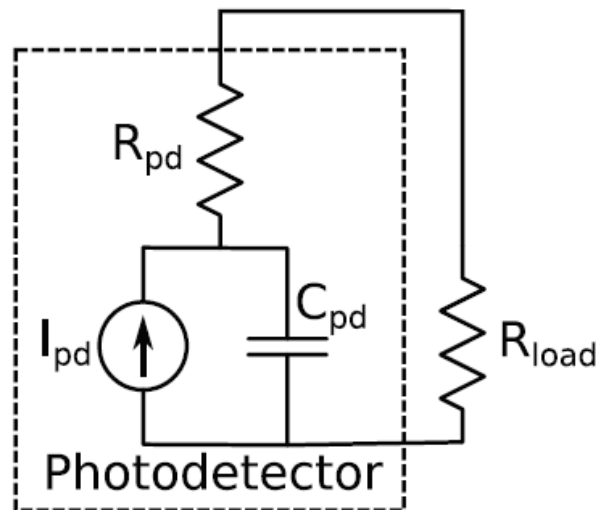
Figure 2.5: Equivalent circuit for the PIN photodetector [7].

faster as temperature increases. Comparing two Figures 2.6 and 2.7, the dark current increases at

the bias voltage of 1V as the area of the germanium becomes larger.
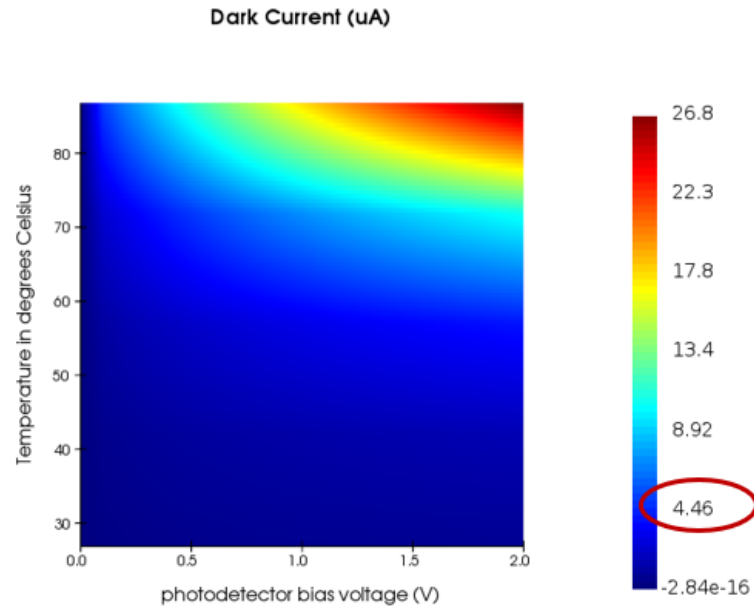
Figure 2.6: The ideal photodetector's dark current was simulated. The germanium's geometry is $3.5\,\mu\text{m} \times 0.3\,\mu\text{m}$ (width $\times$ thickness), and the light's wavelength is 1550 nm.
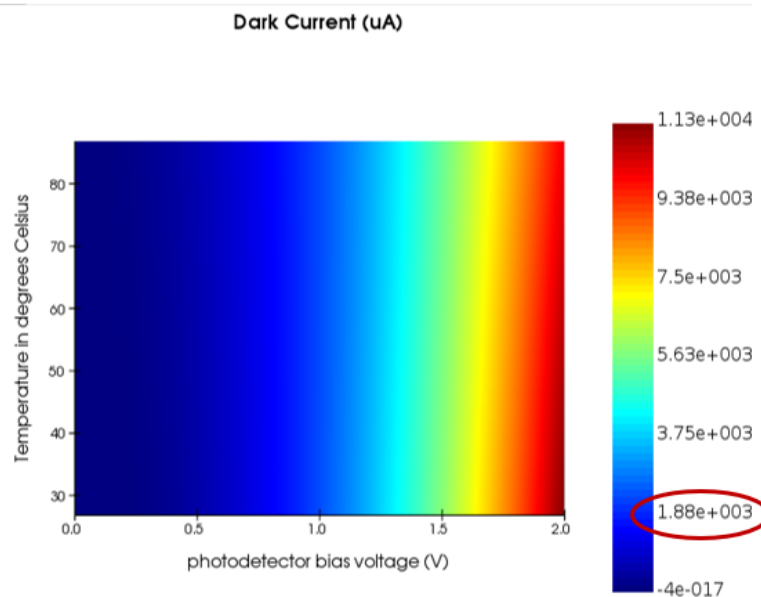
Figure 2.7: The large photodetector's dark current was simulated. The germanium's geometry is $15.5\,\mu\text{m} \times 0.2\,\mu\text{m}$ (width $\times$ thickness), and the light's wavelength is 1550 nm.

Figure 2.8 (a) describes that light is absorbed into the germanium layer from the silicon nitride layer. 60 % of optical power is transmitted into the germanium layer. Figure 2.8 (b) describes that the photodetector works in the range of telecommunication wavelength. Silicon can be used instead of germanium. However, the Si photodiode does not operate around 1550 nm wavelength.

The simulations' results expect that the dark current increases as the germanium's geometry become larger. The dark current linearly increases with the area of the germanium due to the bulk dark current, as shown in Equation 2.6. It was inevitable to design the germanium larger since the photolithography's resolution is $4\,\mu$m, and two electrodes should be made on the Ge layer. One suggestion to reduce the dark current is to design the germanium smaller to have width. The SiN base layer should have width. Each electrode for cathode and anode should be made on the germanium and SiN base layer, respectively. The suggestion's configuration is vertical PIN Ge-photodiode.

| (a) | (b) |
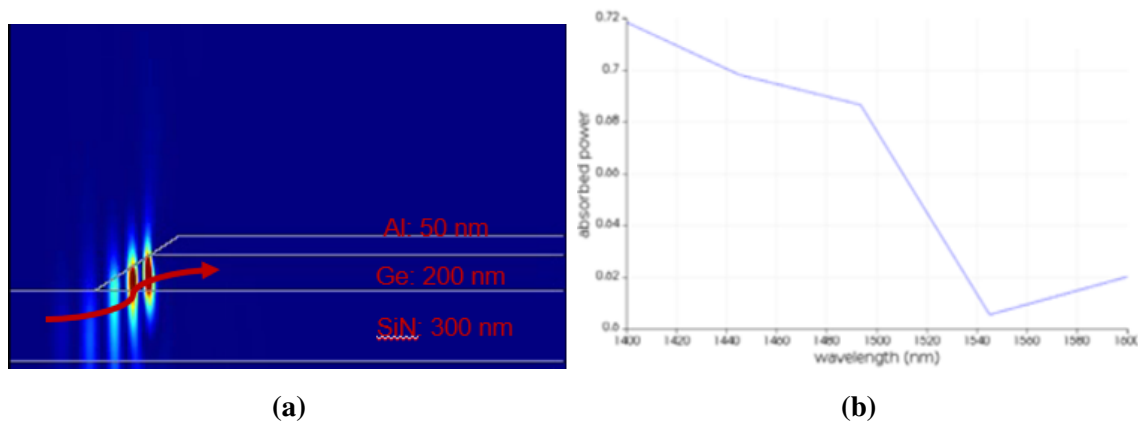
Figure 2.8: (a) Light is absorbed into the germanium layer from the silicon nitride layer. (b) At 1550 nm wavelength, 60 % of optical power is transmitted into the germanium layer.

2.2. Plasmonics

Plasmonics refers to the manipulation of signals generated between nanoscale metal and dielectric interfaces. As mentioned in the Introduction, the plasmonic effects are used for solid coupling and enhancing an original signal. SPPs are excited as a resonant reaction when light is coupled to plasmons at an angle with a prism. Plasmonics' equations start with Maxwell's equations.

E and B are electric and magnetic fields. The source of curl E is a magnetic induction alternating in time. Equation 2.7 describes that variation of the magnetic field induces the electric field.

$$\nabla \times \vec{E} = -\frac{\partial \vec{B}}{\partial t},$$

$$(2.7)$$

μ_0 and ε_0 are permeability and vacuum permittivity. ε_0 and μ_0 are $8.85 \times 10^{-12} F/m$ and $4\pi \times 10^{-7} H/m$, respectively. Equation 2.8 describes how the variation of an electric field induces a magnetic field.

$$\nabla \times \vec{B} = \mu_0 \vec{j} + \mu_0 \varepsilon_0 \frac{\partial \vec{E}}{\partial t},$$

$$(2.8)$$

$$\nabla \cdot \vec{E} = \frac{\rho}{\varepsilon_0},$$

$$(2.9)$$

ρ is charge density. Equation 2.10 describes that the magnetic field is a closed loop.

$$\nabla \cdot \vec{B} = 0$$

$$(2.10)$$

The electromagnetic field accumulates energy, and the density of the cumulated energy, ω, is

given by equation 2.11. When an electromagnetic field is not varied in time, the field is called a static field. When an electromagnetic field is varied in time, the field is called a homogeneous field. Equation 2.12 describes that Lorentz force is generated when a particle is put in an electromagnetic field.

$$\omega = \frac{\varepsilon_0 \vec{E}^2}{2} + \frac{\vec{B}^2}{2\mu_0}$$

(2.11)

$$\vec{F} = q \cdot \vec{E} + q \cdot \vec{v} \times \vec{B}$$

(2.12)

Equation 2.13 describes the Poynting vector representing the directional energy flux, the energy transfer per unit area per unit time, of an electromagnetic field.

$$\vec{S} = \frac{1}{\mu_0} \vec{E} \times \vec{B}$$

(2.13)

Equations 2.14 and 2.15 describe polarization and magnetization, which are defined as P and M, respectively. P and M represent electric and magnetic dipole moment density induced by either an external or a magnetic field. Permittivity and permeability are interaction parameters of electromagnetic waves and materials. In Equations 2.15 and 2.16, χ_e and χ_m are electric and magnetic susceptibility, respectively. Electric susceptibility can be obtained by adding permittivity to 1. D, called displacement field, is shown in Equations 2.16 can be obtained using vacuum permittivity, electric susceptibility, and electric field. Magnetic field strength designated by H is shown in Equation 2.17. Equation 2.18 describes that permittivity consists of real and imaginary parts: ε' and ε'' associated with polarization and losses, respectively. Those two parameters depend on frequency.

$$P(E) = P_0 + \varepsilon_0 \cdot \chi_e \cdot E + \varepsilon_0 \cdot \hat{\chi}_e^{(2)} \cdot E \otimes E + \cdots$$
$$(2.14)$$

$$M(H) = M_0 + \chi_m \cdot H + \cdots$$
$$(2.15)$$

$$D = \varepsilon_0 \cdot E + P$$
$$= \varepsilon_0 (1 + \chi_e) \cdot E$$
$$(2.16)$$

$$H = \frac{B}{\mu_0} - M$$
$$= \mu_0 (1 + \chi_m) \cdot H$$
$$(2.17)$$

$$\varepsilon = \varepsilon'(\omega) + i \cdot \varepsilon''(\omega)$$
$$(2.18)$$

The above equations are introduced to understand the features of light and materials. The interaction of light and materials can be understood after comprehending Maxwell's equations, polarization, and permittivity.

A plane wave is introduced to obtain the dispersion equation. The Plane wave has a translation symmetry along the y-direction, as shown in Figure 2.9. Therefore, the electromagnetic field in Figure 2.9 does not depend on the y-variable. The plain wave is described in Equation 2.19. Equations 2.19a and 2.19b are the 3rd and 4th Maxwell's equations. Equations 2.19e, 2.19f, and 2.19g describe that the electric field in Figure 2.9 varies in time, is independent of the y-direction, and propagates in the z-direction, respectively. Equations 2.19c and 2.19d describe an electric field

and a magnetic field propagating along the z-direction, respectively. $\mathscr{E}$ and $\mathscr{H}$ in Equations 2.19c and 2.19d are amplitude for plane waves.

$$\nabla \times \vec{H} = \frac{\partial \vec{D}}{\partial t} \tag{2.19a}$$

$$\nabla \times \vec{E} = -\frac{\partial \vec{B}}{\partial t} \tag{2.19b}$$

$$E(x,y,z,t) = \mathscr{E}(x) \cdot e^{-i \cdot \omega \cdot t + i \cdot k_z \cdot z} \tag{2.19c}$$

$$H(x,y,z,t) = \mathscr{H}(x) \cdot e^{-i \cdot \omega \cdot t + i \cdot k_z \cdot z} \tag{2.19d}$$

$$\frac{\partial}{\partial t} = -i \cdot \omega \tag{2.19e}$$

$$\frac{\partial}{\partial y} = 0 \tag{2.19f}$$

$$\frac{\partial}{\partial z} = i \cdot k_z \tag{2.19g}$$

The 3rd and 4th Maxwell's equations are represented using the curl operator. Therefore, Equations 2.19a and 2.19b are 3-dimensional vectors with x, y, and z components. The x and z components of Equation 2.19a and the y component of Equation 2.19b are used in this thesis, as shown
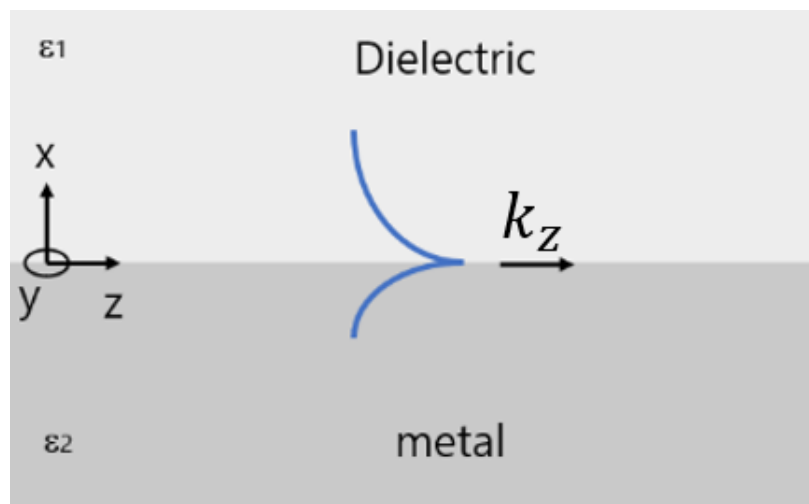
Figure 2.9: A surface electromagnetic wave propagating along the metal-dielectric interface.

in Equation 2.20, since the components are associated with TM mode.

$$\frac{\partial H_z}{\partial y} - \frac{\partial H_y}{\partial z} = -i \cdot \varepsilon \cdot \varepsilon_0 \cdot \omega \cdot E_x \tag{2.20a}$$

$$\frac{\partial E_x}{\partial z} - \frac{\partial E_z}{\partial x} = i \cdot \mu \cdot \mu_0 \cdot \omega \cdot H_y \tag{2.20b}$$

$$\frac{\partial H_y}{\partial x} - \frac{\partial H_x}{\partial y} = -i \cdot \varepsilon \cdot \varepsilon_0 \cdot \omega \cdot E_z \tag{2.20c}$$

Equations 2.20a and 2.20c can be simplified into Equations 2.21a and 2.21c using Equation 2.19f. Equation 2.20b can be simplified into Equation 2.21b using Equation 2.19g.

$$-i \cdot k_z \cdot \mathscr{H}_y = -i \cdot \varepsilon \cdot \varepsilon_0 \cdot \omega \cdot \mathscr{E}_x \tag{2.21a}$$

$$i \cdot k_z \cdot \mathscr{E}_x - \frac{\partial \mathscr{E}_z}{\partial x} = i \cdot \mu \cdot \mu_0 \cdot \omega \cdot \mathscr{H}_y \tag{2.21b}$$

$$\frac{\partial \mathscr{H}_y}{\partial x} = -i \cdot \varepsilon \cdot \varepsilon_0 \cdot \omega \cdot \mathscr{E}_z \tag{2.21c}$$

The Helmholtz equation in Equation 2.22a is obtained, substituting Equations 2.21a and 2.21c into Equation 2.21b for $\mathscr{E}_x$ and $\mathscr{E}_z$. Equation 2.22b is obtained, substituting Equation 2.21a into Equation 2.21b for $\mathscr{E}_x$. Finally, equation 2.22c is obtained, substituting Equation 2.21c into Equation 2.21b for $\mathscr{E}_z$.

$$\frac{\partial^2 \mathscr{H}_y}{\partial x^2} - \left(k_z^2 - \mu \cdot \varepsilon \cdot \frac{\omega^2}{c^2} \right) \cdot \mathscr{H}_y = 0 \tag{2.22a}$$

$$\mathscr{E}_z = \frac{i}{\varepsilon \cdot \varepsilon_0 \cdot \omega} \cdot \frac{\partial \mathscr{H}_y}{\partial x} \tag{2.22b}$$

$$\mathscr{E}_x = \frac{k_z}{\varepsilon \cdot \varepsilon_0 \cdot \omega} \cdot \mathscr{H}_y \tag{2.22c}$$

Equations 2.23b, 2.23c, 2.24b, and 2.24c can be obtained using Equations 2.22b and 2.22c. Equations 2.23b and 2.23c describe electric fields in the upper medium in Figure 2.9. Equations

2.24b and 2.24c describe electric fields in the lower medium in Figure 2.9. The solutions to Equation 2.22a are Equations 2.23a and 2.24a, representing the magnetic field in the upper and lower medium in Figure 2.9.

Equations 2.23 and 2.24 are the final equations. Boundary conditions, which are $\mathscr{H}_{1,y}(0) = \mathscr{H}_{2,y}(0)$ and $\mathscr{E}_{1,z}(0) = \mathscr{H}_{2,z}(0)$, are applied to Equations 2.23 and 2.24. After applying the boundary conditions to Equations 2.23 and 2.24, the dispersion equation for plasmonic materials, Equation 2.25, is obtained.

$$\mathscr{H}_{1,y}(x) = \mathscr{H}_1 \cdot e^{-\kappa_1 \cdot x} \tag{2.23a}$$

$$\mathscr{E}_{1,z}(x) = -\frac{i\kappa_1}{\varepsilon_1 \cdot \varepsilon_0 \cdot \omega} \cdot \mathscr{H}_1 \cdot e^{-\kappa_1 \cdot x} \tag{2.23b}$$

$$\mathscr{E}_{1,x}(x) = \frac{k_z}{\varepsilon_1 \cdot \varepsilon_0 \cdot \omega} \cdot \mathscr{H}_1 \cdot e^{-\kappa_1 \cdot x} \tag{2.23c}$$

$$\mathscr{H}_{2,y}(x) = \mathscr{H}_2 \cdot e^{-\kappa_2 \cdot x} \tag{2.24a}$$

$$\mathscr{E}_{2,z}(x) = -\frac{i\kappa_2}{\varepsilon_2 \cdot \varepsilon_0 \cdot \omega} \cdot \mathscr{H}_2 \cdot e^{-\kappa_2 \cdot x} \tag{2.24b}$$

$$\mathscr{E}_{2,x}(x) = \frac{k_z}{\varepsilon_2 \cdot \varepsilon_0 \cdot \omega} \cdot \mathscr{H}_2 \cdot e^{-\kappa_2 \cdot x} \tag{2.24c}$$

$$k_z = k_z' + i \cdot k_z'' = \frac{\omega}{c} \cdot \sqrt{\frac{\varepsilon_1 \cdot \varepsilon_2}{\varepsilon_1 + \varepsilon_2}} \tag{2.25}$$

Introducing Equations 2.26a and 2.26b to Equation 2.25, dispersion relations of SPPs can be obtained as shown in Figure 2.10. Equations 2.26a and 2.26b mean that dielectric's permittivity is a constant value, and metal can be described according to the Drude model's description. In Figure 2.10 (a), the solutions of Equation 2.25 for silver are found between 5 and 6 ($\times 10^{15}$) rad/s.

The solutions of Equation 2.25 for aluminum are found at around 1.35 and 2.35 ($\times 10^{16}$) rad/s. As shown in the simulations, the SPPs for aluminum are excited at a larger frequency than silver. If the angular frequency of light, ω, is larger than plasma frequency, Ω_p, then the light penetrates the metal. However, if $\omega \to \frac{\Omega_p}{\sqrt{2}}$ is satisfied, then $k_z \to \infty$ is accomplished.

$$\varepsilon_1 = \varepsilon_1^\infty \tag{2.26a}$$

$$\varepsilon_2 = \varepsilon_2^\infty - \frac{\Omega_p^\omega}{\omega^2} \tag{2.26b}$$

Choice of angular frequency (in other words, wavelength) is critical to excite SPPs, as shown in Figure 2.10, Equations 2.25 and 2.26 [14], [1]. After choosing a plasmonic material, optimizing geometry for a plasmonic system should be done. Dispersion relations and propagation lengths of SPPs for Au, Ag, Al, and Cu are plotted in Figure 2.11, referred to when choosing material for plasmonic systems [15], [1]. SPPs, surface plasmon polaritions, are excited at the arrow for materials in Figure 2.11. One of them can be chosen to decide SPPs energy and propagation length. Propagation length means how long SPPs can propagate on metals and can be obtained using equation 2.27 in which $k_z^{''}$ comes from equation 2.25.

$$L_{SPP} = \frac{1}{|2 \cdot k_z^{''}|} \tag{2.27}$$

Metal is well known for reflecting light, and k^t in Figure 2.12 can be described as a purely imaginary number. The penetration depth of light for metal can be obtained from the inverse of the pure imaginary number and is shown in Figure 2.13(a). The thickness of Al can be around 17-18 nm at 1550 nm wavelength, as shown in Figure 2.13(a). Equation 2.26 is substituted into Equation 2.25, and then the imaginary part of Equation 2.25 is for the propagation length for materials.

Figures 2.11(b) and 2.13(b) show the propagation lengths for materials.

The side and top views of the device for plasmonic coupling are shown in Figure 2.14. The air gap, metal thickness, spacers, and tapered waveguide were designed based on Otto configuration. Light is fully coupled to the nanoscale metal without reflection in a prism at a specific angle. The prism is placed on the two spacers. Therefore, the spacers' thickness determines the air gap's thickness.

(a)   (b)
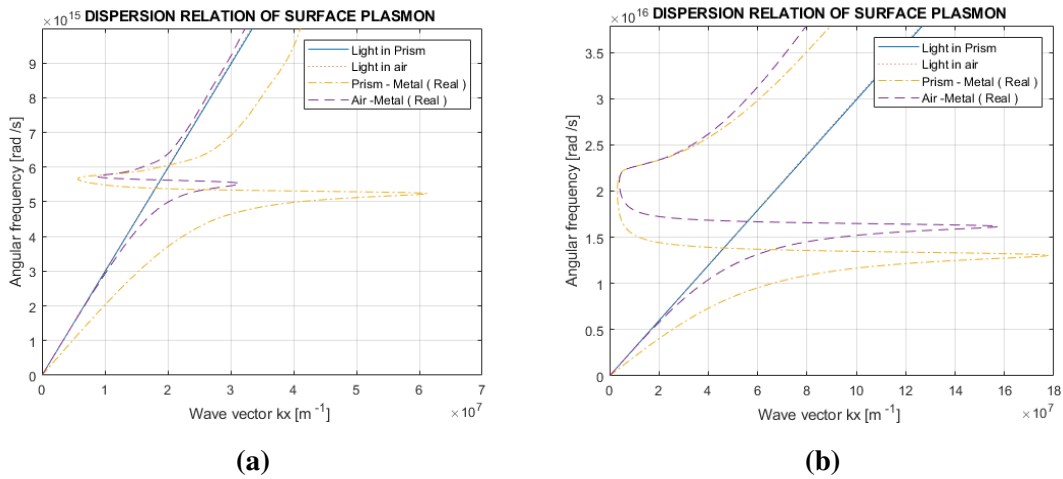
Figure 2.10: Dispersion curves of SPPs for (a) Ag and (b) Al.

(a)   (b)
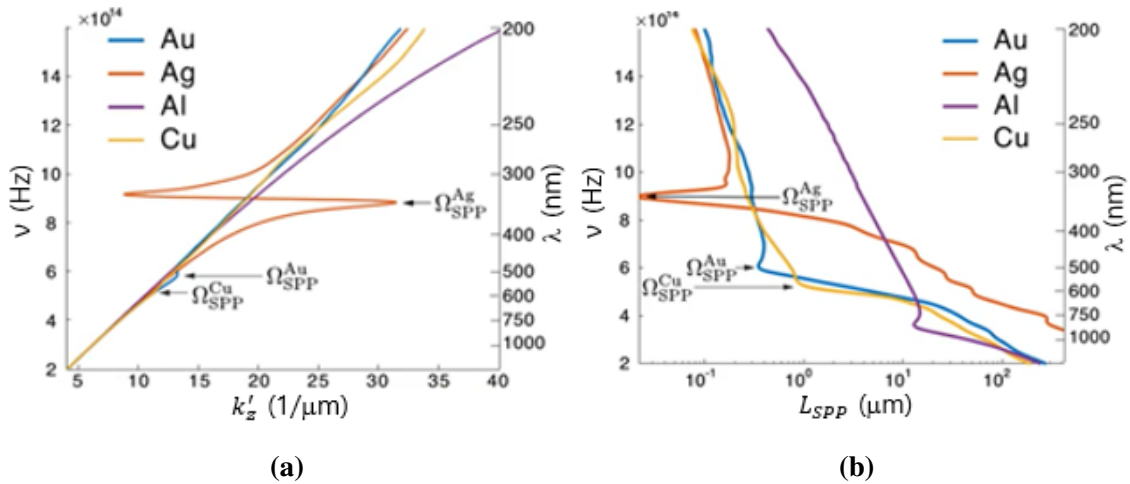
Figure 2.11: (a) Dispersion relations and (b) propagation lengths of SPPs for Au, Ag, Al, and Cu [1], [15].

Figures 2.15, 2.16, 2.17, and 2.18 show the plasmonic effects and how light propagates. In each figure, a prism is on the left. A metal layer and waveguide are on the top of the SiO_2. Light is introduced into the prism in Figure 2.15, coupled to the nanoscale metal, and goes through the 0.95 μ*m* thick air gap in Figure 2.16. The metal delivers the light to the waveguide in Figure 2.16

TM-polarization (p-polarization)

XZ plane is the plane of incidence
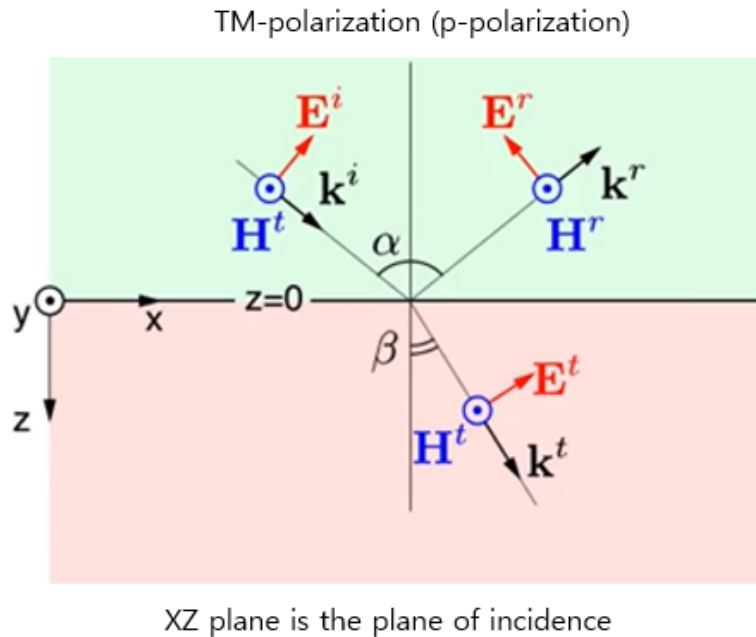
Figure 2.12: Incident, reflection, and refraction of TM-polarization between dielectric and metal [1].

(a)

(b)
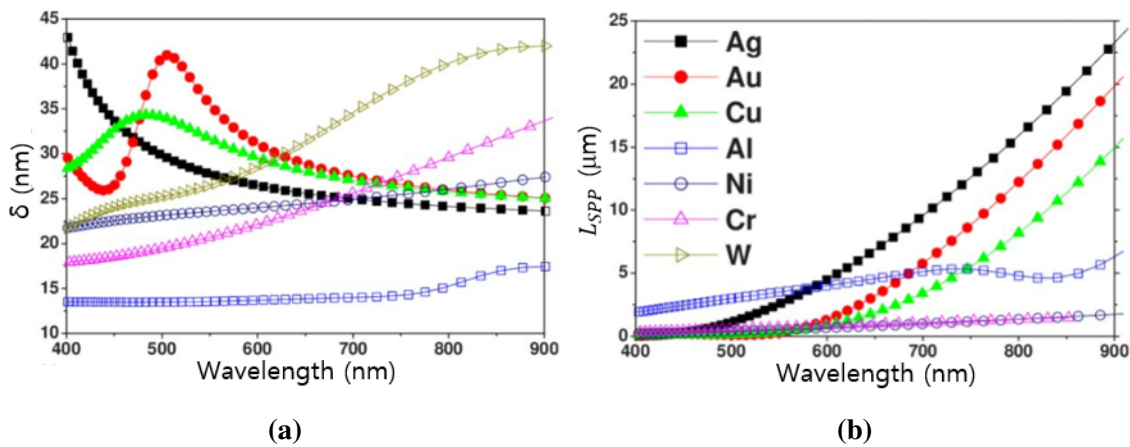
Figure 2.13: (a) Penetration depth. (b) Propagation length. [16]

as SPPs. When the SPPs reach the waveguide, the light is decoupled and propagates, as shown in Figure 2.17.

Three simulation results are shown in Figure 2.19. Nanoscale silver layer and Si waveguide were used for the simulations in Figures 2.19(a) and (b). SiN waveguide were used for the simulation in Figure 2.19(c) instead of Si waveguide. Figures 2.19(a) and (c) describe functions of incident angle for transmission, which are maximized at the angle of 43 °. The transmission is maximized at 1.3 μm thick air gap, as shown in Figure 2.19(b).
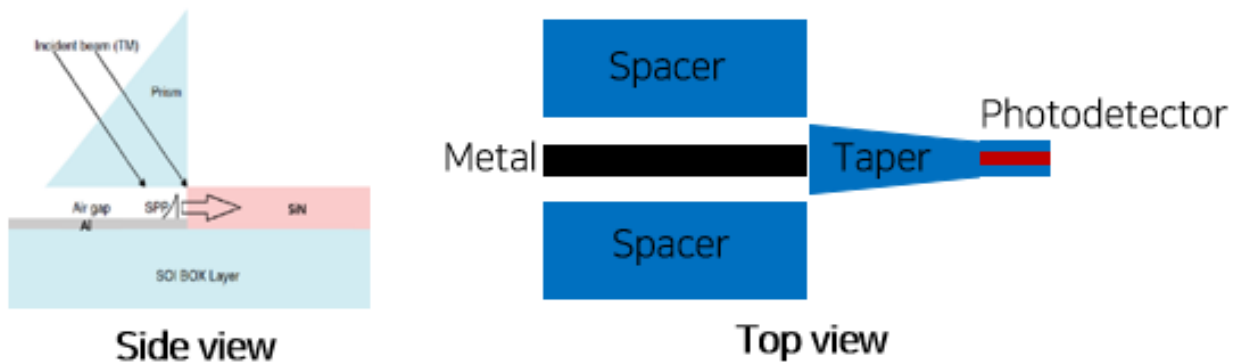
Figure 2.14: Side and top views in Otto configuration, which is used in this thesis.
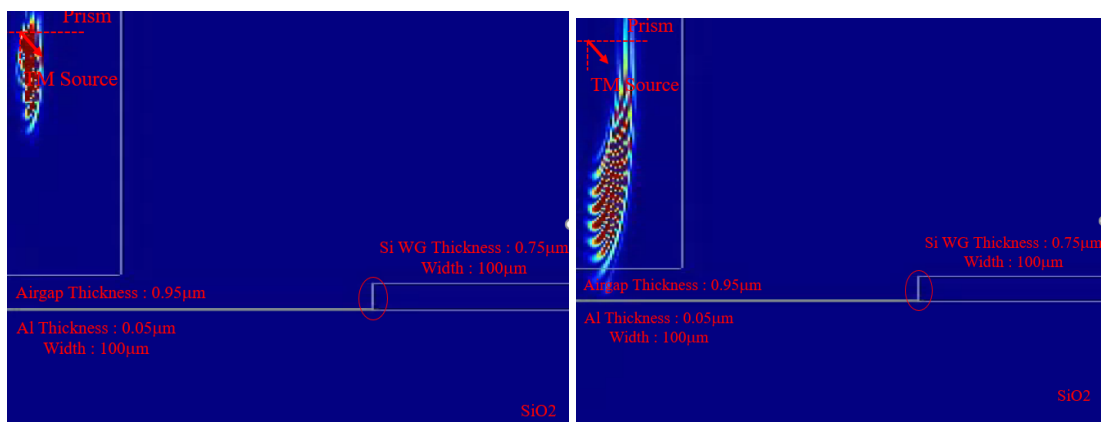
Figure 2.15: TM mode light is introduced to the prism and propagates toward the aluminum metal through the air gap. The aluminum metal layer is thinner than the silicon oxide layer. The thickness and width of the aluminum are 0.05 μm and 100 μm, respectively. The air gap's thickness is 0.95 μm.

The simulation result in Figure 2.19(c) shows lower transmission than other simulations since the SiN spacer can only have 300 nm thickness because the spacers and waveguides are fabricated using the same photomask. However, the transmission will increase if the air gap's thickness becomes larger. 250 nm thick air gap is not enough to fully couple light to the nanoscale metal.

As shown in the simulations and data, Ag offers higher performance than Al around 1550 nm wavelength in propagation length and transmission. First of all, most materials are not appropriate
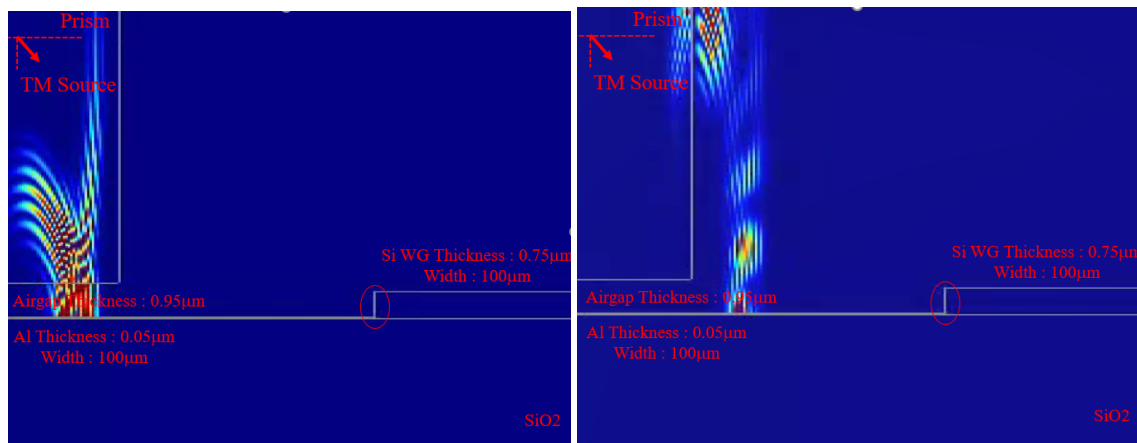
Figure 2.16: TM mode light goes through the 0.95 μ*m* air gap and reaches the aluminum metal. Some of the light is reflected from the aluminum and diverges into the air. The light coupled to the aluminum metal travels towards the silicon waveguide.
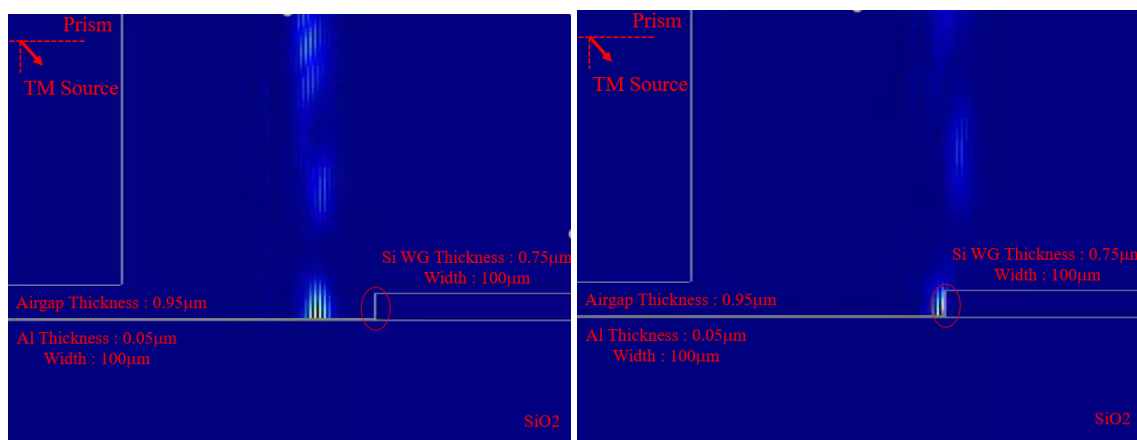
Figure 2.17: TM mode light coupled to the aluminum metal travels toward the silicon waveguide and reaches the silicon waveguide.

to use 1550 nm wavelength for SPPs, as shown in Figure 2.11. New material should be found to raise the efficiency of SPPs in telecommunication wavelength.

The light is coupled to nanoscale metal with high efficiency [1]. However, Figure 2.19 shows that 60% and 15% of light are transmitted to Si and SiN waveguides, respectively, which assume that coupled light is attenuated in the y-direction. Most coupled light disappears at the boundary between the metal and waveguide, as shown in Figures 2.17 and 2.18.
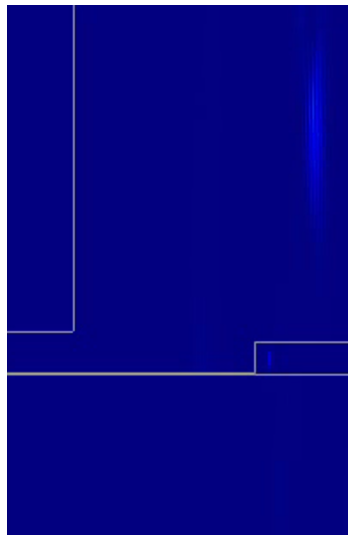
Figure 2.18: TM mode light is decoupled from the aluminum metal and coupled to the silicon waveguide. The faint light propagates in the silicon waveguide.

| (a) | (b) | (c) |
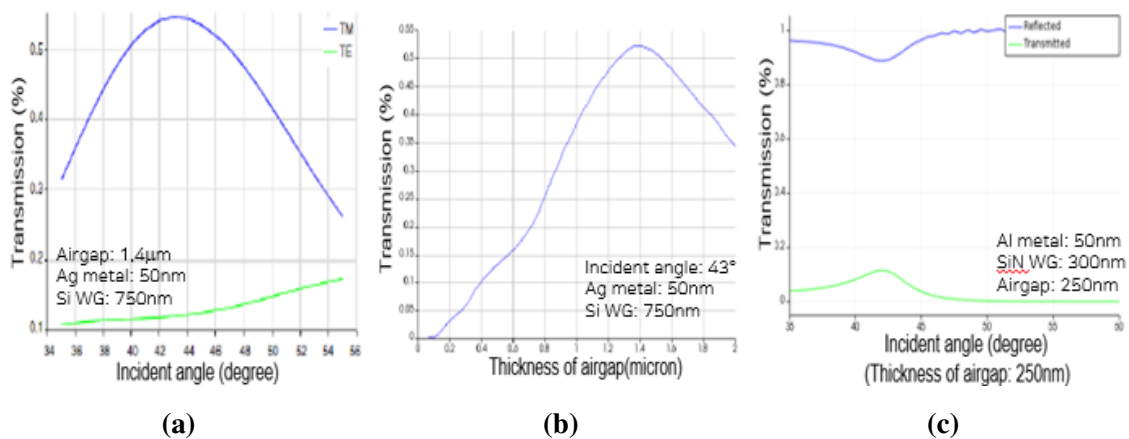
Figure 2.19: (a), (c) Transmission as a function of incident angle. (b) Transmission as a function of air gap [14].

2.3. Prism Coupler

A prism coupler is one of the most valuable tools to couple light to metal. Prism has a high refractive index and is located close to the metal. Evanescent light is excited when light hits the prism's bottom at an angle greater than the critical angle. The evanescent light is coupled to metal that carries the light to a waveguide. This coupling method can be used for plasmonic coupling. A high refractive index is required in normal prism coupling. However, plasmonic coupling using nanoscale metal does not need a high refractive index prism, which broadens the choice of a prism. Figure 2.20 shows Otto and Kretschmann configurations that enable prism coupling [17].
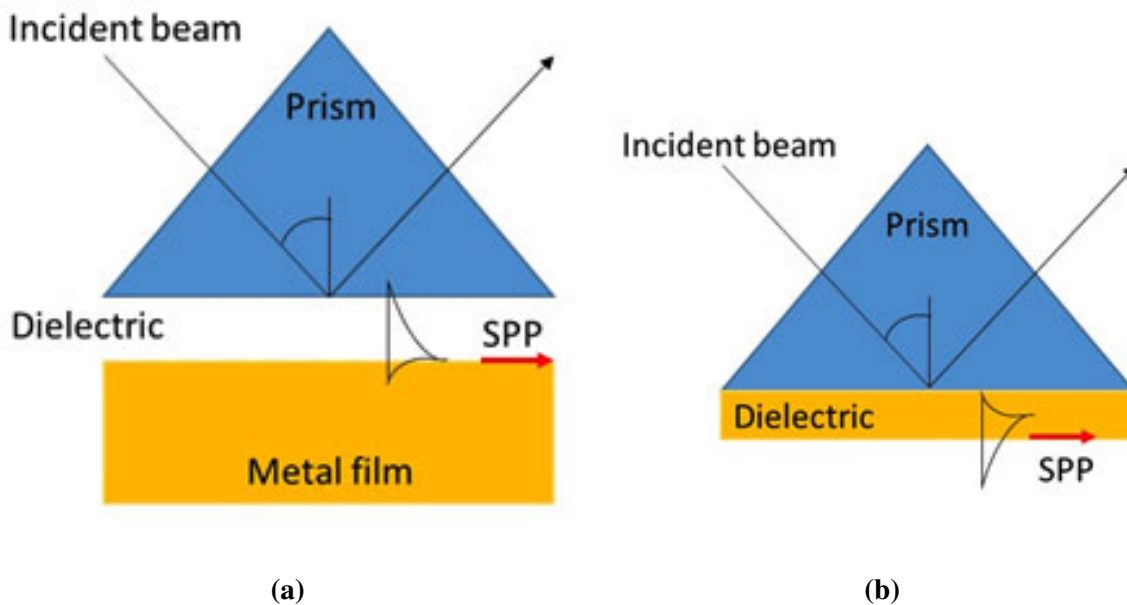
Figure 2.20: (a) Otto (b) Kretschmann configurations. [17]

3. FABRICATION

This thesis deals with the whole process of input, circuit, and output. The whole process consists of three steps, as shown in Figure 3.1. As a detailed explanation, incident light is coupled to metal using a prism and is carried by metal toward the second chip. The light coupled to metal is decoupled to the second chip, Integrated Photonic Education Kit (IPEK). IPEK consists of many photonic devices such as directional coupler, Bragg cavity, waveguides, and ring resonators. The light from IPEK propagates to photodetectors and is detected by the photodetector.

In this chapter, the fabrication of photodetectors and metals for prism coupling using SPPs is covered. The integrated devices with metal and PIN photodetectors were fabricated in the cleanroom at Rose-Hulman Institute of Technology using four photomasks which were drawn using KLayout program. The tools used to fabricate the integrated devices were furnaces for oxidation and doping, photolithography equipment, sputtering machine, PECVD, and RTA. The metal fabricated can be cut out to test photodetectors using butt coupling. (100) orientation wafer should be used to cleave wafer in X or Y direction as shown in Figure 4.14, which will be explained in the
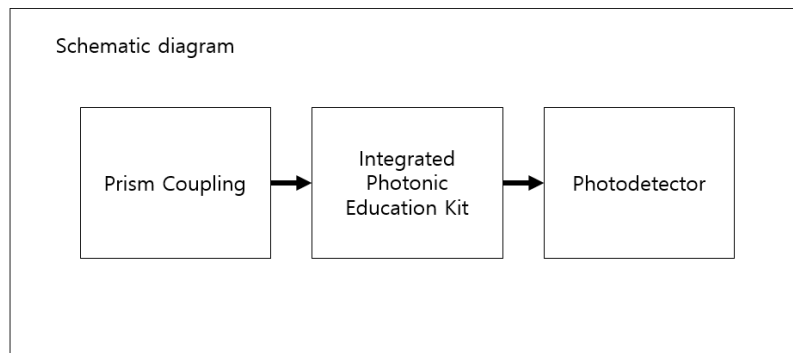
Figure 3.1: The whole process consists of three parts. Incident light is coupled to metal using the plasmonic effects, and the light is decoupled to the Integrated Photonic Education Kit. The light is detected using the photodetector made by us.

next chapter.

Figure 3.2 shows each step in sequence for the fabrication of the integrated devices. Step 1 is to clean silicon wafers using RCA cleaning. After RCA cleaning, silicon oxide of 800 µm is grown on the silicon wafers, and it takes 5 hours to grow 800 nm thick silicon dioxide. Silicon nitride of 300 nm is deposited on the silicon oxide layer with PECVD in step 2, and the silicon nitride is p-type doped in a doping furnace for 10 minutes with a boron target. The silicon nitride is spin-coated with the SPR3600 photoresist, which is patterned in step 3. The silicon nitride is etched out with PECVD using CF4 gas in step 4. After the etching of the silicon nitride, the rest of the photoresist is removed in step 5. Germanium of 200 nm is deposited with a sputtering machine in step 6. Germanium is patterned using the lift-off method, and the rest of the germanium is removed in step 7. The aluminum is deposited and patterned using the lift-off method in step 8. The rest of the photoresist is removed in step 9.

Four photomasks were designed and order-made before fabricating. Several wafers should be cleaned off using RCA cleaning. The following chapter explains the 4 photomasks followed by RCA cleaning.

3.1. Mask Design

The four masks were designed using KLayout program and order-made before fabricating the photodetectors and metals on wafers. Figures 3.3, 3.4, 3.5, and 3.6 show each mask layout for making patterns of silicon nitride, germanium, aluminum, and doping process.

The silicon nitride mask is a bright field mask, so photoresist in the bright field is exposed to light and removed. The germanium, aluminum, and doping masks are all dark field masks.

3.2. Fabrication Process

3.2.1. RCA Cleaning

RCA cleaning should be performed to remove dust and particles on wafers. Instruction on RCA cleaning is set in the cleanroom. RCA cleaning consists of two steps, which are SC-1 and SC-2. SC-1 is alkali and NH_4OH:H_2O_2:H_2O with 1:1:5 at 70-80°C to remove organic contaminants and particles. Some metals such as Al and Fe are insoluble in the solution and tend to precipitate on the surface of Si wafers. SC-2 is HCl:H_2O_2:H_2O with 1:1:6 to 1:2:8 ratio at 70 to 80 °C to remove
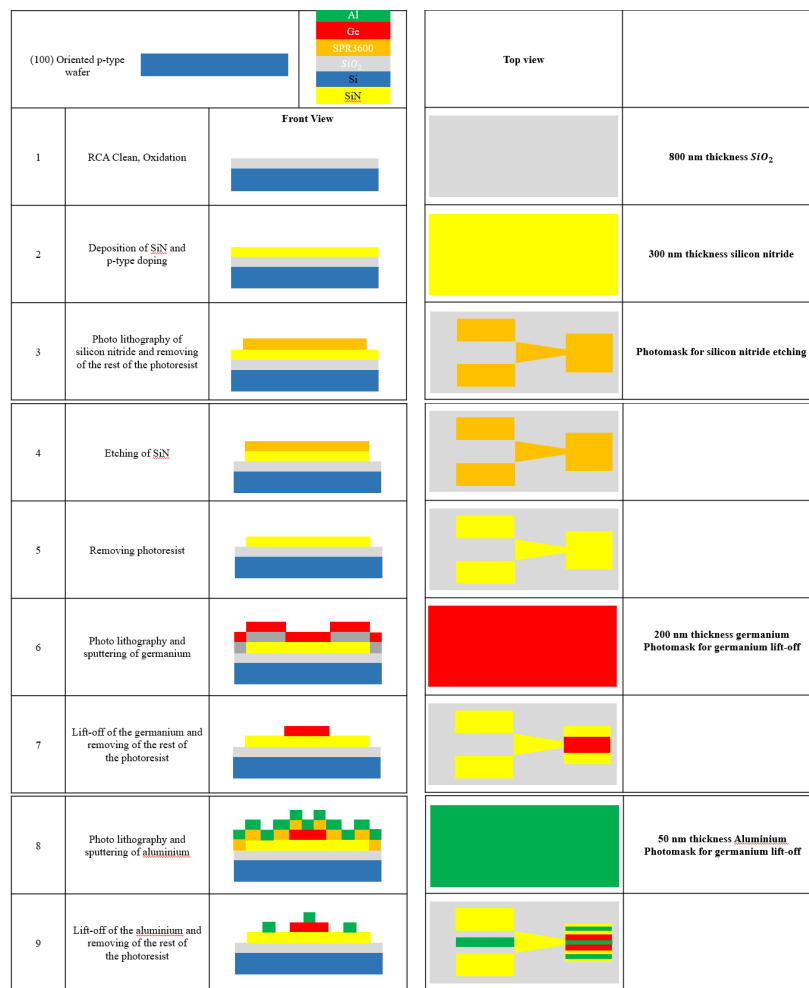
Figure 3.2: Fabrication process.

inorganic contaminates. HCl removes alkali and transition metals such as Fe. After each step, the wafer should be rinsed with DI water. After performing SC-1 and SC-2, the wafer should be dipped in HF to remove native oxide. However, there is some caution before performing the HF dip. After SC-1 or SC-2 steps, the surface of wafers becomes hydrophilic, and particles do not tend to stick to wafers. However, after the HF dip, wafers become hydrophobic. Hence, particles

Mask 1 – Silicon nitride (Bright field mask)
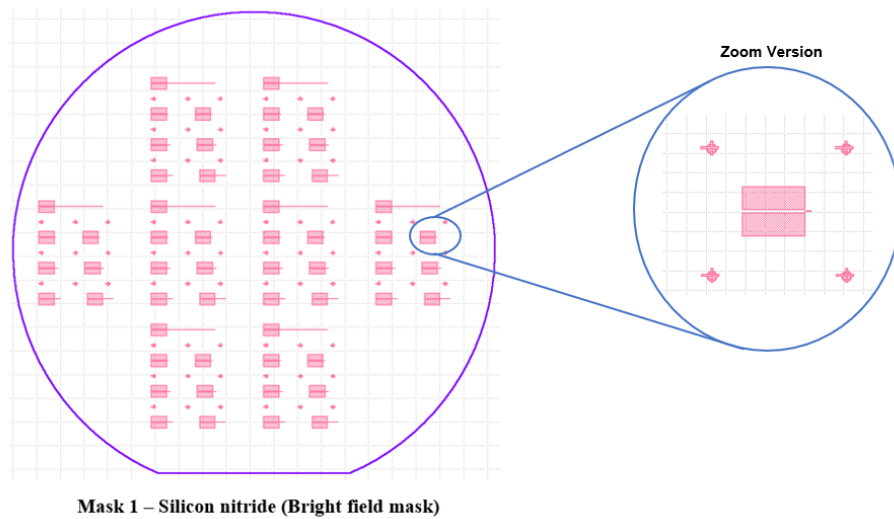
Figure 3.3: Silicon Nitride Mask layout in GDS file.

Mask 2 – Germanium (Dark field mask)
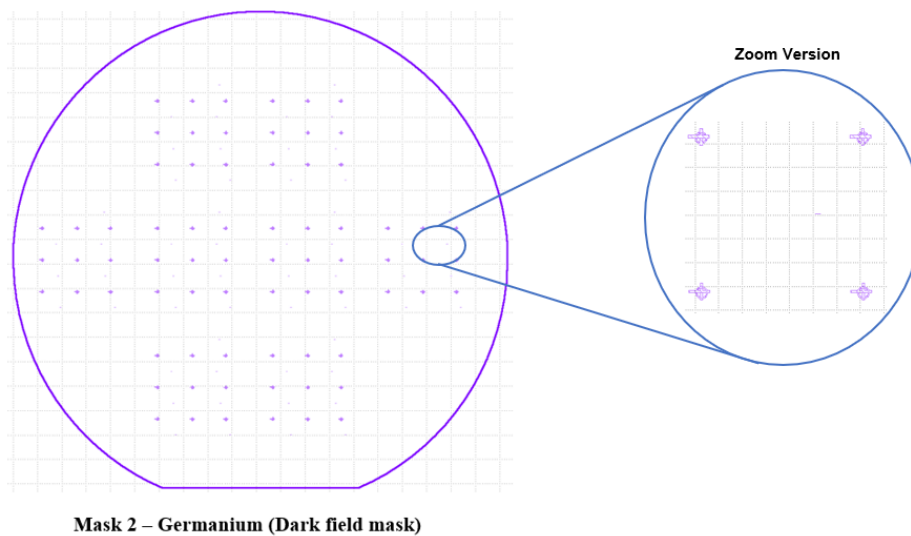
Figure 3.4: Germanium Mask layout in GDS file.

tend to stick to wafers. Therefore, it is recommended to perform the HF dip right before doing the next step, which is oxidation.

3.2.2. Oxide Growth

After RCA cleaning, 800 nm thickness of silicon oxide was grown on the wafers cleaned. There are two furnaces used for wet or dry oxidation, respectively. The wet oxidation furnace shown in
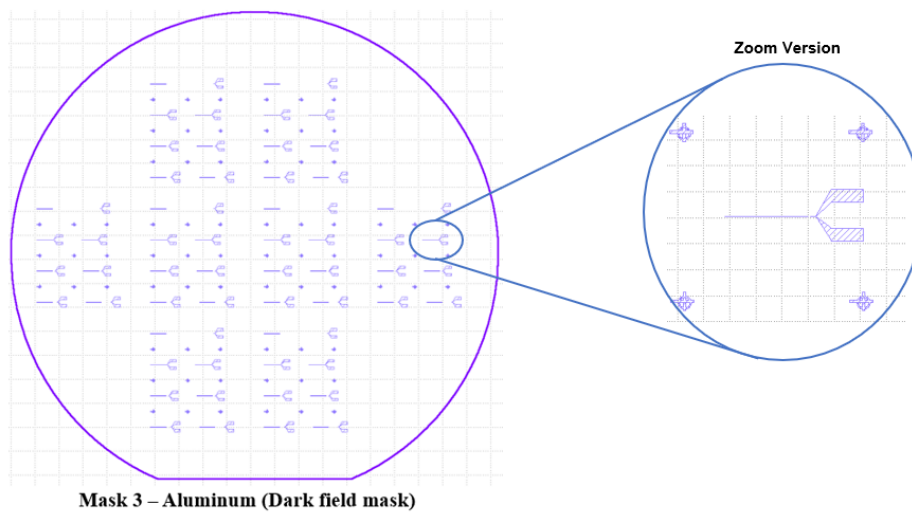
Figure 3.5: Aluminum Mask layout in GDS file.
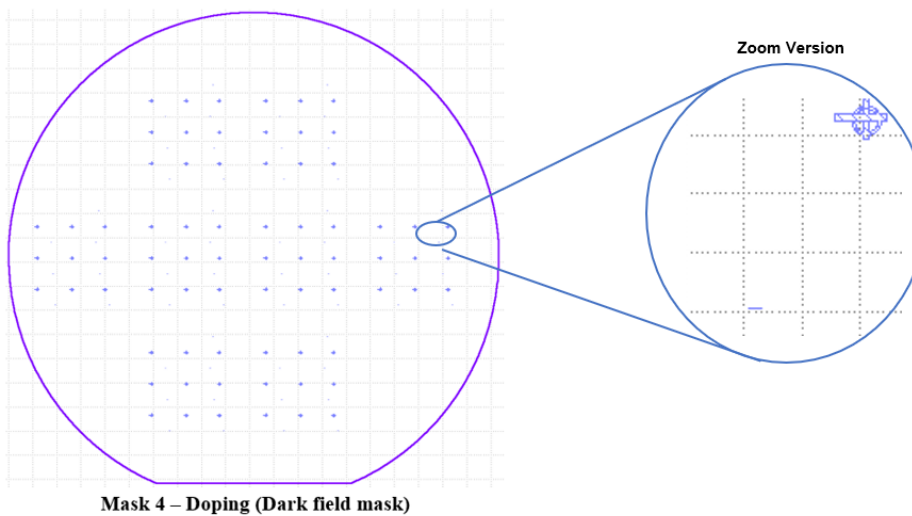
Figure 3.6: Doping Mask layout in GDS file.

Figure 3.8 was used in this step. P-type silicon wafers were put in the furnace to oxidize. Figure 3.7 shows the silicon oxide's thickness grown on the silicon wafers. Each thickness of silicon dioxide is 846 and 832.4 nm, respectively, as shown in Figure 3.7. The two silicon oxide's quality is good, as shown in Figure 3.7.

To perform oxidation, gas bottles of oxygen and nitrogen in the cleanroom should be turned on. A water flask is found behind the oxidation furnace, as shown in Figure 3.8(a). The water flask should be checked if there is enough water. The temperature of the oxidation furnace should be set to 800 °C and slowly raised to 1000 °C, as shown in Figure 3.8(b). When the temperature is stable at around 1000 °, wafers should slowly be pushed into the oxidation furnace (1 inch/min). If this caution is ignored, wafers will have dislocation defects, and the wafers will be bent. Wafers should stay in the furnace for 7-8 hours to grow 800 nm thick silicon oxide. The oxidation rate depends on the orientation of silicon wafers. (111) orientation silicon wafers have a high oxidation rate than (100) orientation silicon wafers since silicon atoms are densely combined. If a p-type or n-type silicon wafer is used, then the oxidation rate increases. Dry oxidation gets silicon wafers better quality of silicon oxide than wet oxidation. However, dry oxidation is slower than wet oxidation.

(a)   (b)
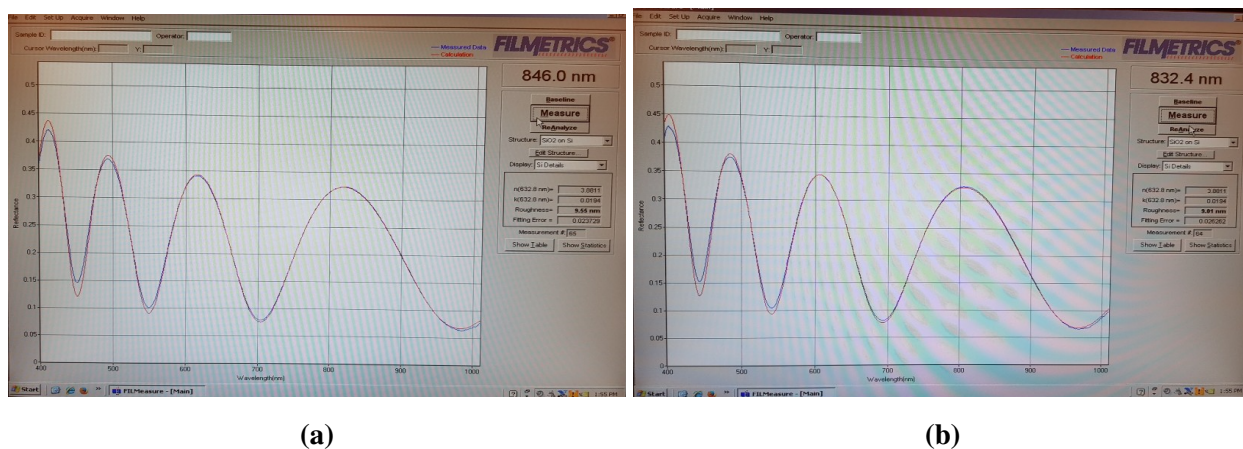
Figure 3.7: Measurement after oxidation. The thickness of silicon oxide grown on two silicon wafers are (a) 846 and (b) 832.4 nm, respectively.

The silicon dioxide's quality is not significant in this paper since it is used as an insulator. But, if silicon oxide is used as a depletion layer in a transistor, then the silicon oxide's quality becomes essential.

3.2.3.   Silicon Nitride Growth

Silicon nitride was deposited after oxidation. The PECVD in Figure 3.14 was used to perform the deposition of silicon nitride. The recipe was newly designed since the quality of silicon nitride film deposited by the old silicon nitride recipe was not good.

PECVD refers to Plasma-enhanced chemical vapor deposition, which is a chemical vapor deposition process. PECVD has been used to deposit thin films. Chemical reactions occur in the chamber after vapor in a gas state changes into a solid state on a substrate creating a plasma.

Before running the PECVD, the PECVD's power and vacuum pump should be turned on. A recipe for deposition of silicon nitride should be chosen. Argon, ammonia, and silane were used to deposit silicon nitride, and their bottles were turned on. Before opening the chamber's lip, the vacuum valve behind the chamber got closed, as shown in Figure 3.14(b). A wafer was placed on the substrate in the chamber. After closing the chamber's lip, the vacuum valve was turned

| (a) | (b) | (c) |
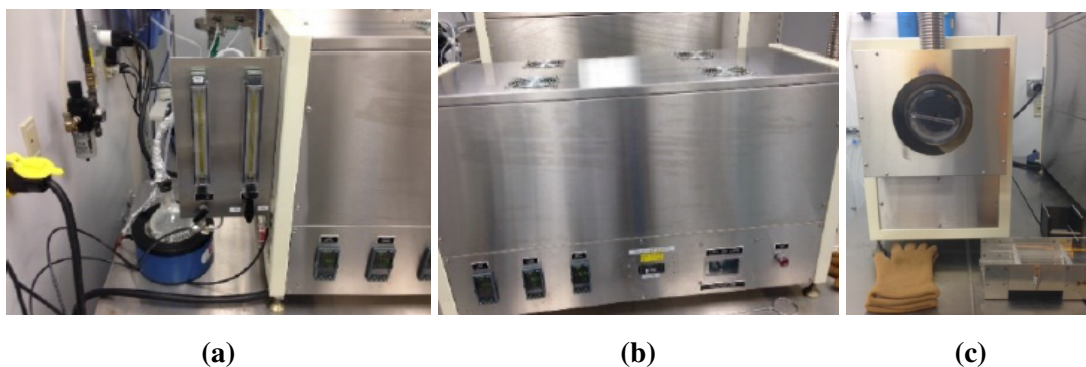
Figure 3.8: Furnace for growth of silicon oxide. (a) Gas flow controllers and a water flask. (b) Temperature controller. (c) Entrance of the furnace.

on to make vacuum pressure in the chamber. The PECVD started to run after clicking on the run button on the computer. The PECVD ran according to the recipe. The temperature in the chamber increased slowly up to 300 °C. After finishing running the recipe, the chamber cooled down to around 120 °C. When the temperature became about 120 °C, the vacuum valve closed, and the wafer could be retrieved.

As shown in Figure 3.9, there are two silicon nitride wafers deposited. The wafer in Figure 3.9(a) shows a commercial silicon nitride wafer made with LPCVD. The wafer in Figure 3.9(b) shows a silicon nitride wafer of bad uniformity, which the old recipe was used. The second wafer shows why a new recipe should be made for the deposition of silicon nitride.

The old recipe not only gets the wafers bad uniformity but also gets them shower head pattern. The gas deflector shown in Figure 3.10(a) was not used to generate the patterns on the wafers. However, the gas deflector made the uniformity of silicon nitride worse. The wafer in Figure 3.9(b) is the silicon nitride wafer made using the gas deflector. Wafers get the shower patterns on silicon nitride without using the gas deflector, as mentioned and shown in Figure 3.10(b).

(a)   (b)
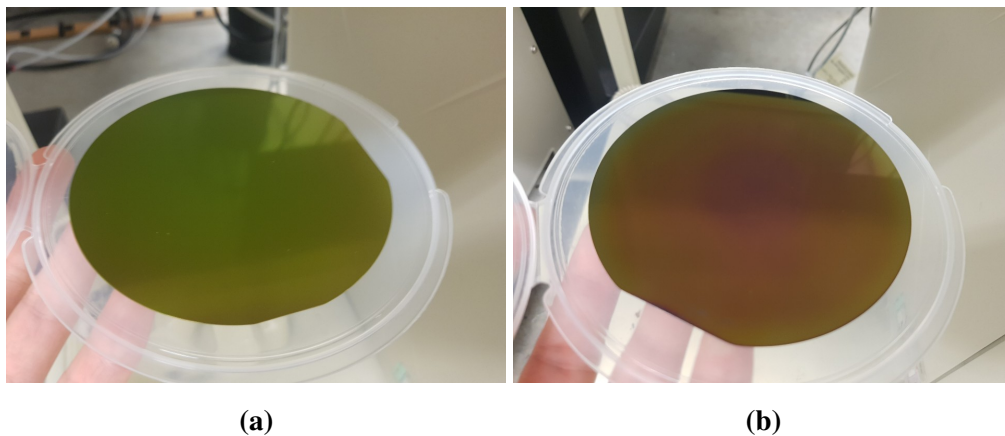
Figure 3.9: Two wafers of silicon nitride are shown in this figure. (a) The commercial wafer is deposited with LPCVD and has good film quality. (b) The wafer is deposited with PECVD using the old recipe.

The wafers' thicknesses in Figure 3.9 were measured using the tool in Figure 3.15. Figures 3.11(a) and 3.11(b) show 292.2 nm and 262.7 nm thicknesses of silicon nitride, which are made using LPCVD and PECVD, respectively.

For the reasons mentioned above, a new silicon nitride recipe was made. The gas ratio is the most critical part of designing a silicon nitride recipe. The gas ratio of silane to ammonia used in the PECVD in Figure 3.14 should be 1:2. The deposition time and average thickness are 10 minutes and 50 nm, respectively.

The silicon nitride wafer in Figure 3.12(a) is made using the new silicon nitride recipe and has 57.14 nm thickness as shown in Figure 3.12(b). The wafer in Figure 3.12(a) has good uniformity and no head shower patterns.

It is significant to make the same condition in the PECVD each time before running the silicon nitride recipe. The film quality strongly depends on the condition in the PECVD's chamber.

(a)   (b)
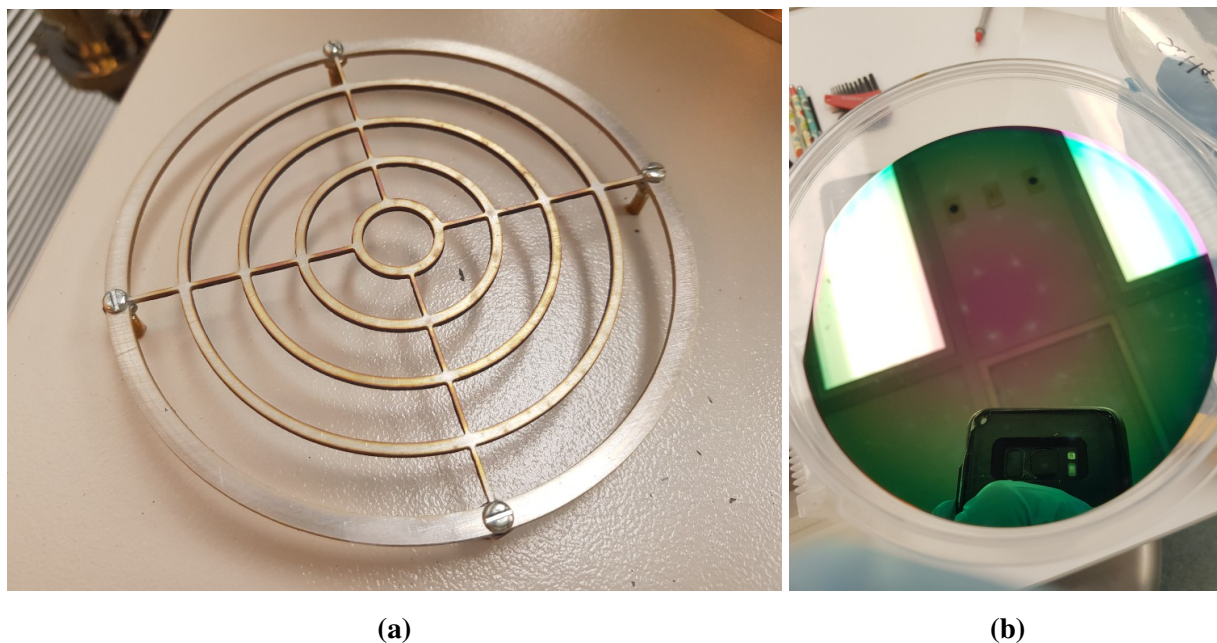
Figure 3.10: (a) The gas deflector is used to prevent a wafer from getting the shower head pattern of PECVD. (b) The wafer has the shower head pattern from PECVD.

To make the same condition in the chamber, first, the chamber should be cleaned using the CF4 gas. Second, the PECVD's chamber should be purged with Argon for 5 minutes. Third, a dummy wafer should be placed in the chamber, and the seasoning recipe should be run, which is required to remove the first wafer effect. After completing the previous processes, it is time to run "Nitride 20 40 20W 10minutes" recipe. The seasoning recipe is found in the same folder named "Nitride 20 40 20W 10minutes" recipe.

The kick plasma step can be found in the silicon nitride recipe. As referred to the PECVD's manual, the kick plasma should be between 30W and 50W since 20W plasma for silicon nitride deposition is too low to start with, so the kick plasma helps to generate the plasma in the chamber.

Silicon nitride, which is made using PECVD, has many hydrogen, voids, and dangling bonds. Annealing process with RTP should be employed to remove hydrogen, voids, and dangling bonds. Nitrogen gas is required with a temperature of more than 700°C in the annealing process.

The RTP in Figure 3.16 was used for the annealing of silicon nitride. Defects such as dangling bonds and voids were made during the rapid deposition of silicon nitride. Silicon nitride can be annealed using either the oxidation furnace or the RTP. The RTP is easier to use than the furnace

(a)   (b)
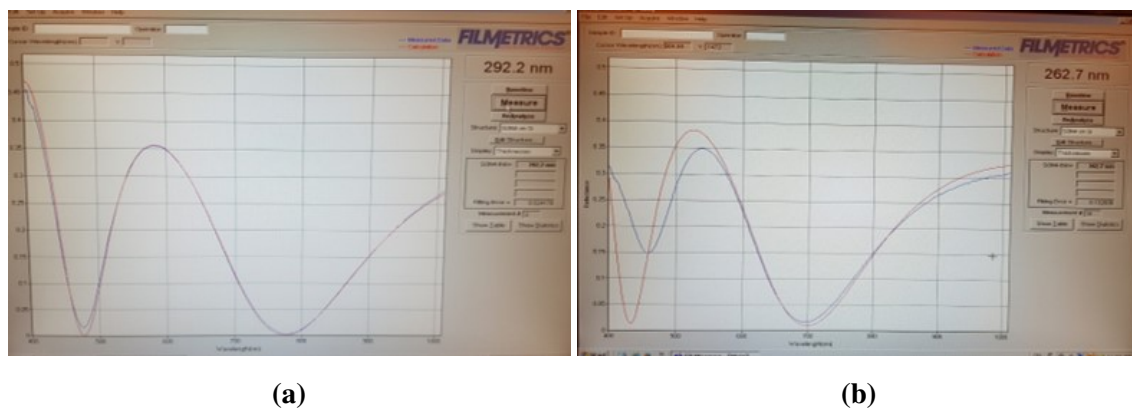
Figure 3.11: Measurement of the silicon nitride wafers in Figure 3.9 using the tool in Figure 3.15. (a) The measurement of the wafer in Figure 3.9(a) is 292.2 nm. (b) The measurement of the wafer in Figure(b) is 262.7 nm.

since it does not take as much time as the furnace needs, and the processes are automatically completed after clicking the run button on the RTP. There is a recipe newly made for annealing silicon nitride on the RTP. After the annealing process, measurement was done, as shown in Figure 3.13(a). The ellipsometry was used in this measurement, as shown in Figure 3.13(b). The thickness of the silicon nitride and the silicon oxide deposited on the silicon wafer are 293.31 nm and 871.6 nm, respectively, as shown in Figure 3.13(b).

The silicon nitride recipe was newly designed as mentioned. The PECVD in Figure 3.14 was used to deposit silicon nitride, and the quality of silicon nitride strongly depends on the condition of the chamber of the PECVD. The particles of other materials were still stuck to the chamber's wall even though the CF4 cleaning process was done. The particles influenced the quality of the silicon nitride.

As another issue, silicon oxide was formed in the silicon nitride layer, as shown in Figure 3.30. The ellipsometer in Figure 3.30(b) measured the silicon nitride layer as shown in Figure 3.30(a). As reported in the paper [18], silicon oxide is formed in the silicon nitride layer. The PECVD

(a)   (b)
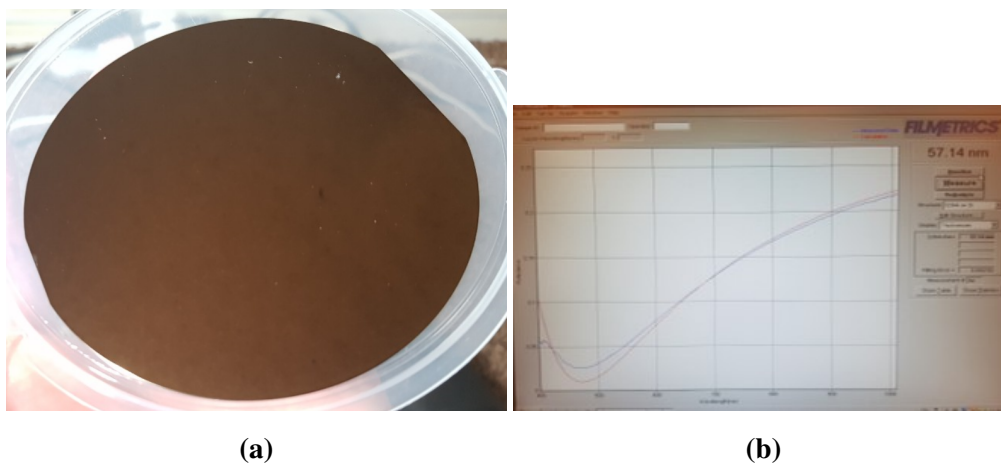
Figure 3.12: (a) Silicon nitride wafer shows no shower head pattern and has good uniformity, which is made using the new silicon nitride recipe. (b) The thickness of the silicon nitride wafer is 57.14 nm.
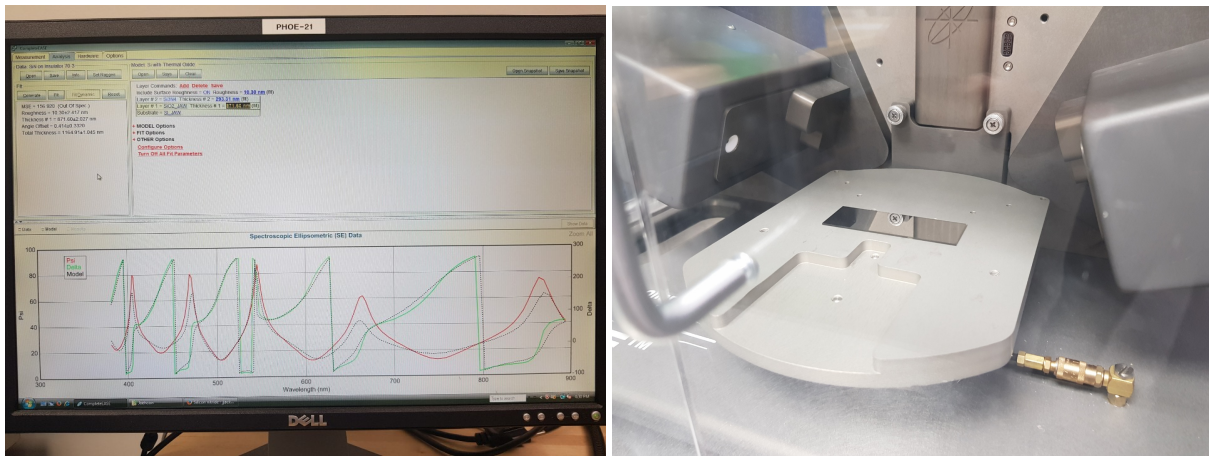
(a)   (b)

Figure 3.13: Measurement of the wafer in Figure 3.12(a) with the ellipsometry. (a) 871.6 nm thick silicon oxide was deposited for 6 hours in the oxidation furnace. 293.31 nm thick silicon nitride was deposited for 50 minutes in the PECVD using the new silicon nitride recipe. (b) This figure shows how we measure the chip using the ellipsometer.

(a)   (b)

Figure 3.14: (a) PECVD used for deposition and etching of silicon nitride in this paper. Chamber, Power, and vacuum pump are shown. (b) The valve between the chamber and vacuum pump is shown behind the chamber.

always has oxygen particles in the chamber, and the oxygen particles generate silicon oxide during deposition of the silicon nitride layer [18]. Silicon nitride does typically not interact with HF solution [19], but the silicon nitride, which has oxygen atoms in the layer, gets etched by HF solution.

It is desirable to use LPCVD to avoid generating silicon oxide in silicon nitride. Furthermore, LPCVD shows better performance on the deposition of several films since the process is done under lower pressure and higher temperature than PECVD.

(a)
(b)
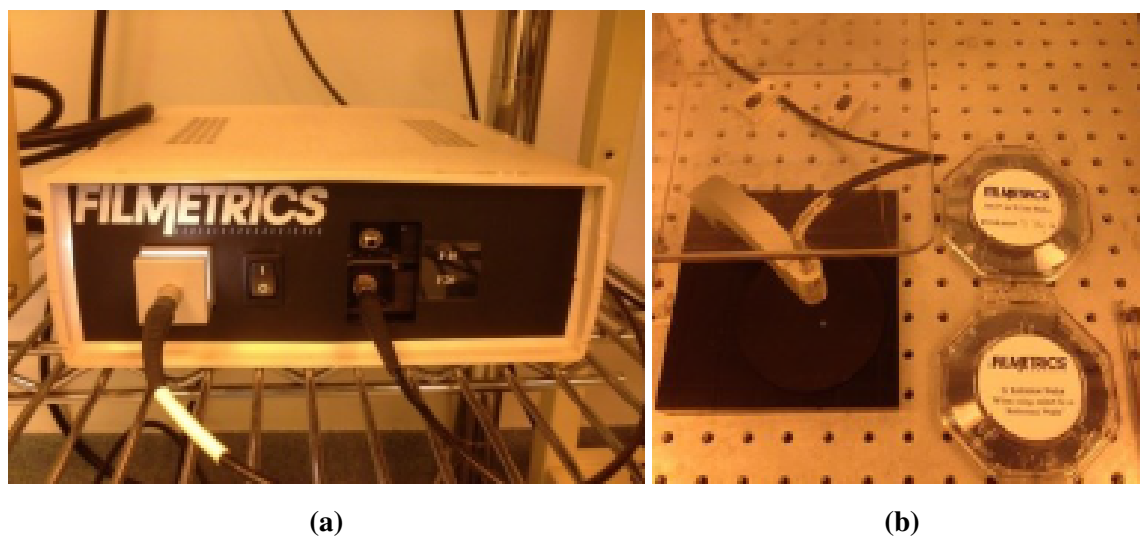
Figure 3.15: Tool for thin-film measurement. (a) Broadband light source. (b) There are two reference wafers and a wafer stage. Calibration using the two reference wafers is required according to the manual in the cleanroom.

(a)
(b)
(c)
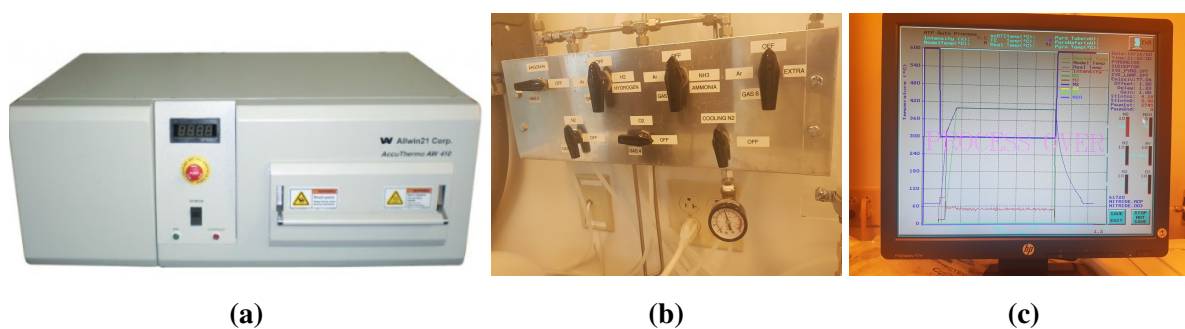
Figure 3.16: Equipment for annealing of silicon nitride. (a) RTP body. (b) Valves for gas flow. (c) Monitor connected to the RTP body.

3.2.4. Doping

A doping process is required to form PIN configuration in photodetectors. After finishing a lift-off of germanium, p-type doping of germanium should have been done. However, it was unable to p-type dope germanium since the cleanroom does not own p-type spin-on-dopants.

Germanium cannot be doped with the doping furnace due to the vaporization of germanium at 400-500 °C forming germanium oxide readily [20]. The germanium's central area in Figure 3.28(c) was vaporized due to the interaction with oxygen. The measurement was done using the profilometer in Figure 3.29(a). The image in Figure 3.29(b) indicates that the thickness of the central area is 300 nm which means the silicon nitride is uncovered. The not vaporized area was deposited with silicon oxide as a hard mask not to be p-type doped. Spin-on-dopants should be used to p-type dope germanium to resolve the issue shown in Figure 3.28(c). For another method, the RTP in Figure 3.16 can be used to p-type dope germanium using aluminum gas.

The photomask in Figure 3.5 was made based on a lateral photodetector, which should use spin-on-dopants. The photomask in Figure 3.5 is unable to operate with the doping furnace. Therefore, the plan was changed into p-type doping of silicon nitride due to the issues mentioned above.

Methods for doping of silicon nitride are reported in the papers [11], [12], which uses CVD using aluminum powder and PECVD using boron, respectively, in high temperature. They performed the doping right after deposition of silicon nitride in the same furnace or chamber, maintaining high temperature.

Figure 3.12(a) shows that the silicon nitride layer was doped in the doping furnace using a boron-source target. The doping process of silicon nitride was performed before the etching of silicon nitride. The boron-source target was put in the doping furnace, and the doping furnace's temperature increased up to 900 °C with nitrogen gas. When the temperature reached 900 °C, the

wafer in Figure 3.12(a) was slowly put in the doping furnace. The boron was diffused into the silicon nitride layer for 10 minutes. The final doping configuration is shown in Figure 3.25.

3.2.5. Etching of silicon nitride

After p-type doping of silicon nitride, the silicon nitride was patterned to form waveguide, taper, and the base layer of photodetectors. Spin-coating with the SPR3600 photoresist, soft-bake for a minute, photolithography with the photomask in Figure 3.3, exposure-bake for one minute, and hard-bake for 3 minutes were done. The photoresist was patterned, as shown in Figure 3.17.

After patterning of the photoresist, the silicon nitride was etched. The PECVD in Figure 3.14 was used to etch silicon nitride. CF4 plasma etching recipe on the PECVD was used. The CF4 plasma etching is not an isotropic process, making vertical walls with slight scattering loss. Phosphoric acid at 170-180 °C can be used for wet etching, anisotropic process. However, wet etching is inappropriate for waveguides to have vertical walls. After the etching of silicon nitride, the rest of the photoresist was removed. The silicon nitride was formed as spacers, tapers, photodetector's base layer, and alignment marks, as shown in Figure 3.18. The silicon oxide layer was uncovered

(a)   (b)
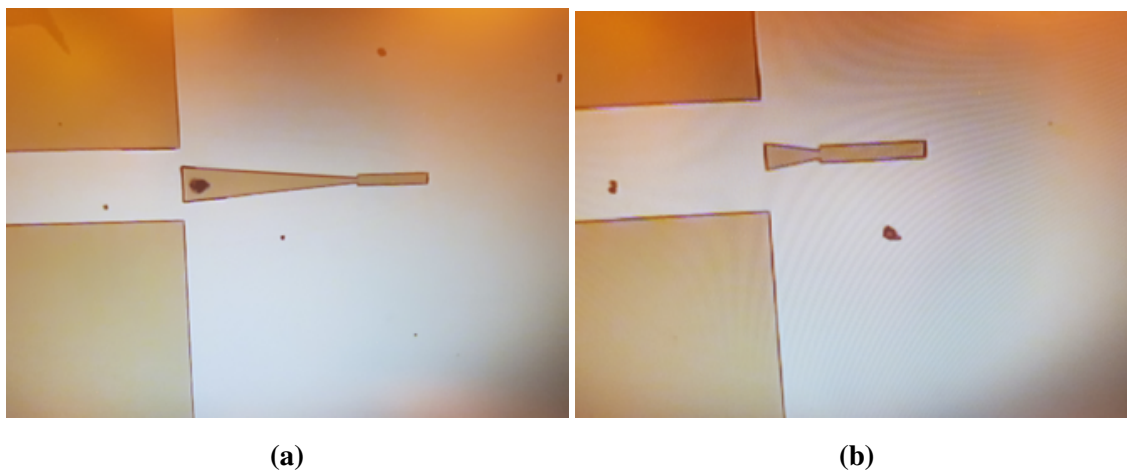
Figure 3.17: Photoresist was patterned. The silicon nitride layer is shown in the area that the photoresist is removed. (a), (b): Spacers, tapers, and base layer of photodetectors are shown.

in the area removed during the dry etching process, as shown in Figure 3.18.

3.2.6. Germanium Deposition

Germanium was deposited after the etching process. Germanium absorbs photons coming from silicon nitride waveguide. The sputtering machine in Figure 3.23(a) was used to deposit germanium.

Sputtering deposition is a physical vapor deposition method of thin film deposition by sputtering. The method includes ejecting material from a target, which is a source, onto a substrate. A few particles are ionized among the ejected materials and deposited onto the wafer in straight lines.

The bottles of argon, nitrogen, and vacuum pump's power should be turned on to use the sputtering machine. A wafer is put in the small chamber in Figure 3.23(a). The main and small chambers' pressures in Figure 3.23(a) become equal by lowering the main chamber's pressure up to the small chamber's pressure. After dropping the pressure, the valve between the main and small chambers is opened. The wafer placed in the small chamber is pushed into the main chamber. The valve is

(a)   (b)
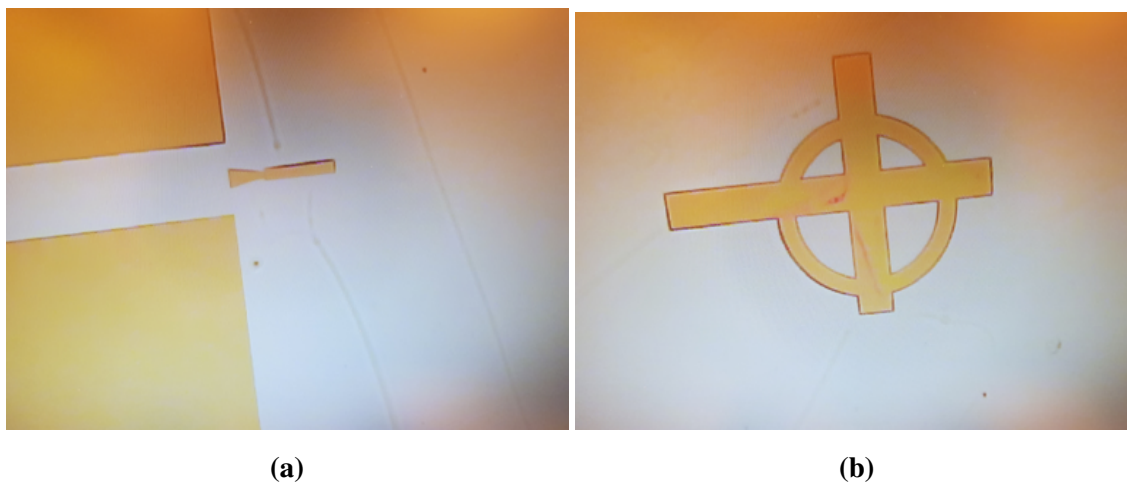
Figure 3.18: Silicon nitride was etched with PECVD using the CF4 plasma recipe. The area etched out shows the silicon oxide layer. (a) Spacers, taper, and base layer of photodetectors are shown. (b) Alignment mark made of silicon nitride.

closed, and the wafer is rotated to face the germanium target installed in the main chamber. Next, the sputtering machine starts to run. After finishing running the sputtering machine, the wafer is rotated back to the original position. After opening the valve again, the wafer is pull back to the small chamber. Before retrieving the wafer, it is necessary to confirm that the valve between the chambers is completely closed.

RF power was used instead of DC power for the deposition of germanium with the sputtering machine. DC power can be used for metals, but germanium is not metal. Therefore, RF power should be used for germanium. The germanium target is n-type, and the tool in Figure 3.19(b) was used to make sure whether the germanium was deposited or not. The tool in Figure 3.19(b) is connected to the four-point probes in Figure 3.19(a). The wafer sputtered was placed on the stage of 4 point probe, and the knob is pushed down carefully, as shown in Figure 3.19(a). The n-type light was turned on when pressing the button in Figure 3.19(b).

(a)   (b)

Figure 3.19: These tools were used to measure the wafer's doping type and are connected. A wafer is placed on the four-point probes' stage, and the knob is pushed down. Either the p-type or n-type light is on. (a) Wafer stage and knob. (b) JANDEL-1 letting know wafer's doping type.

The lift-off sequence of germanium is shown in Figure 3.24. Spin-coating, soft-bake, exposure, exposure-bake, development, and hard-bake were performed. The process patterning photoresist is the same as for the silicon nitride's patterning. After hard-bake for 3 minutes, 200 nm thickness germanium was sputtered, as shown in Figure 3.21. The wafer was entirely deposited with germanium for 30 seconds using the sputtering machine, as shown in Figure 3.23(a). The tool in Figure 3.20 was used for the lift-off of germanium. The germanium was patterned as shown in Figure 3.22.

The tool for lift-off in Figure 3.20 offered sonic energy to take off the photoresist under the germanium layer readily. The germanium layer on the photoresist was taken off along with the photoresist. DI water should be prepared in the tool up to the line, indicating the proper amount of DI water. The wafer was put into a petri dish with acetone. The petri dish was placed on the water in the tool for a minute to take off the photoresist. After the photoresist was removed from the wafer, the germanium was patterned.

Figure 3.20: Tool for lift-off, which offers sonic energy.

3.2.7. Aluminum Deposition and Patterning

After the deposition and lift-off of germanium, aluminum was deposited using the sputtering machine in Figure 3.23(a), and lift-off was done to make aluminum patterns. The lift-off process of aluminum is the same as the lift-off process used for germanium, and shown in Figure 3.26.

SPR3600 photoresist was used. Spin-coating, soft-bake, exposure, exposure-bake, development, and hard-bake were done in this process. After hard-bake, 50nm thickness aluminum was deposited using the sputtering machine. DC power was used since aluminum is metal.

(a)   (b)
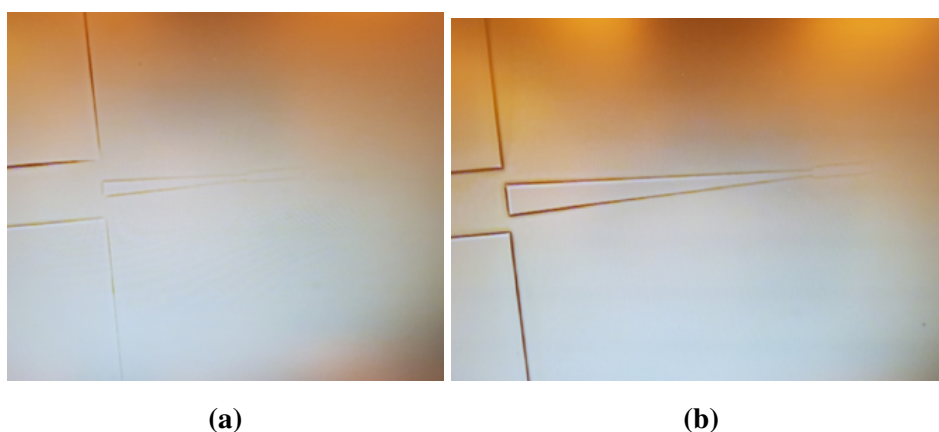
Figure 3.21: Germanium of 200 nm was sputtered on the wafer in Figure 3.18. It took 30 seconds to deposit germanium of 200 nm with the sputtering machine using RF power.

(a)   (b)
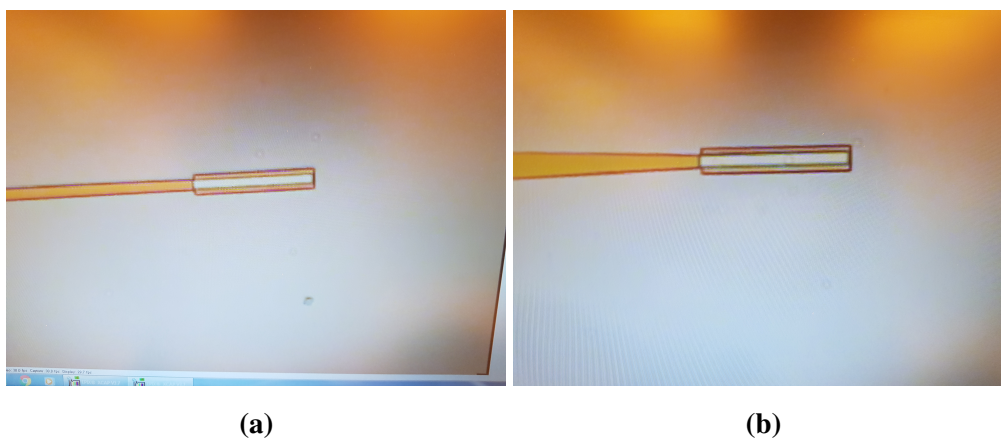
Figure 3.22: The patterned germanium after the lift-off process. The silicon nitride and germanium are formed as structures.
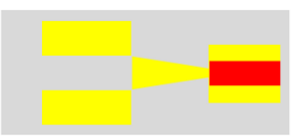
The tool in Figure 3.20 was used to take off the photoresist coated under the aluminum layer. The aluminum deposited on the photoresist was taken off along with the photoresist. DI water was prepared in the tool up to the line, indicating the proper amount of DI water. The wafer was put into a petri dish with acetone. The petri dish was placed on the water in the tool for three minutes to take off the photoresist fully. When the photoresist was removed from the wafer, the aluminum is patterned. The final wafer fabricated is shown in Figure 3.27.

The width of the aluminum electrodes was 5 μm since the width was unable to be made smaller than 4 μm due to the 4 μm resolution of photolithography in Figure 3.28(a). As shown in Figures 2.7 and 2.8, the photodetector's dark current increases as the germanium's geometry becomes larger. As shown in Figure 2.3, the photodetector's responsivity is 1.75 A/W which means 175 mA current will be detected if 100 mW laser is used. However, dark current will be critical if a

(a)   (b)
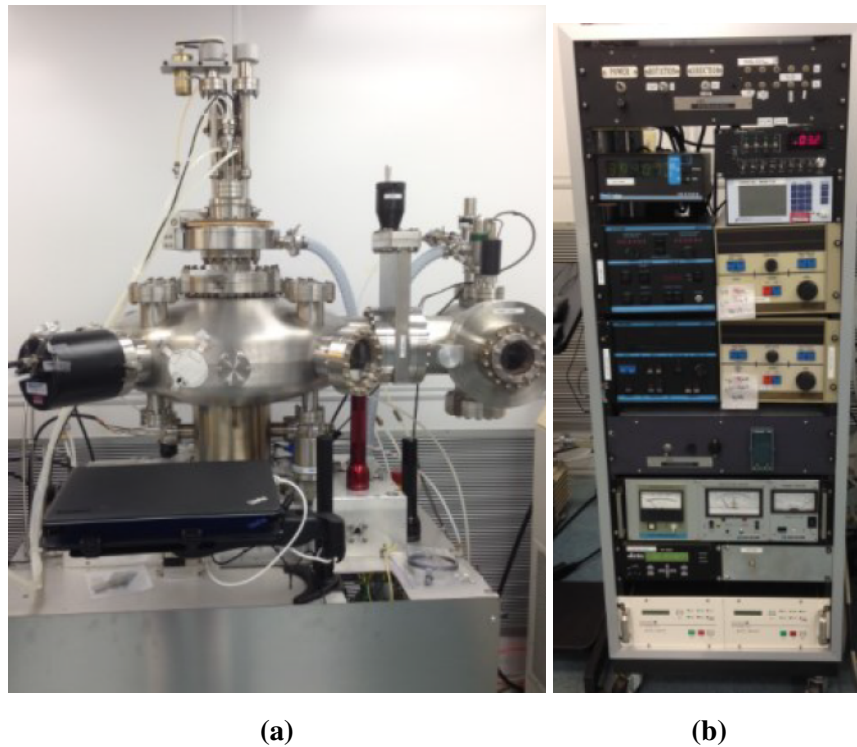
Figure 3.23: Sputtering machine with RF and DC powers. (a) Main chamber, valve, and small chamber. (b) RF, DC powers supplies and control electronics.

Figure 3.24: Fabrication process for lift-off to make patterns of germanium. SPR3600 photoresist is used in this process. Spin-coating, soft-bake for 1 minute, exposure, exposure-bake for 1 minute, development, and hard-bake for 3 minutes are done. After hard-bake, 200nm thickness germanium is sputtered, and lift-off is done.
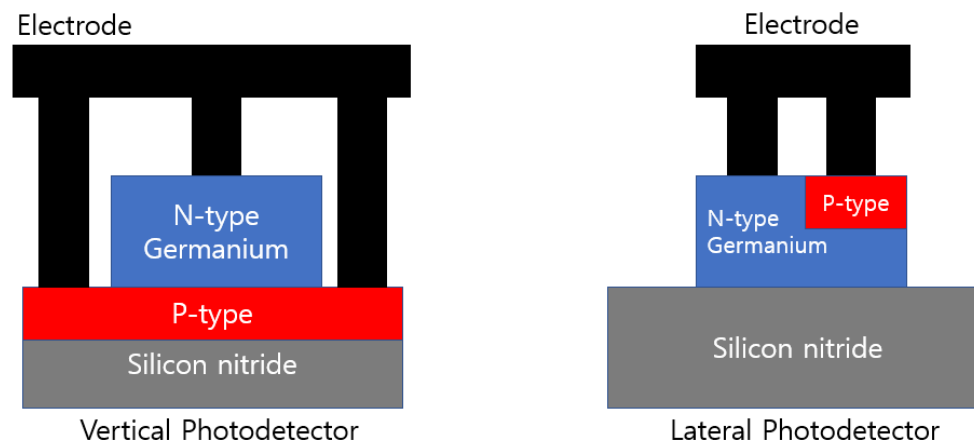
Figure 3.25: Vertical and lateral photodetectors. (a) After deposition of silicon nitride, silicon nitride is p-type doped with doping furnace, boron source target, and nitrogen gas. The germanium and aluminum are deposited after the doping process. (b) After deposition of silicon nitride and germanium, p-type doping is done. Deposition of aluminum is done after the doping process.

few photons should be detected since the power per photon is 19 nW and the photocurrent will be

20-30 nA which is too tiny to detect compared to 1880 μm dark current. This paper's aim is not to

1	Spin-coating of SPR3600		Si / SiO2 / SiN / SPR3600 / Ge / Al
2	Photo lithography		Soft-bake for 1 miniute Exposure with germanium photomask Post-exposure-bake for 1 minute Develop Post-bake for 3 minutes
3	Deposition of Aluminium		Grow Aluminium 0.05 μm thickness using the sputtering machine
4	Lift-off		
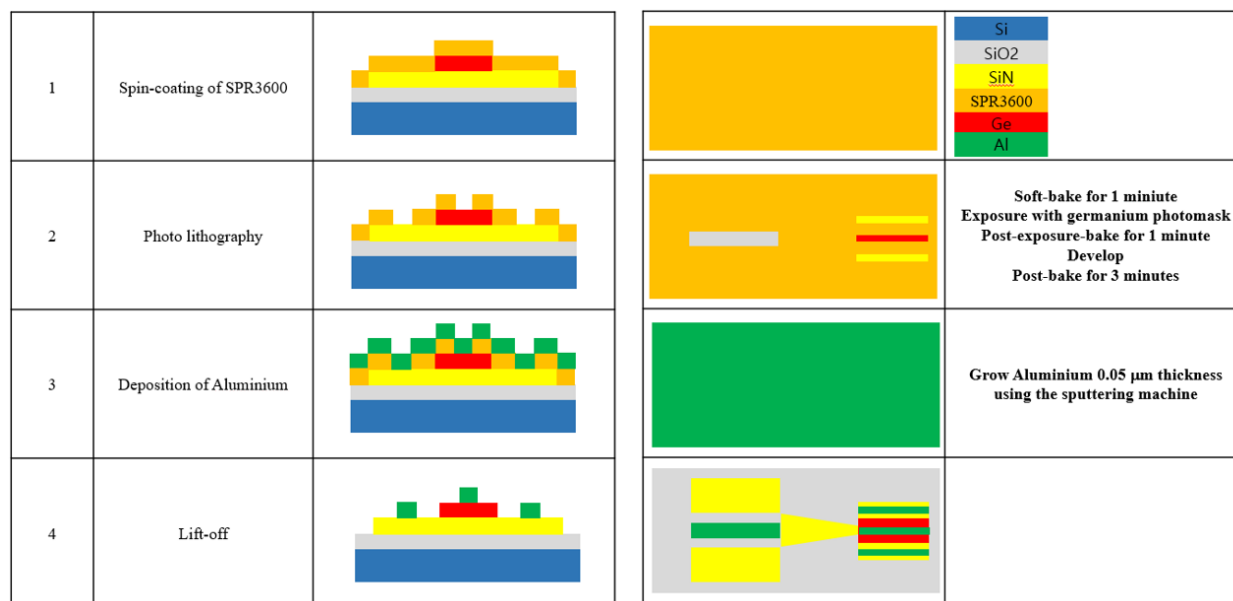
Figure 3.26: Fabrication process for lift-off to make patterns of aluminum. SPR3600 photoresist is used in this process, and spin-coating, soft-bake for 1 minute, exposure, exposure-bake for 1 minute, development, and hard bake for 3 minutes are done. After hard-bake, germanium of 50 nm is deposited, and lift-off is done.
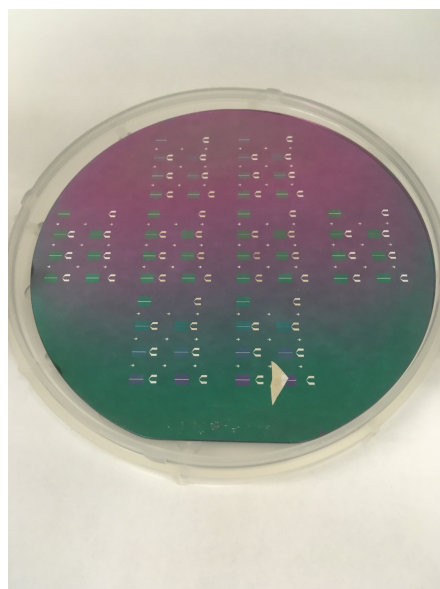
Figure 3.27: The wafer after lift-off of aluminum layer.

detect a few photons, so the dark current is not an issue. Therefore, photodetectors can be made larger than the ones fabricated in this paper. The two areas for cathode and anode were merged into one due to the narrow space between them, as shown in Figure 3.28(b). The space needs to be larger than 4 μm to reduce fabrication error.

(a)

(b)

(c)
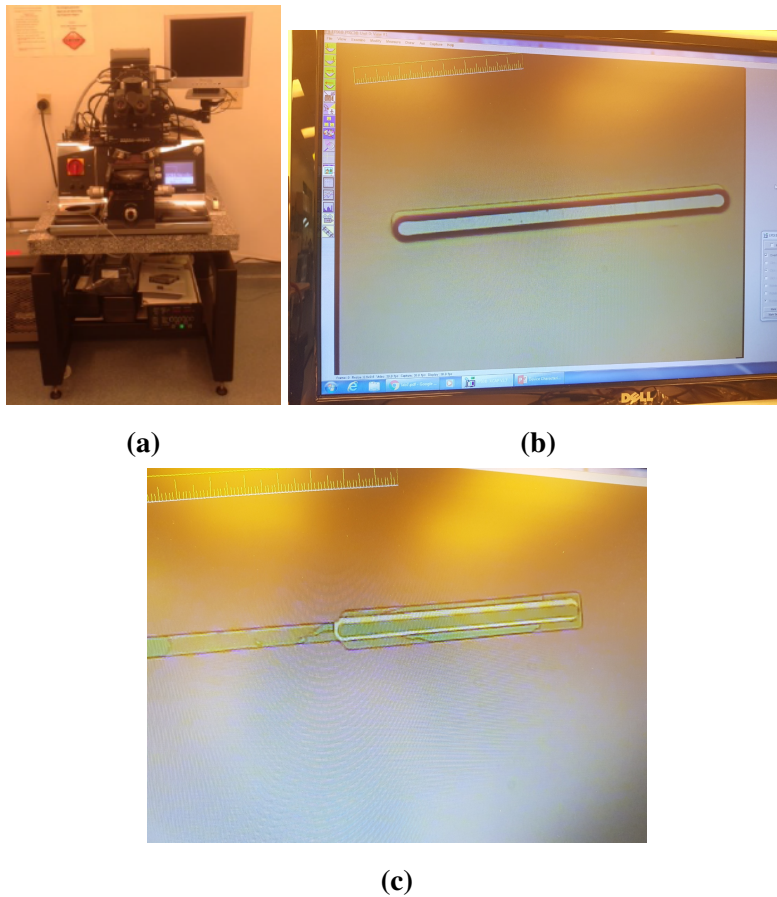
Figure 3.28: (a) Photolithography equipment in the cleanroom. (b) Due to the narrow space, the electrodes for cathode and anode were merged into one. (c) Germanium was vaporized during p-type doping in the doping furnace. HF solution was used to remove the hard mask and damaged the silicon nitride layer which has oxide in the film.

(a)   (b)
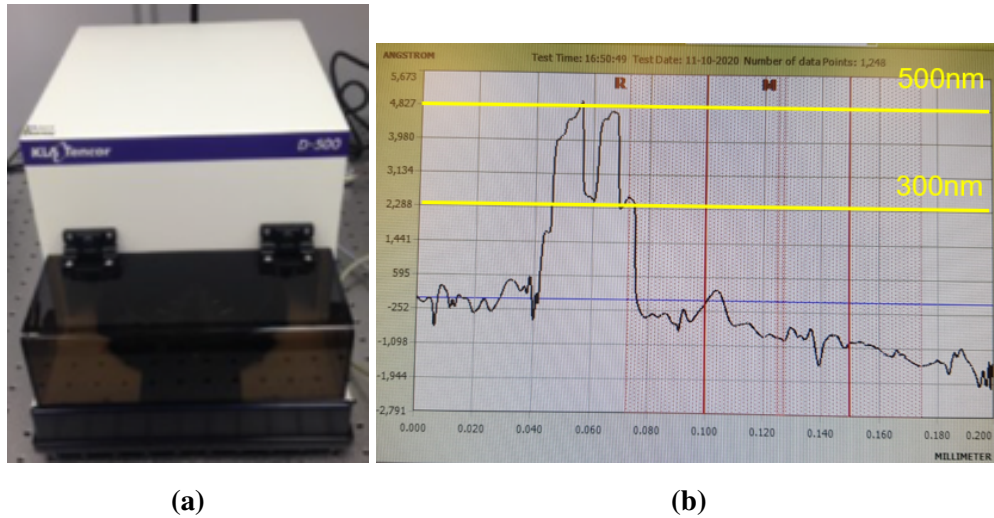
Figure 3.29: (a) Profilometer. (b) Image indicating that germanium was vaporized in the doping furnace.

(a)   (b)
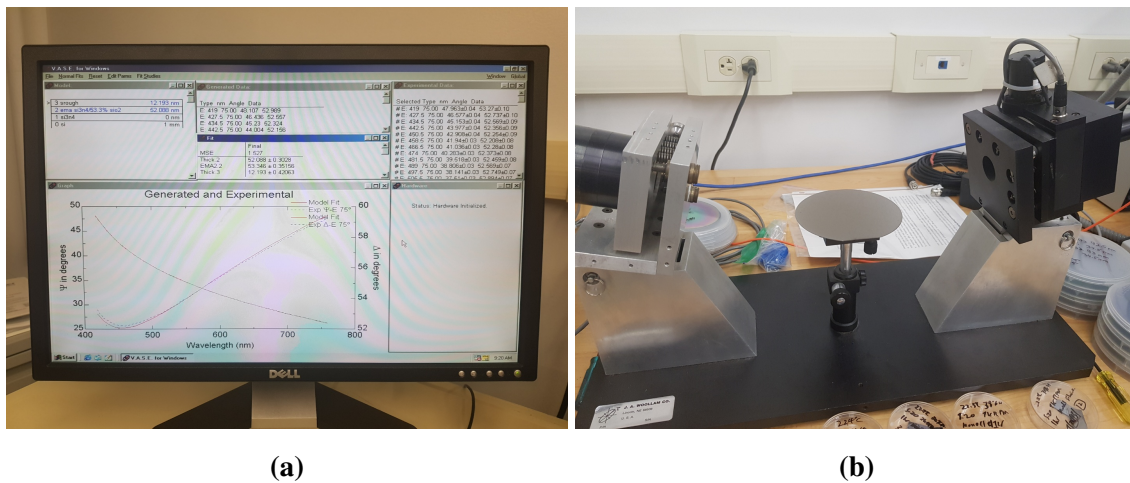
Figure 3.30: (a) Ellipsometer measured the silicon nitride layer that oxide was generated during the deposition of silicon nitride. (b) Ellipsometer used in this measurement.

4. Characterization of Photodetectors

The fabrication of the device with photodetectors and metal for prism coupling using the plasmonic effects was explained previously. Photodetector testing is discussed in this chapter.

4.1. Photodetectors

The testing of the IPEK was done as outlined in the Appendix. The optical spectrum analyzer was used to observe the data from the output ports. However, photodetectors fabricated in this thesis can be used to detect light. Figure 4.12 presents a vertical photodetector's configuration, and Figure 4.13 shows an experimental setup [21]. The setup in Figure 4.13 has been used to achieve edge coupling to a device.

The wafer fabricated was cleaved in X and Y directions, as shown in Figure 4.14, since the wafer's orientation is 100. The device fabricated is separated into two parts: a coupling part with metal using SPPs and a detecting part with a photodetector. The detecting part can be tested
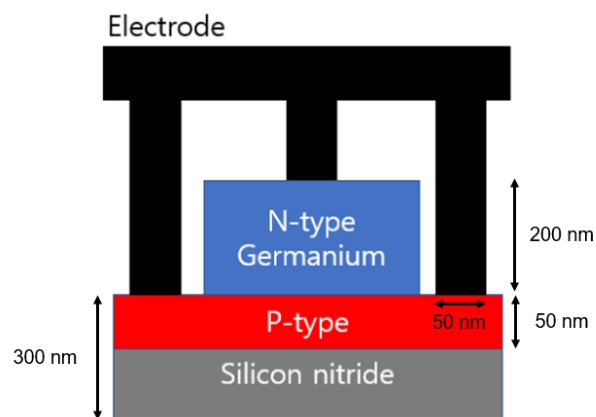
Figure 4.1: Configuration of the photodetector tested in this section. The thickness of the silicon nitride and the germanium are 300 nm and 200 nm, respectively. The aluminum's width is 50 nm. The doping depth is 50 nm.

alone without the coupling part, which can be cut off. Therefore, light can be coupled to the SiN tapered waveguide using the edge coupling and can be detected by observing a current variation. Unfortunately, the current variation was not observed due to fabrication errors and insertion loss.

The cleaved wafer placed on the vacuum chuck, and the best coupling was tried using a tapered fiber marked as 1 in Figure 4.13. A bias voltage of 1V using a power supply was applied to the chip using two probe tips marked as 5 and 6 in Figure 4.13. After the coupled light propagates in the SiN tapered waveguide, the light gets absorbed into the germanium, and the carrier generation should occur as a current variation.

Before fabricating the photodetectors, they were simulated. The simulations demonstrated that the photodetectors' performance are acceptable. Therefore, the photodetectors were designed and
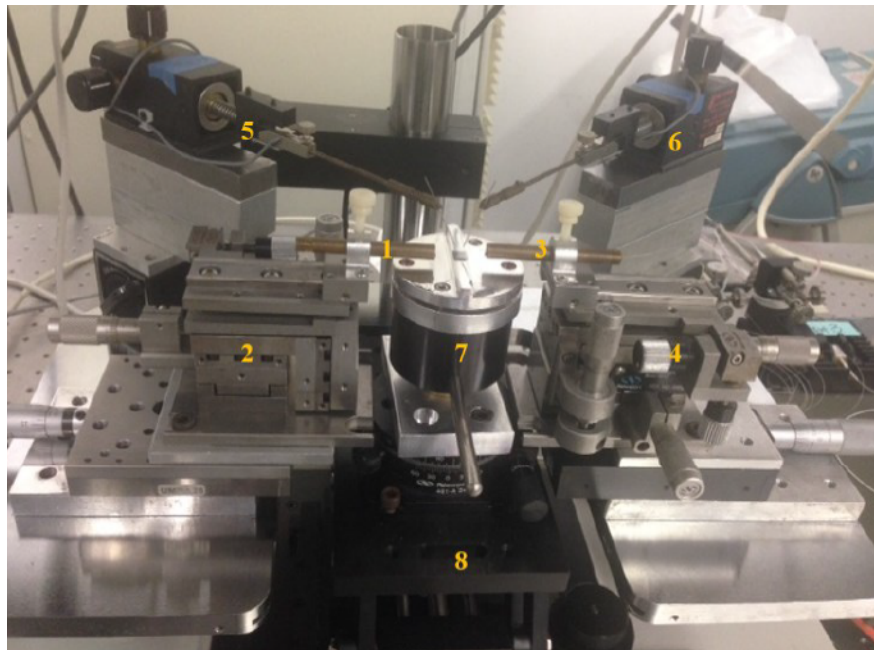
Figure 4.2: Experimental setup for the photodetector. The numbers 1 and 3 in yellow are for input and output fibers. The number 3 is not used since incident light is detected using the current variation. The numbers 2 and 4 in yellow are for XYZ translation stage. The numbers 7 and 8 are for stage and vacuum chuck. The numbers 5 and 6 are for probes that can be connected to cathode and anode to photodetectors. Voltage can be applied to the numbers 5 and 6 using a power supply [21].

modeled correctly. The reason, the current variation was not observed, can be found from the fabrication errors and the large insertion loss between the tapered fiber and the SiN tapered waveguide. As mentioned in the Fabrication, the SiN waveguide should be made with LPCVD since the SiN waveguide deposited using PECVD has silicon oxide in the film, and the silicon oxide generates propagation losses as defects [18]. Therefore, light disappears on the way to a photodetector due to the loss. The insertion loss is the second issue since the tapered fiber is manually coupled to the SiN tapered waveguide. The coupling system is very sensitive, and coupling to the SiN taper requires a great deal of effort. If the light is not exactly coupled to the SiN taper, then the huge insertion loss is produced to the system. To reduce the insertion loss, a robust coupling setup should be designed and tested.
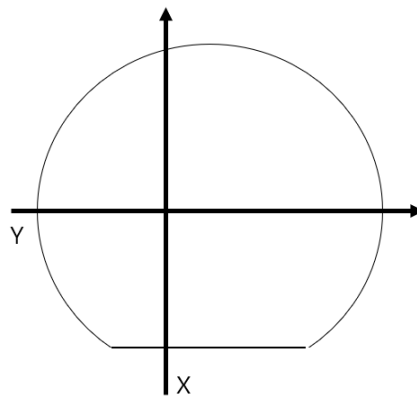
Figure 4.3: Since the wafer's orientation is 100, The wafer was cleaved in two ways: X and Y.

5.   CONCLUSIONS

The integrated device for evanescent coupling using surface plasmon polaritons (SPPs) and for PIN SiN-Ge photodiodes were designed, modeled, fabricated, and tested in this paper. The prism coupling using the plasmonic effects and photodetectors was simulated using Lumerical FDTD solution. The silicon photonic devices with MZI, ring resonator, directional coupler, and Bragg gratings were tested, and data were extracted and analyzed.

The FDTD simulation for the prism coupling presents that light is coupled to the nanoscale Al layer from a prism, and the Al metal delivers the light to the SiN tapered waveguide. The coupling efficiencies for Ag and Al are 60 % and 15 %, respectively. The Al film for the prism coupling can be detached using the cleaving method. Light can directly be coupled to the SiN tapered waveguide using the edge coupling and detected using the photodetector.

The IPEK utilized broadband and laser sources as input sources. The optical spectrum analyzer observed the light from the IPEK and extracted the data. The extracted data were compared to the simulation results in Appendix A.

Two types of SiN-Ge photodiodes were designed, one with ideal dimensions of 3.5 × 0.3 μm (W × H) and the other with dimensions of 15.5 × 0.2 μm (W × H). The latter geometry was considered for the photolithography resolution of 4 μm, which means the space between electrodes should be more than 4μm. The values of responsivity, 3dB bandwidth, and dark current for the dimensions of 3.5 × 0.3 μm (W × H) are +1.25 A/W, +12GHz, and +4.46 μA, respectively. The values of responsivity, 3dB bandwidth, and dark current for the dimensions of 15.5 × 0.2 μm (W × H) are +1.7 A/W, +1.8GHz, and +1.88 mA, respectively. The dark current becomes larger as the geometry becomes larger.

The SiN-Ge photodiode of 15.5×0.2 μ*m* was fabricated in the cleanroom with the four masks process. The four masks were drawn with KLayout. The silicon dioxide of 800 nm $\pm$ 10 nm was grown on a 100 oriented silicon wafer using the oxidation furnace. A silicon nitride recipe was made for this project, and the silicon nitride of 300 nm $\pm$ 10 nm was deposited using the PECVD. The silicon nitride was p-type doped with the doping furnace using a boron target. The silicon nitride was etched with the PECVD using the CF4 plasma etching. Germanium of 200 nm $\pm$ 10 nm was deposited with the magnetron sputtering using the RF power, and a lift-off process for the germanium was done. The aluminum for the prism coupling and electrodes were deposited, and the lift-off step for the aluminum layer was performed.

The setup for testing of the SiN-Ge photodiode was described in the Characterization of PIC chapter. The current variation should occur when light is coupled to the SiN tapered waveguide. However, unfortunately, any current variation was not observed due to fabrication errors and insertion loss between tapered fiber and the SiN tapered waveguide.

Propagation loss in SiN waveguides was huge due to many defects and fabrication errors. The PECVD has been used by many and thus contaminated. The contamination deteriorated the quality of the SiN films. Additionally, the PECVD had a small amount of oxygen gas in the chamber that generates silicon oxide in silicon nitride films [18]. The oxide in the SiN films is critical when HF solution is used to remove the oxide hard mask. Typically, silicon nitride does not interact with HF solution [19], but silicon nitride + oxygen starts to gradually etch. To resolve this issue, LPCVD should be used to deposit silicon nitride. LPCVD's silicon nitride quality is better than the PECVD's since LPCVD runs under lower pressure and at a higher temperature than PECVD.

For future research, first, it is recommended to prepare spin-on-dopants for germanium. Presently, the MiNDS cleanroom does not own p-type spin-on-dopants for germanium. It is inappropriate to

dope germanium in the furnace with oxygen gas since Ge is vaporized at around 400-500 °C. Spin-on-dopants do not require a high-temperature process. Hence, germanium can be doped using spin-on-dopants. It is recommended to test germanium doping using the RTA (Rapid thermal annealing) with aluminum dopant and nitrogen gas. Second, LPCVD's silicon nitride recipe should be made to resolve the issue associated with defects. The film's quality will be better if silicon nitride can be made in the vacuum furnace at a high temperature. Third, the cleanroom is recently equipped with the RTA. The RTA can be used to anneal many films. Amorphous silicon of sputtering machine or PECVD is annealed and turned into poly-silicon. Poly-silicon can be used as waveguides instead of silicon nitride.

LIST OF REFERENCES

[1]   Yongqian Li. *Plasmonic optics: Theory and applications*. SPIE Press Bellingham, 2017.

[2]   Daniel J Blumenthal et al. "Silicon nitride in silicon photonics". In: *Proceedings of the IEEE* 106.12 (2018), pp. 2209–2231.

[3]   Léopold Virot et al. "High-performance waveguide-integrated germanium PIN photodiodes for optical communication applications". In: *Photonics Research* 1.3 (2013), pp. 140–147.

[4]   Kazumi Wada. "Electronics and photonics convergence on Si CMOS platform". In: *Opto-electronic Integration on Silicon*. Vol. 5357. International Society for Optics and Photonics. 2004, pp. 16–24.

[5]   G Sun, F Chang, and RA Soref. "High efficiency thin-film crystalline Si/Ge tandem solar cell". In: *Optics Express* 18.4 (2010), pp. 3746–3753.

[6]   James Sharp et al. "A novel technique for degenerate p-type doping of germanium". In: *Solid-state electronics* 89 (2013), pp. 146–152.

[7]   Lukas Chrostowski and Michael Hochberg. *Silicon photonics design: from devices to systems*. Cambridge University Press, 2015.

[8]   Amit Khanna et al. "Impact of ALD grown passivation layers on silicon nitride-based integrated optic devices for very-near-infrared wavelengths". In: *Optics Express* 22.5 (2014), pp. 5684–5692.

[9]   Sina Ebnesajjad and Cyrus Ebnesajjad. *Surface treatment of materials for adhesive bonding*. William Andrew, 2013.

[10]   I Fränz and W Langheinrich. "Conversion of silicon nitride into silicon dioxide through the influence of oxygen". In: *Solid-State Electronics* 14.6 (1971), pp. 499–505.

[11]   Zhiyong Mao et al. "Investigation of Al-doped silicon nitride-based semiconductor and its shrinkage mechanism". In: *CrystEngComm* 14.23 (2012), pp. 7929–7933.

[12]   YK Fang et al. "Preparation and Characterization of Boron-and Phosphorus-Doped Hydrogenated Amorphous Silicon Nitride Films". In: *Journal of the Electrochemical Society* 132.5 (1985), p. 1222.

[13]   Simon M Sze and Kwok K Ng. *Physics of semiconductor devices*. John wiley & sons, 2006.

[14]   Zhemin Chen, Jaehoon Jeong, and Azad Siahmakoun. "Modeling and simulation of evanescent coupling to Si waveguides using SPP". In: *Plasmonics: Design, Materials, Fabrication, Characterization, and Applications XVIII*. Vol. 11462. International Society for Optics and Photonics. 2020, p. 114622M.

[15]   LC Oliveira et al. "Optical properties and instrumental performance of thin noble metal (Cu, Au, Ag) films near the surface plasmon resonance". In: *Procedia Engineering* 168 (2016), pp. 834–837.

[16] Sergio G Rodrigo, FJ García-Vidal, and L Martín-Moreno. "Influence of material properties on extraordinary optical transmission through hole arrays". In: *Physical Review B* 77.7 (2008), p. 075401.

[17] Motahar Hossain, Kinichi Morita, Toshikazu Kawaguchi, et al. "Effect of Metal Film Thickness and Various Solvents on the SPR Biosensor Sensitivity for Illegal Compound Detection". In: *Oriental Journal of Chemistry* 34.3 (2018), p. 1355.

[18] D Virzonis et al. "Advanced Process Equipment for PECVD Silicon Nitride Deposition–an Experimental Study". In: *Mater. Sci* 12 (2006), pp. 4–37.

[19] Kirt R Williams, Kishan Gupta, and Matthew Wasilik. "Etch rates for micromachining processing-Part II". In: *Journal of microelectromechanical systems* 12.6 (2003), pp. 761–778.

[20] A Ohta et al. "Dry oxidation of germanium (100) and (111) surfaces–impact of oxidation Temperature on Ge oxide growth". In: *Proc. International Conference on Solid State Devices and Materials*. 2012, pp. 743–744.

[21] Yeongho Park. "Fabrication and Characterization of Thermo-Optic Mach-Zehnder Silicon Modulator". In: (2017).

[22] Amnon Yariv. "Coupled-mode theory for guided-wave optics". In: *IEEE Journal of Quantum Electronics* 9.9 (1973), pp. 919–933.

[23] Amnon Yariv and Pochi Yeh. *Photonics: optical electronics in modern communications*. Vol. 6. Oxford university press New York, 2007.

[24] Nicolas Rouger, Lukas Chrostowski, and Raha Vafaei. "Temperature effects on silicon-on-insulator (SOI) racetrack resonators: A coupled analytic and 2-D finite difference approach". In: *Journal of Lightwave Technology* 28.9 (2010), pp. 1380–1391.

[25] Yi Zhang et al. "A compact and low loss Y-junction for submicron silicon waveguide". In: *Optics Express* 21.1 (2013), pp. 1310–1316.

[26] Wim Bogaerts et al. "Silicon microring resonators". In: *Laser & Photonics Reviews* 6.1 (2012), pp. 47–73.

[27] Jens Buus, Markus-Christian Amann, and Daniel J Blumenthal. *Tunable laser diodes and related optical sources*. John Wiley & Sons, 2005.

[28] Di Wang et al. "Influence of intra-cavity loss on transmission characteristics of fiber Bragg grating Fabry–Perot cavity". In: *Chinese Physics B* 27.2 (2018), p. 024207.

APPENDICES

APPENDIX - LUMERICAL CODES

A.1. Directional Couplers

The directional coupler is one of the useful methods of combining and splitting light in silicon photonic circuits. The directional coupler has two parallel waveguides and we can determine the coupling coefficient, which is adjusted by the length of the two waveguides and the gap between the two waveguides. Any type of waveguides, such as rib waveguides or strip waveguides, can be used for designing directional couplers. An example of a directional coupler is shown in Figure 1. Using coupled-mode theory [22, 23], behavior of a directional coupler can be found. The below equation expresses the fraction of the power coupled to the other waveguide from the input waveguide: [7]

$$\kappa^2 = \frac{P_{cross}}{P_0} = sin^2 (C \cdot L) \tag{1}$$

The coupling coefficient is C, L is the coupler length, P_{cross} is the coupled optical power, and P_0 is the input optical power. Each port is called as input, through, coupled, and isolated in clockwise from 11 o'clock. Assuming lossless directional coupler, $(\kappa^2 + t^2 = 1)$ [7], The fraction of the
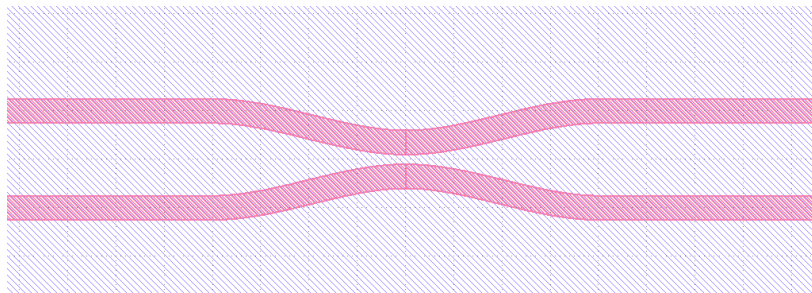
Figure 1: Directional coupler layout in GDS file.

power in through port is given by:

$$t^2 = \frac{P_{through}}{P_0} = cos^2\left(C \cdot L\right) \tag{2}$$

n_1 and n_2 are the first two effective indices of a directional coupler. There are several ways to obtain the coupling coefficient such as "supermode" analysis of a numerical calculation dealing with the first two eigenmodes. Two eigenmodes are shown in Figure 2 and they are known as the symmetric and antisymmetric supermodes [7].

The supermode analysis is called the eigenmode expansion method and useful to strong coupling of high-index contrast waveguides. The coupled mode theory approach, which the coupling coefficient is found by perturbation methods, can be used instead.

$$C = \frac{\pi \Delta n}{\lambda} \tag{3}$$

Δn is n_1-n_2. Two propagation constants using two effective indices in Equations 4 and 5 can be obtained. These two propagation constants has individual Real(E_y) and E-field intensity.

$$\beta_1 = \frac{2\pi n_1}{\lambda} \tag{4}$$

$$\beta_2 = \frac{2\pi n_2}{\lambda} \tag{5}$$

When the first two modes are in-phase, the power becomes localized in the upper waveguide, but when they are out-of-phase, specifically π, the power becomes localized in the lower waveguide. This phenomenon occurs after, L_x, the cross-over length.

$$\beta_1 L_x - \beta_2 L_x = \pi$$

$$L_x \left[\frac{2\pi n_1}{\lambda} - \frac{2\pi n_2}{\lambda} \right] = \pi$$

$$L_x = \frac{\lambda}{2\Delta n} \tag{6}$$

The cross-over length versus the gap is shown in Figure 3. The coupling coefficient depends on
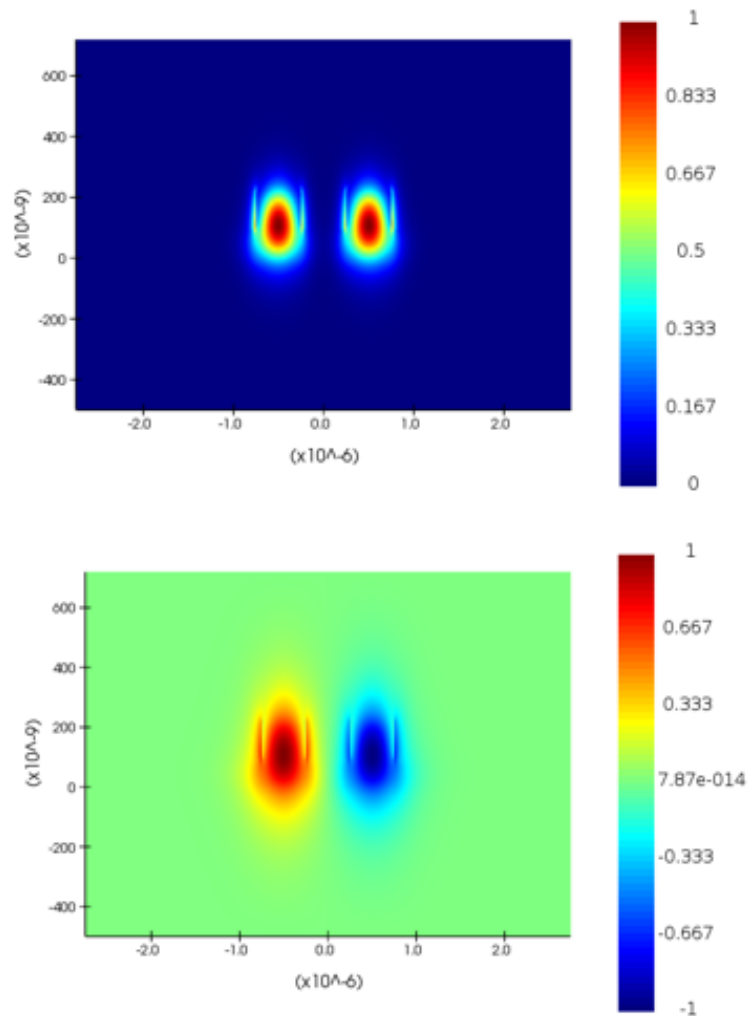
Figure 2: The wavelength used in this device is 1550nm, coupler gap is 200nm, The waveguide in this directional coupler has a shape of 500nm x 220nm waveguides with a 90nm slab. The upper figure is the symmetric supermode and the lower figure is antisymmetric supermode.

the gap between two waveguides, g as presented in Equation 7.

$$C = B \cdot e^{-A \cdot g} \tag{7}$$

From Equation 7, A and B depend on the coupler geometry, wavelength, and so forth. Equation 8 is for the geometry of strip waveguide (500 x 220 nm with 90 nm slab), similar to the reference [24].

$$L_x = 10^{0.0026084 * g[nm] + 0.657094} [\mu m] \tag{8}$$

The field directional coupling coefficient, κ, shown in Equation 9 is calculated using Equation 8.
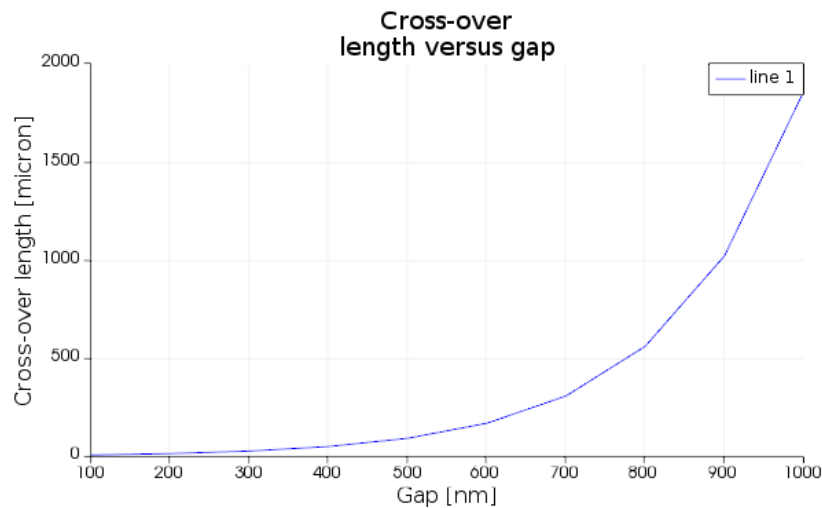
Figure 3: **Cross-over length versus gap. The wavelength used in this device is 1550nm and the coupler gap is 200nm. The waveguide in this directional coupler has a shape of 500nm x 220nm waveguides with a 90nm slab.**

$$\kappa = \left[\frac{P_{Coupled}}{P_0}\right]^{1/2} = \left|sin\frac{\pi\Delta n}{\lambda}\cdot L\right|$$

$$= \left|sin\frac{\pi}{2}\cdot\frac{z}{L_x}\right| \tag{9}$$

The field-coupling, κ, of a directional coupler with 5 μm and 15 μm coupler length are shown in the reference [24]. The data points in the reference are calculated using the eigenmode solver [24]. The solid lines are obtained using Equation 8. The error is observed due to small gaps. Zero coupling coefficient is shown when a directional coupler has 100 μm coupler gap and 15 μm long coupler since the cross-over length of 15 μm long coupler is 8 μm and all the power gets returned to the upper waveguide.

Sine and cosine shape plots are calculated using Equation 9. Equation 9 is used to determine parameters, such as gap and coupler length, and to design a directional coupler with a coupling power ratio, e.q., 30%. The plots in Figure 4 show wavelength dependence.
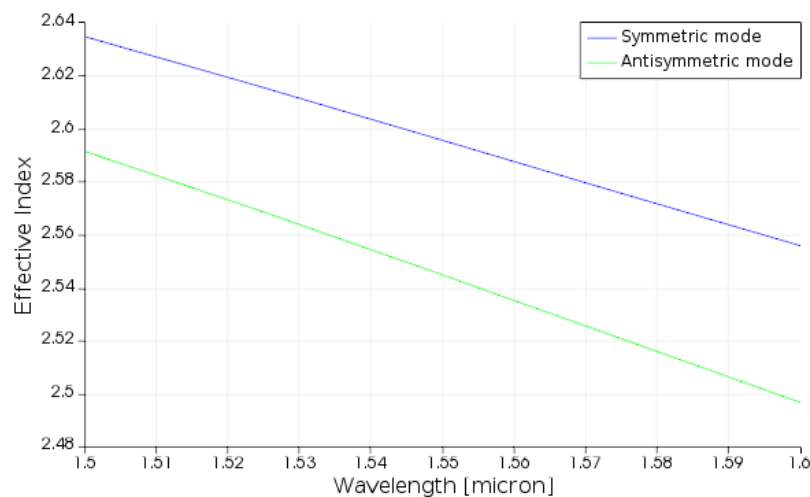
Figure 4: Wavelength dependence is shown. The wavelength used in this device is 1550nm and coupler gap is 200nm. The waveguide in this directional coupler has a shape of 500nm x 220nm waveguides with a 90nm slab.

The symmetric field profile in Figure 5 is illustrated as Mode 1 and the asymmetric field profile in Figure 5 is illustrated as Mode 2. The upper and lower waveguide in Figure 2 are labelled as wg A and wg B.

$$E_{wgA} = frac1\sqrt{2}\left(e^{i\beta_1 L} + e^{i\beta_2 L}\right)$$
$$E_{wgA} = frac1\sqrt{2}\left(e^{i\beta_1 L} + e^{i\beta_2 L} - i\pi\right) \tag{10}$$

The asymmetric Mode 2 has a phase shift of π in the negative field component in wg B. The phase shift can be calculated using Equations 10 and 11 and it is shown in Figure 5.

$$\angle E_{wgA} = \frac{\beta_1 + \beta_2}{2}L$$
$$\angle E_{wgB} = \frac{\beta_1 + \beta_2}{2}L - \frac{\pi}{2}$$
$$\angle E_{wgB} - \angle E_{wgA} = -\frac{\pi}{2} \tag{11}$$

The phase shift can be introduced in t and κ in Equation 12.
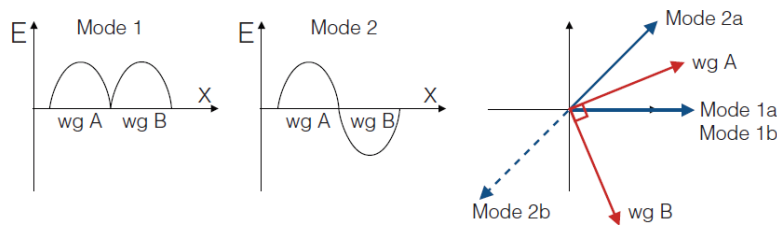
Figure 5: The two eigenmodes illustrated as Mode 1 and Mode 2, and Phase relationship. The wavelength used in this device is 1550nm and coupler gap is 200nm. The waveguide in this directional coupler has a shape of 500nm x 220nm waveguides with a 90nm slab [24].

$$t = |t|^2 \cdot e^{\frac{\beta_1 + \beta_2}{2} L}$$

$$\kappa = |\kappa|^2 \cdot e^{i \frac{\beta_1 + \beta_2}{2} - i \frac{pi}{2}} \tag{12}$$

$$t = |t|^2$$

$$\kappa = |\kappa|^2 \cdot e^{-i \frac{\pi}{2}} = -i |\kappa|^2 \tag{13}$$

A.2. Y-branch

Y-branch equally splits the light into two waveguides from one waveguide or combines the light into one waveguide from two waveguides. An example is shown in Figure 6. The ideal Y-branch is to split the intensity of the light into 50/50% for each output intensity. The intensity of the each output has $I_1 = I_2 = I_i/2$, which I_i is intensity of an input light. The electric field of the each output has $E_1 = E_2 = E_i / \sqrt{2} \left(since\ I \propto |E|^2 \right)$. But, for the combiner, it is impossible to combine two incoherent light into one waveguide to raise the power of light. For the combiner, if light is present in either of two waveguides, then the output light will decrease into a half of the light. The actual Y-branches have excess loss and are unable to exactly split the light into 50/50% for each output intensity. The geometry of Y-branches should be optimized using simulation program such as FDTD. For FDTD, the simulation program will adjust the shape of Y-branches using genetic algorithm and the insertion loss will be less 0.3 dB [25].

In Figure 7, light is split equally between two waveguides, the insertion loss is slightly over 10 dB, and the splitter has the excess loss as we expect.

In Figure 8, light is launched at the upper waveguide of the combiner. The combiner has two

modes, the fundamental mode and the second order mode. The insertion loss is lower than the one in Figure 7.
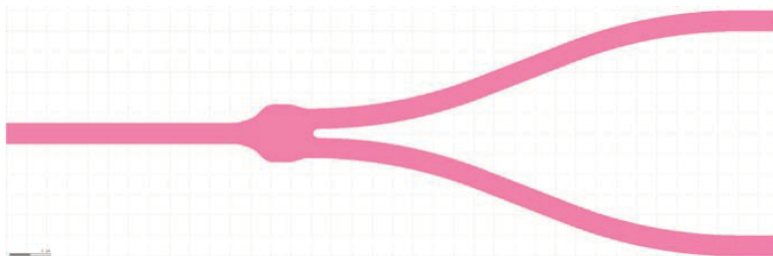
Figure 6: Y-branch layout in GDS file.
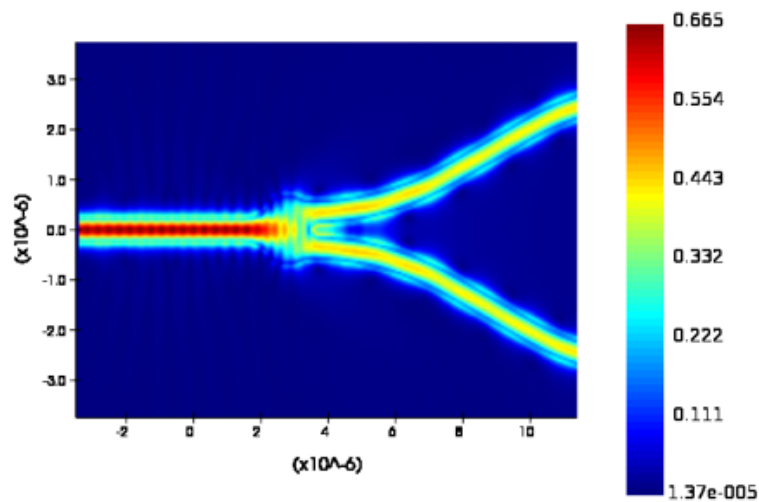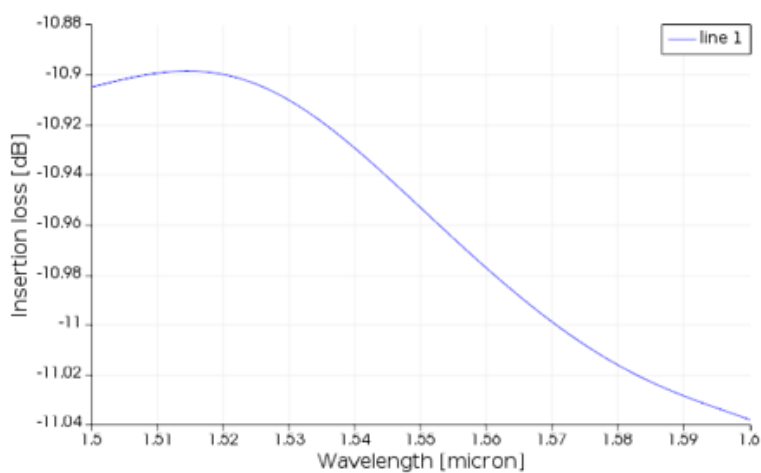
Figure 7: Field profile and insertion loss of the Y-branch as splitter

The simulation in Figure 9 considers two in-phase inputs in the combiner; in this situation, the two sources are coherent hence constructive interference is observed in the fundamental mode of the output port, as shown in Figure 9. In this case, the power in the waveguide should approach 100%. The deviation from this is known as the "excess loss" of the device, and is plotted in Figure 9 as a function of wavelength. The simulation in Figure 10 considers two out-of-phase inputs in the combiner; Destructive interference is observed in the fundamental mode of the output port, as shown in Figure 10. In this case, the power in the fundamental mode of the waveguide should approach 0%, with all the power going into the second-order TE mode or into radiation modes.
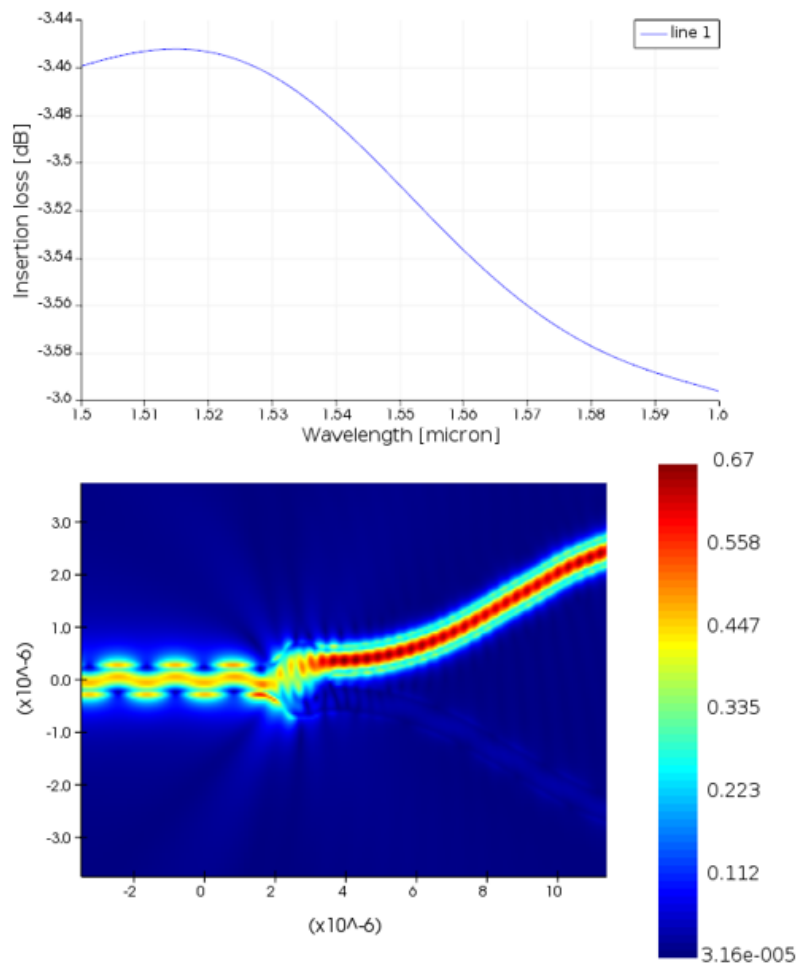
Figure 8: Field profile and insertion loss of the Y-branch as combiner

A.3. Mach-Zehnder interferometer

Figure 11 shows a Mach-Zehnder interferometer drawn with a Layout program. It is shortly called MZI. MZI consists of two Y-branches and two waveguides, which have different length each. Directional couplers can be used instead of Y-branches within MZI.

Input intensity is I_i and electric field is E_i. The input intensity is divided into two branches. At the upper branch, the field is $E_1 = E_i/\sqrt{2}$ and, at the lower branch, the field is $E_2 = E_i/\sqrt{2}$. The propagation constant of the two branches (waveguides) are $\beta_1 = \frac{2\pi n_1}{\lambda}$ and $\beta_2 = \frac{2\pi n_2}{\lambda}$ respectively.
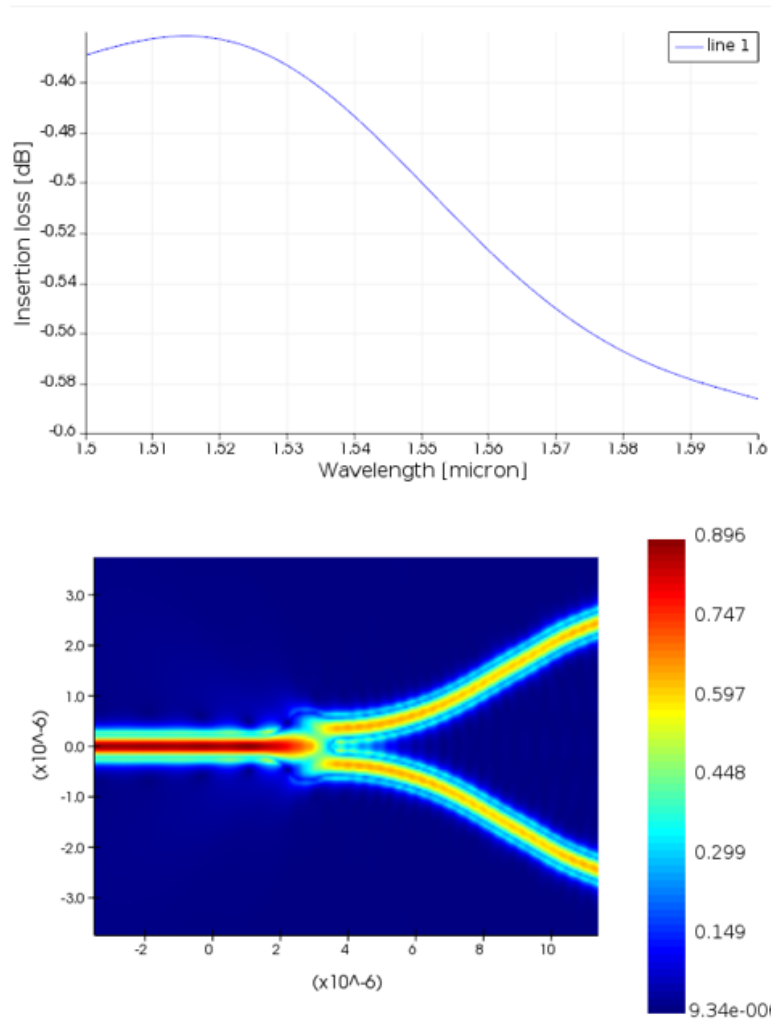
Figure 9: Simulations of the Y-branch operating as combiner with two in-phase inputs

The waveguides have lengths of L_1 and $L_2 = L_1 + \Delta L$, respectively. Propagation losses are α_1 and

α_2 (Equation 14). So, at the end of the branches, the fields are described in Equation 15.
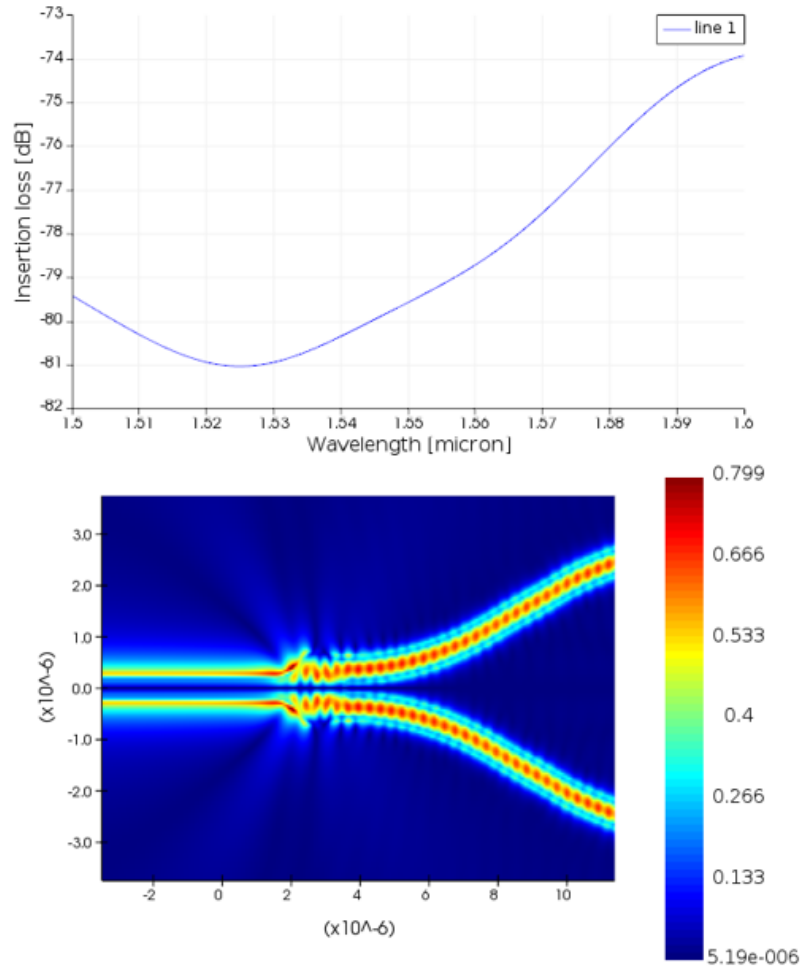
Figure 10: Simulations of the Y-branch operating as combiner with two out-of-phase inputs.

Figure 11: Simple example of Mach-Zehnder interferometer [7].

$$\alpha\left|m^{-1}\right| = \frac{\alpha\left|dB/m\right|}{10log_{10}\left(e\right)} = \frac{\alpha\left|dB/m\right|}{4.34}$$

$$k = \frac{\lambda\alpha\left|dB/m\right|}{4\pi\cdot 4.34} \tag{14}$$

$$E_{o1} = E_1 e^{-i\beta_1 L_1 - \frac{\alpha_1}{2}L_1} = \frac{E_i}{\sqrt{2}}e^{-i\beta_1 L_1 - \frac{\alpha_1}{2}L_1}$$

$$E_{o2} = E_2 e^{-i\beta_2 L_2 - \frac{\alpha_2}{2}L_2} = \frac{E_i}{\sqrt{2}}e^{-i\beta_2 L_2 - \frac{\alpha_2}{2}L_2} \tag{15}$$

The output of the second Y-branch is described in Eqaution 16.

$$E_o = \frac{1}{\sqrt{2}}\left(E_{o1} + E_{o2}\right) = \frac{E_i}{2}\left(e^{-i\beta_1 L_1} + e^{-i\beta_2 L_2 - \frac{\alpha_2}{2}L_2}\right) \tag{16}$$

The intensity at the output of the second Y-branch is described in Eqaution 17.

$$I_o = \frac{I_i}{4}\left|e^{-i\beta_1 L_1 - \frac{\alpha_1}{2}L_1} + e^{-i\beta_2 L_2 - \frac{\alpha_2}{2}L_2}\right|^2 \tag{17}$$

Equation 17 can be simplified as Equation 18 after some trigonometry manipulation.

$$I_o = \frac{I_i}{4}\left|2\cos\frac{\beta_1 L_1 - \beta_2 L_2}{2}\right|^2$$

$$= I_i\cos^2\frac{\beta_1 L_1 - \beta_2 L_2}{2} \tag{18}$$

$$= \frac{I_i}{2}\left|1 + \cos\beta_1 L_1 - \beta_2 L_2\right|$$

Equation 18, the output of MZI, is sinusoidally varying as a function of wavelength ($\beta_1 = \frac{2\pi n_1}{\lambda}$ and $\beta_2 = \frac{2\pi n_2}{\lambda}$) for an imbalanced MZI ($L_1 = L_2$). FSR, free spectral range, is period and determined

using Equation 19.

$$FSR\,|Hz| = \frac{c}{n_g \Delta L}$$

$$FSR\,|m| = \frac{\lambda^2}{n_g \Delta L} \tag{19}$$

In Equation 19, c is the speed of light in vacuum, and n_g is the waveguide group index in Equation 20. The intensity also varies with the waveguide effective index (n_1 and n_2), which is related with thermo-optic effect and the plasma dispersion effect. These effects are considered to implement a thermo-optic switch or a high-speed Mach–Zehnder modulator.

$$n_g(\lambda) = n_{eff}(\lambda) - \lambda \frac{dn_{eff}}{d\lambda} \tag{20}$$
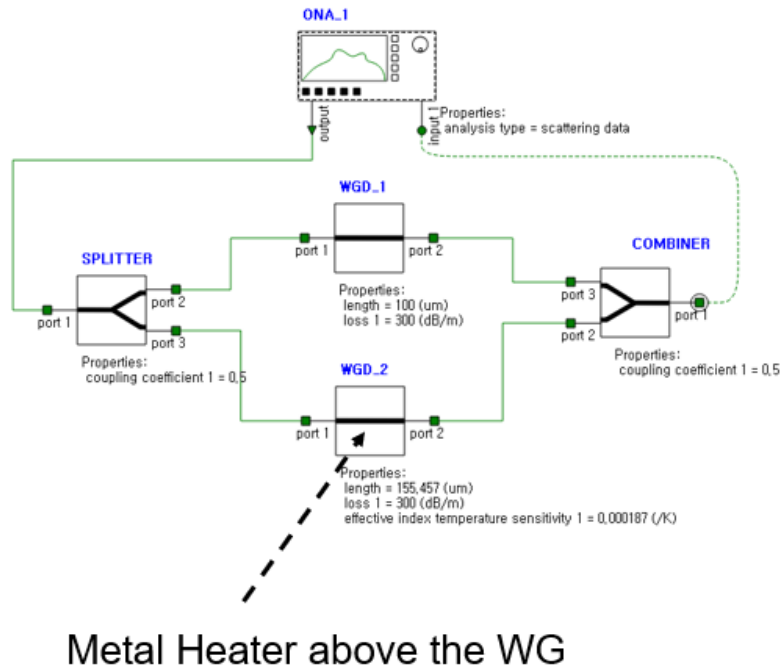
Figure 12: MZI layout drawn by using Lumerical program

Figures 12 and 13 show the simulation for MZI.

A.4. Ring resonators

Ring resonator consists of a loop of waveguide with some coupling to the outside world. The loop is typically a shape of circle. In Figure 14, ring resonator consists of one or two-directional couplers, which are called All-pass or Add-drop respectively. The ring resonator cavity consists of two straight waveguides for directional couplers and two half circular waveguides as shown in Figure 15 [26].

Equation 21 describes the roundtrip length.

$$L_{rt} = 2\pi r + 2L_c$$

(21)

Bend radius is defined by r. L_c is the directional coupler length. $L_c = 0$ Means that the coupler
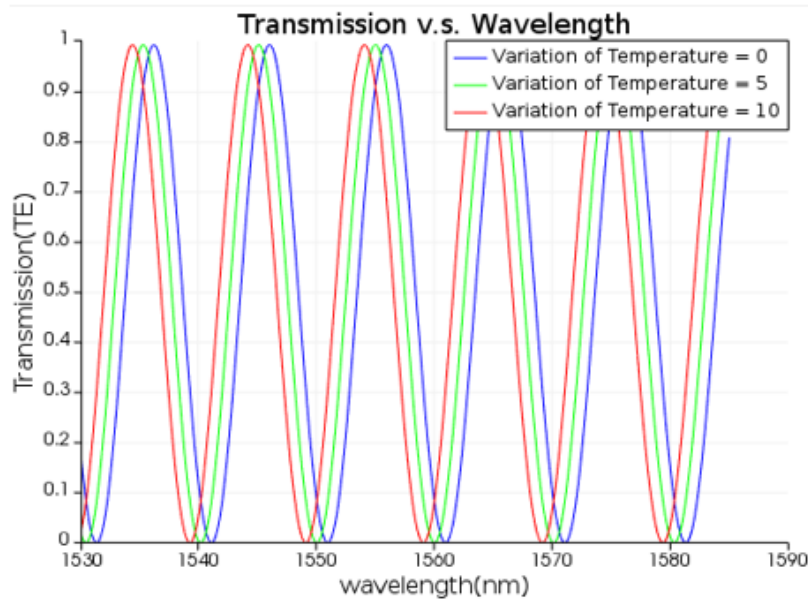
Figure 13: Transmission versus wavelength for MZI, FSR is 10 nm, Difference between waveguides is 55.46 μm, Loss is 3 dB/cm

length is 0 and ring resonator is point-coupled and the cavity becomes a circle. Equation 22
describes through-port response of an All-pass ring resonator.

$$\frac{E_{thru}}{E_{in}} = \frac{-\sqrt{A} + t e^{-i\theta_{rt}}}{-\sqrt{A} t^* + e^{-i\theta_{rt}}} \tag{22}$$

$$\theta_{rt} = \beta L_{rt}$$

$$A = e^{-\alpha L_{rt}} \tag{23}$$

A is power attenuation and θ_{rt} is the roundtrip phase. t_1 is the straight coupling coefficient and
κ_1 is cross-over coupling coefficient. * stands for complex conjugate. Point-coupling coefficients
are defined by t and k in Figure 14.

$$\frac{E_{thru}}{E_{in}} = \frac{t_1 - t_2^* \sqrt{A} e^{i\theta_{rt}}}{1 - \sqrt{A} t_1^* t_2^* e^{i\theta_{rt}}}$$

or

$$|\tau_{11}| = \sqrt{\left(\frac{n_g \cdot L \cdot \pi}{2 \cdot Q \cdot \lambda}\right)^2 + 1} - \frac{n_g \cdot L \cdot \pi}{2 \cdot Q \cdot \lambda} \tag{24}$$

$$\frac{E_{drop}}{E_{in}} = \frac{\kappa_1^* \kappa_2 A^{frac14} e^{i\theta_{rt}/2}}{1 - \sqrt{A} t_1^* t_2^* e^{i\theta_{rt}}}$$

(a) All-pass   (b) Add-drop
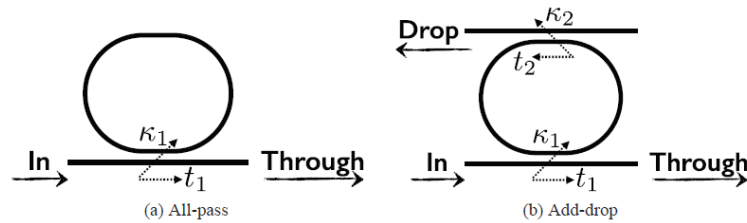
Figure 14: Two types of ring resonators [7].

In Equation 24, E_{thru} and E_{drop} are the optical field of the through-port and the drop-port.

In Equation 24, t_1, κ_1, t_2, and κ_2 are the straight through and cross-over coupling coefficients of Through and Drop ports. Assuming ring-resonator is lossless, Equation 25 is satisfied. The optical losses is incorporated into the cavity.

$$|\kappa|^2 + |t|^2 = 1 \tag{25}$$

$$n_g = \frac{\lambda^2}{L\Delta\lambda}$$

or

$$L = \frac{c}{n_g \cdot FSR} \tag{26}$$

or

$$FSR = \frac{\lambda^2}{n_g \cdot L}$$

Figures 15 and 16 are simulations for ring resonator. E-field is shown in Figure 15 and three resonances are shown in Figure 16. Group index and Q factor can be calculated using Lumerical and total length of the ring related to desired FSR can be calculated using Equation 26. Transmission in through port of the ring resonator can be obtained using the equation 24.

A.5. Bragg grating filters

Bragg grating is used in various application areas such as semiconductor laser and fibers, and helps achieve wavelength selective function [7].

As a simple and uniform Bragg grating shown in Figure 17, the Bragg grating has a periodic structure of waveguide in the light direction travelling.

Reflections of light propagating in the Bragg grating occur at each boundary. The multiple and distributed reflections and phase shift of the reflections can be adjusted designing the period,
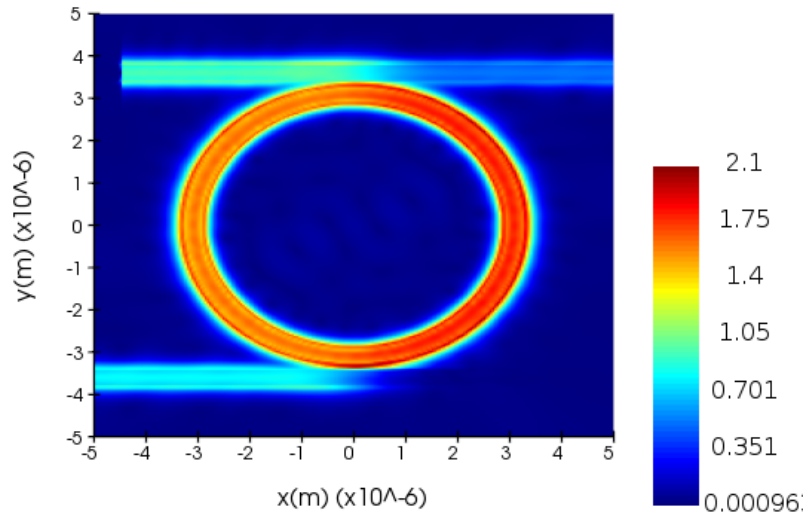
Figure 15: E-field for ring resonator and wavelength is 1.55 μ*m* and FSR is 25.6 nm and Q factor is 2000.
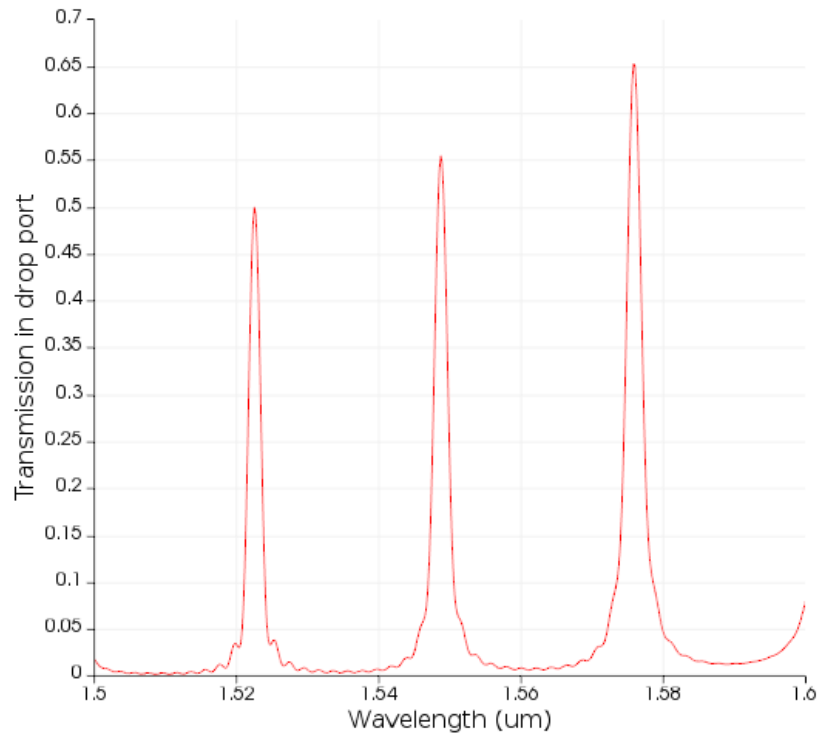
Figure 16: Transmission in drop port versus wavelength and FSR is 25.6 nm and Q factor is 2000.

Λ, and determining the light wavelength. Light only interferes constructively around the Bragg wavelength ($\Delta(\lambda)$) and is reflected, strongly. As shown in Figure 18, light within $\Delta(\lambda)$ is strongly reflected. The light reflected out of range of ($\Delta(\lambda)$) interferes destructively and disappears.
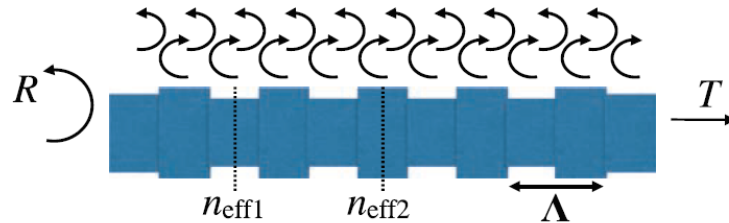
Figure 17: A simple and uniform Bragg grating having a periodic structure. n_{eff1} and n_{eff2} are the lowest and the largest waveguide effective indices, respectively. R and T are the reflection and the transmission. The $180\angle$ arrows show that many reflections occur as the light going through the Bragg grating [7].
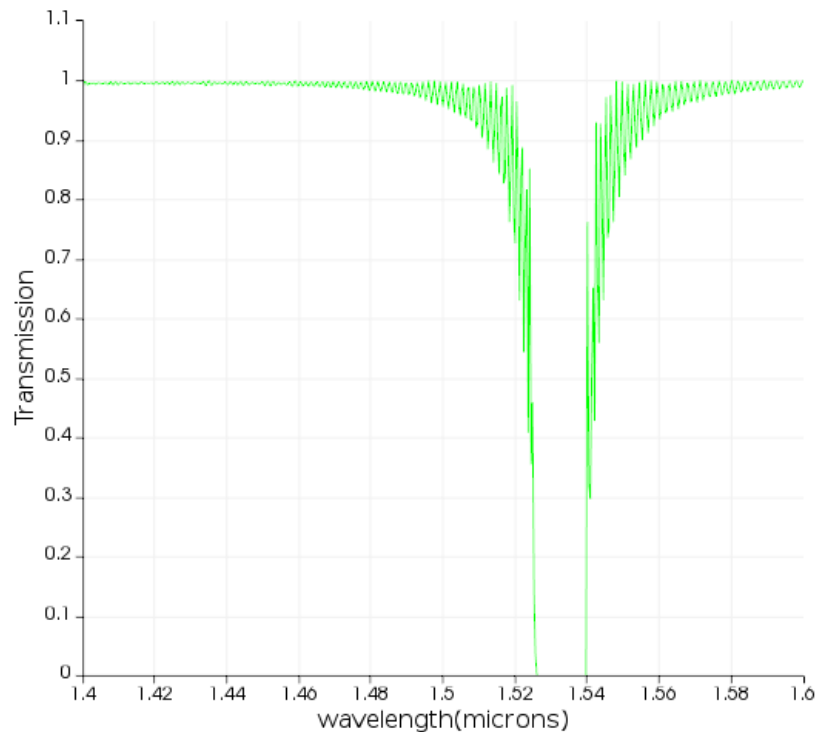
Figure 18: Transmision versus wavelengths. Λ is 500, λ_0 is 1.53 μm.

$$\lambda_B = 2\Lambda n_{eff}$$

(27)

The center wavelength, the Bragg wavelength, can be calculated using Equation 27. In Equation 27, Λ and n_{eff} are the grating period and average effective index. Equation 28 is the reflection coefficient for a Bragg grating with length L [27].

$$r = \frac{-i\kappa \sinh \gamma L}{\gamma \cosh \gamma L + i\Delta\beta \sinh \gamma L}$$

(28)

$$\gamma^2 = \kappa^2 - \Delta\beta^2$$

(29)

In Equation 30, $\Delta\beta$ is the propagation constant offset from the Bragg wavelength, and, in Equation 28, κ is the coupling coefficient for the Bragg grating. κ is the amount of reflection over unit length. Equation 28 can be simplified into $r = -i\tanh \kappa L$ assuming $\Delta\beta = 0$. The peak power of reflection is shown in Equation 31.

$$\Delta\beta = \beta - \beta_0 << \beta_0$$

(30)

$$R_{peak} = \tanh^2 \kappa L$$

(31)

Equation 32 describes the bandwidth of the Bragg grating [27].

$$\Delta\lambda = \frac{\lambda_B^2}{\pi n_g} \sqrt{\kappa^2 + (\pi/L)^2}$$

(32)

For long Bragg gratings ($\kappa \gg \pi$/L), Equations 32 can be simplified into Equation 33.

$$\Delta\lambda = \frac{\lambda_B^2 \cdot \kappa}{\pi n_g}$$

(33)

To consider losses, $\Delta\beta$ is substituted into $\Delta\beta - i\alpha/2$.

A.6.   Integrated Silicon Photonic Chip

In this section, the Integrated Photonic Education Kit (IPEK), including ring resonator, bragg gratings, directional coupler, and mach-zehnder interferometer are dealt with. These devices accept the light from either fiber or the metal for prism coupling using the plasmonic effects and carry the light to a photodetector to detect the light.

Testing of the IPEK and extracting of data were done. Either broadband light source or laser can be used as an input. Optical spectrum analyzer was used to measure output data. Each simulation of the devices is shown in the Appendix.

Figure 4.1 shows broadband and laser source used in this chapter. The broadband source is not a constant number in dBm over the wavelength range, so results deviate from the simulation results as shown in Figure 4.1(a). The laser source is a single wavelength at 1510 nm, as shown in Figure 4.1(b).

A.6.1.   Ring resonators

A ring resonator is included in the IPEK. Data from the ring resoantor was extracted from the ring resonator. The broadband source was used for the ring resonator as an input. The broadband source was coupled to the input port and observed from the through and drop ports, as shown in Figures 4.3 and 4.4. The optical spectrum analayer was used to observe the light. The through

port's central wavelength and optical power are 1498 nm and -57.813 dBm, respectively, as shown in Figure 4.3(a). Figure 4.3(b) is magnified compared to Figure 4.3(a). The drop port's central wavelength and optical power are 1497 nm and -61.256 dBm, respectively, as shown in Figure 4.4(a). Figure 4.4(b) is magnified compared to Figure 4.4(a).

The data from the drop port in Figure 4.4(b) is well matched to the simulation result in Figure 16 in the Appendix. The transmission in Figure 4.4(b) shows sharp edges, which look the same as shown in Figure 16 in the Appendix. The data from the through port shows a contrary shape compared to the data from the drop port.

A.6.2. Bragg gratings

A bragg grating is included in the IPEK. Data was extracted from the bragg grating. The broadband source was used for the bragg grating as an input. Figure 4.6 shows the data from the bragg grating. Contrary to the simulation results in Figure 18 in the Appendix, the results do not show significant contrast between the maximum and minimum transmission. The output port's central wavelength

(a)   (b)
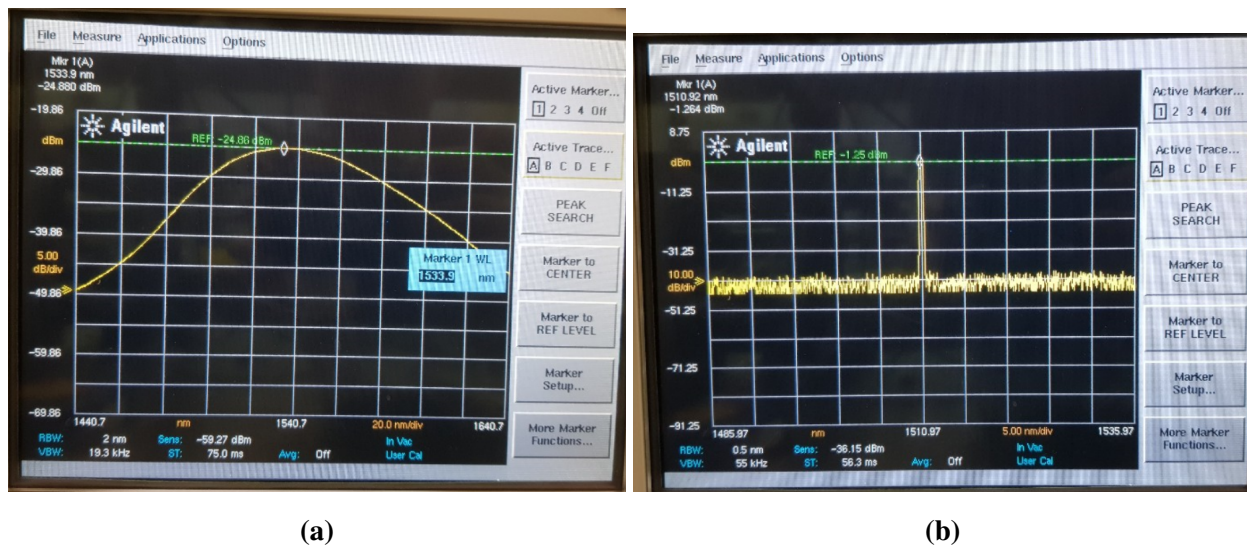
Figure 19: (a) is a Broadband source, and (b) is a laser source.

and optical power are 1498.9 nm and -58.443 dBm, respectively.

The deviation between the data in Figure 4.6 and the simulation results in Figure 18 in the Appendix can be explained by using Figure 4.7. The broadband source did not have high optical power since it was modulated to have a central wavelength of 1510 nm. The output data will have a similar shape shown in Figure 4.7, which has significant contrast between the highest and lowest
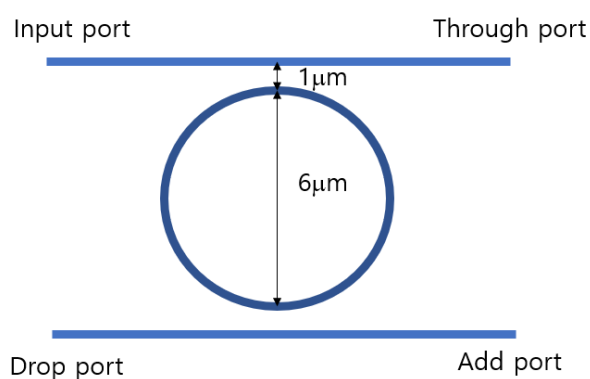
Figure 20: Configuration of the ring resonator in the IPEK. The gap, the ring's diameter, and the waveguide's width are 1 μ*m*, 6 μ*m*, and 1 μ*m*, respectively.

(a)   (b)
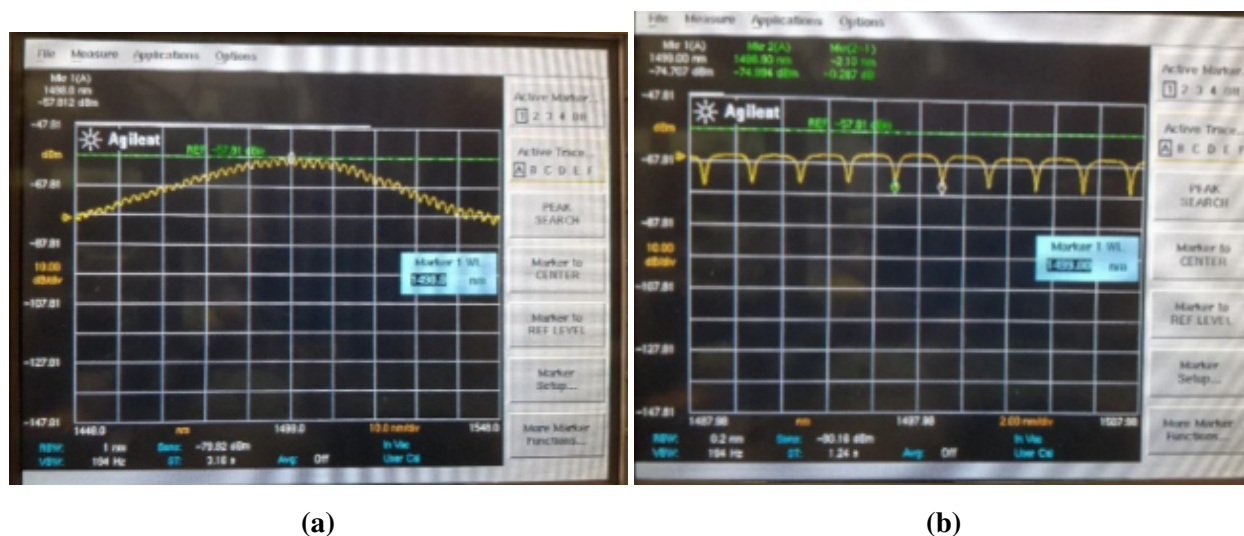
Figure 21: The data was extracted from the through port of the ADD-DROP Ring resonator in the IPEK. The light was coupled to the input port and observed from the through port. The through port's central wavelength and optical power are 1498 nm and -57.813 dBm, respectively. (b) is magnified visually compared to (a).

transmission, assuming high optical power is provided as an input.

A.6.3. Directional coupler

A directional coupler is included in the IPEK. Data from the directional coupler was extracted. The broadband source was coupled to the input port and observed with the output and coupled ports in Figure 4.8. The optical spectrum analyzer was used to observe the coupled and transmitted light.

The output port's central wavelength and optical power are 1497.6 nm and -61.737 dBm, re-
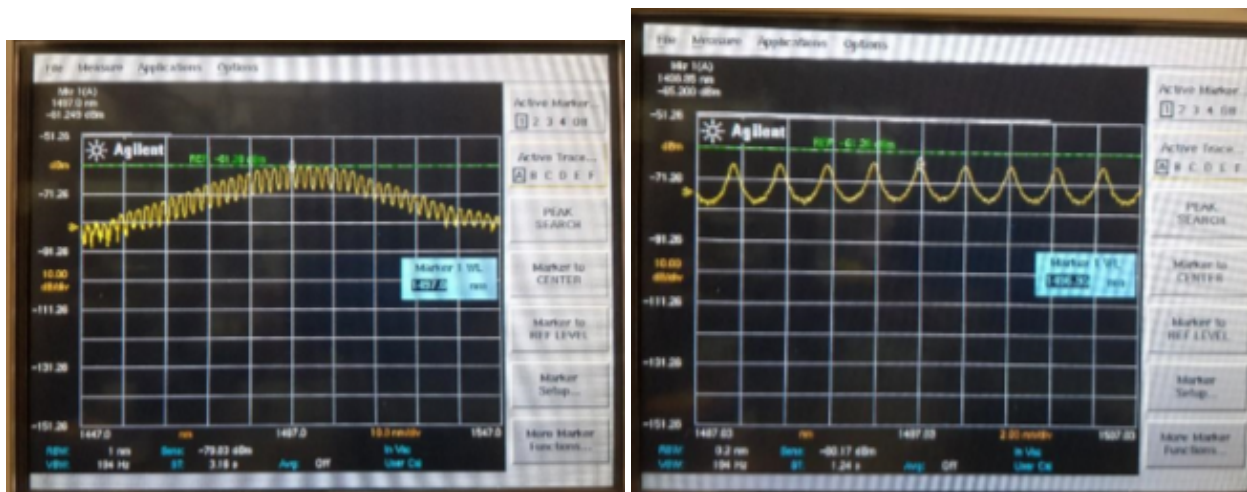
(a)   (b)

Figure 22: The data was extracted from the drop port of the ADD-DROP Ring resonator in the IPEK. The light was coupled to the input port and observed from the drop port. The drop port's central wavelength and optical power are 1497 nm and -61.256 dBm, respectively. (b) is magnified visually compared to (a).
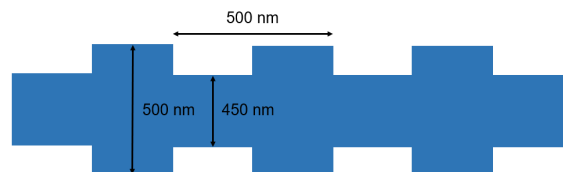
Figure 23: The Bragg grating's configuration in the IPEK. The large width, corrugation width, and grating period are 500 nm, 50 nm, and 500 nm, respectively.

spectively, as shown in Figure 4.9(a). The coupled port's central wavelength and optical power are 1494.4 nm and -60.761 dBm, respectively, as shown in Figure 4.9(b). The sum of the optical power of the output and coupled ports is the input's optical power.
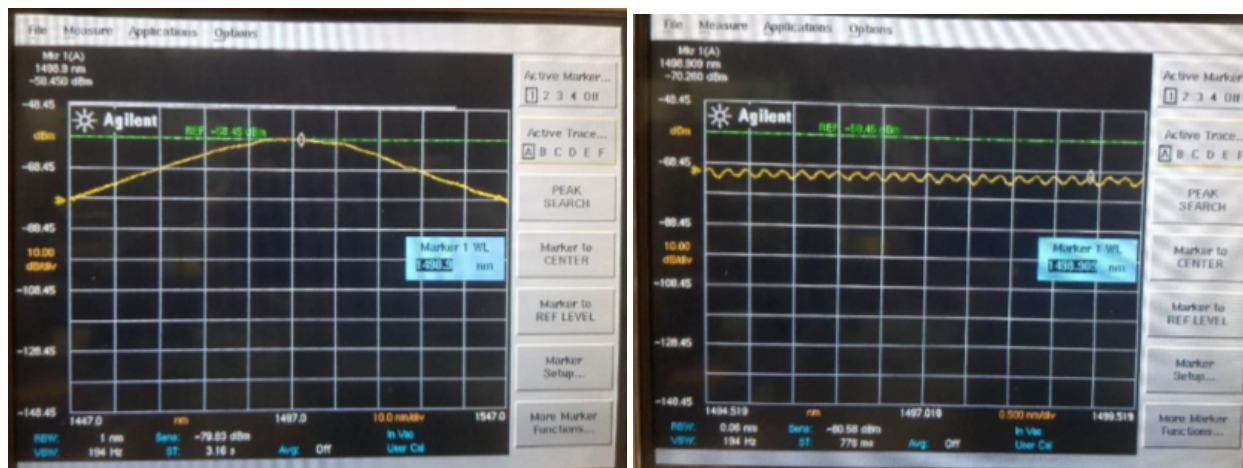
(a)   (b)

Figure 24: The broadband source was used as an input to the Bragg grating, and the output data are shown above. The output port's central wavelength and optical power are 1498.9 nm and -58.443 dBm, respectively. (b) is magnified visually compared to (a).
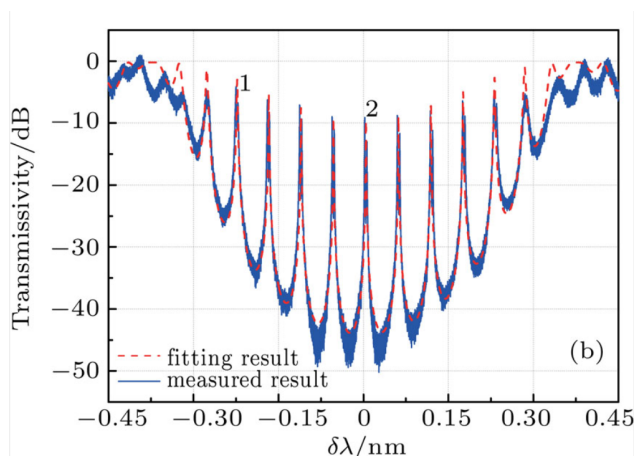
Figure 25: A reference data of a Bragg gratings is shown above [28].

A.6.4. Mach-Zehnder interferometer

A Mach-Zehnder interferometer (MZI) is included in the IPEK. The broadband source was used as an input, coupled to the input port, and observed from the output port, as shown in Figure 4.10. The output port's central wavelength and optical power are 1500.6 nm and -57.802 dBm, respectively,
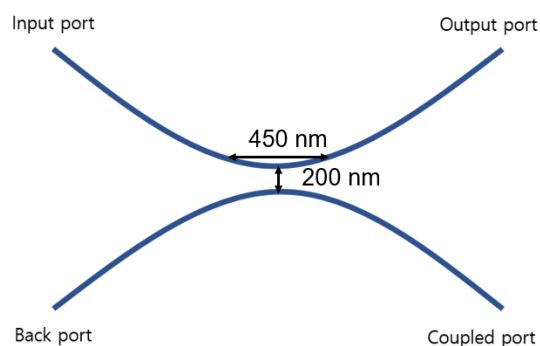
Figure 26: The directional coupler's configuration in the IPEK. The coupler length and gap are 450 nm and 200 nm, respectively.

(a)   (b)
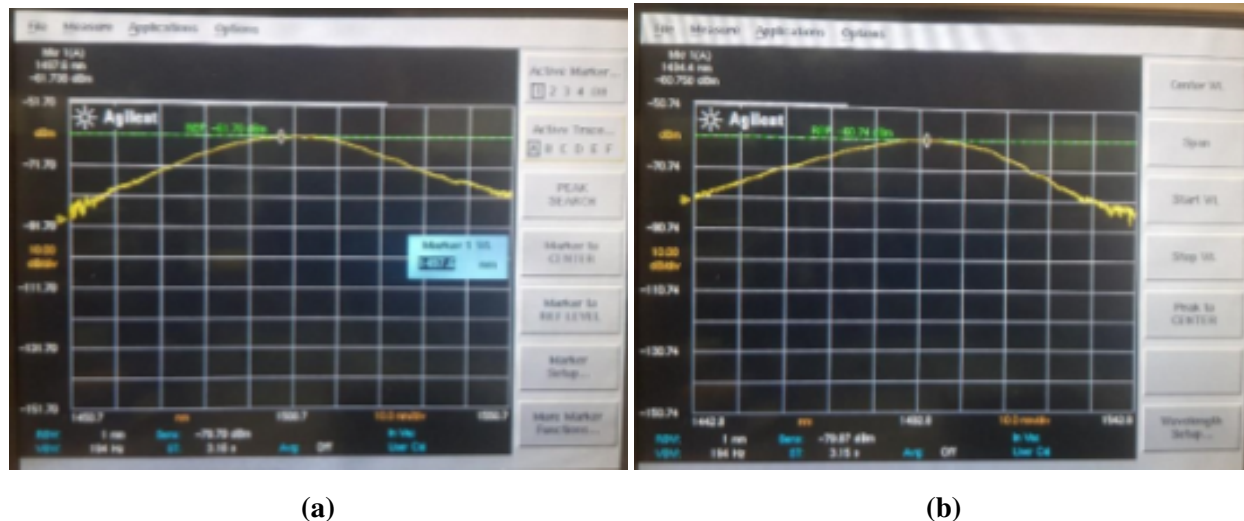
Figure 27: Above figures show the data from the directional coupler. The broadband source was coupled to the input port and observed from the output and coupled ports. (a) The output port's central wavelength and optical power are 1497.6 nm and -61.737 dBm, respectively. (b) The coupled port's central wavelength and optical power are 1494.4 nm and -60.761 dBm, respectively.

as shown in Figure 4.11. The data is well matched to the simulation results in Figure 13 in the Appendix.

The IPEK has a ribbon cable that can adjust the temperature for phase shift by applying a voltage. However, the instruction on the manual was not enough to figure out which port is for voltage and ground for phase shift. If the temperature can be handled, then the data in Figure 4.11 will shift to the right, as shown in Figure 13 in the Appendix.
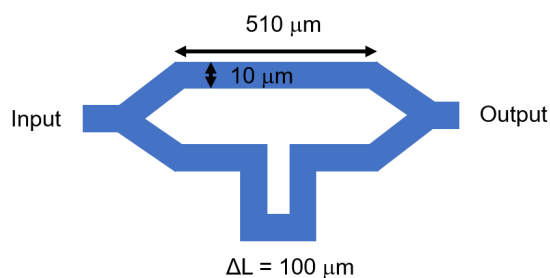
Figure 28: The Mach-Zehnder interferometer's configuration in the IPEK. The upper length, waveguides' width, and length difference are 510 μ*m*, 10 μ*m*, and 100 μ*m*, respectively.
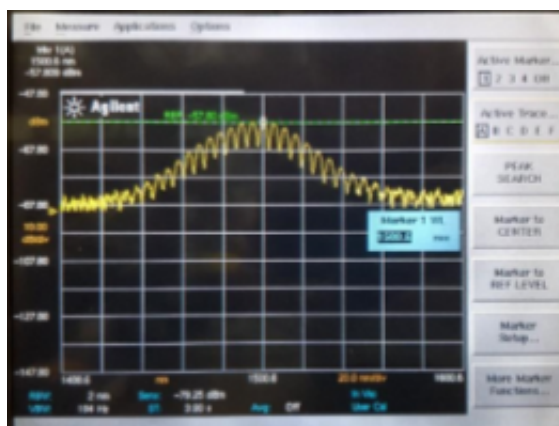
Figure 29: The broadband light was coupled to the input port and observed from the output port. The output port's central wavelength and optical power are 1500.6 nm and -57.802 dBm, respectively.

A.7. Code for Figure 2

```
1   % ////////////////////////////////////////////////////////////
2   % Figure 2.3
3   % ////////////////////////////////////////////////////////////
4
5   new(1);
6   % define wafer and waveguide structure
7   thick_Clad = 2.0e-6;
8   thick_Si = 0.22e-6;
9   thick_BOX = 2.0e-6;
10  #thick_Slab = 0; # for strip waveguides
11  thick_Slab = 0.09e-6; # for strip-loaded ridge waveguides
12  width_ridge = 0.5e-6; # width of the waveguide
13  gap = 100e-9; # Directional coupler gap
14  % define materials
15  material_Clad = "SiO2 (Glass) - Palik";
16  % material_Clad = "H2O (Water) - Palik"; material_Clad = "Air (1)";
17  material_BOX = "SiO2 (Glass) - Palik";
18  material_Si = "Si (Silicon) - Palik";
19  % materials; # run script to add materials
20  % define simulation region
21  width_margin = 2.5e-6; # space to include on the side of the waveguide
22  height_margin = 0.5e-6; # space to include above and below the waveguide
23  % calculate simulation volume
24  % propagation in the x-axis direction; z-axis is wafer-normal
25  Xmin = -2e-6; Xmax = 2e-6; # length of the waveguide
26  Zmin = -height_margin; Zmax = thick_Si + height_margin;
```

```
27  Y_span = 2*width_margin + width_ridge; Ymin = -Y_span/2; Ymax = -Ymin;
28  % draw cladding
29  addrect; set("name","Clad"); set("material", material_Clad);
30  set("y", 0); set("y span", Y_span+1e-6);
31  set("z min", 0); set("z max", thick_Clad);
32  set("x min", Xmin); set("x max", Xmax);
33  set("override mesh order from material database",1);
34  set("mesh order",3); # similar to "send to back", put the cladding as a
        background.
35  set("alpha", 0.05);
36  % draw buried oxide
37  addrect; set("name", "BOX"); set("material", material_BOX);
38  set("x min", Xmin); set("x max", Xmax);
39  set("z min", -thick_BOX); set("z max", 0);
40  set("y", 0); set("y span", Y_span+1e-6);
41  set("alpha", 0.05);
42  % draw silicon wafer
43  addrect; set("name", "Wafer"); set("material", material_Si);
44  set("x min", Xmin); set("x max", Xmax);
45  set("z max", -thick_BOX); set("z min", -thick_BOX-2e-6);
46  set("y", 0); set("y span", Y_span+1e-6);
47  set("alpha", 0.1);
48  % draw waveguide 1
49  addrect; set("name", "waveguide1"); set("material",material_Si);
50  set("y", -width_ridge/2-gap/2); set("y span", width_ridge);
51  set("z min", 0); set("z max", thick_Si);
52  set("x min", Xmin); set("x max", Xmax);
53  % draw waveguide 2
```

```
54  addrect; set("name", "waveguide2"); set("material",material_Si);
55  set("y", width_ridge/2+gap/2); set("y span", width_ridge);
56  set("z min", 0); set("z max", thick_Si);
57  set("x min", Xmin); set("x max", Xmax);
58  % draw slab for strip-loaded ridge waveguides
59  addrect; set("name", "slab"); set("material",material_Si);
60  if (thick_Slab==0) {
61  set("y min", 0); set("y max", 0);
62  } else {
63  set("y", 0); set("y span", Y_span+1e-6);
64  }
65  set("z min", 0); set("z max", thick_Slab);
66  set("x min", Xmin); set("x max", Xmax);
67  set("alpha", 0.2);
```

A.8. Code for Figure 3

```
1  % ////////////////////////////////////////////////////////////
2  % Figure 2.4
3  % ////////////////////////////////////////////////////////////
4
5  % DC_gap.lsf - Calculate directional  c o u p l e r s  gap dependence, Lumerical
        MODE Solutions
6  gap_list =[.1:.1:1]*1e-6; # sweep waveguide width
7  neff = matrix (length(gap_list), N_modes );
8  L_cross= matrix (length(gap_list));
9  for(jj=1:length(gap_list)) {
10 switchtolayout;
11 setnamed("waveguide2","y", -width_ridge/2-gap_list(jj)/2);
12 setnamed("waveguide1","y", width_ridge/2+gap_list(jj)/2);
13 n=findmodes;
14 for (m=1:N_modes) { # extract mode data
15     neff (jj,m) =abs( getdata ("MODE::data::mode"+num2str(m),"neff") );
16 }
17 L_cross(jj) = wavelength / 2 / abs( neff (jj,1)-neff (jj,2));
18 }
19 plot (gap_list*1e9, L_cross*1e6, "Gap [nm]", "Cross-over length [micron]",
        "Cross-over
20 length versus gap");
21 plot (gap_list*1e9, L_cross*1e6, "Gap [nm]", "Cross-over length [micron]",
        "Cross-over
22 length versus gap","logy");
23 matlabsave ("DC_gap", L_cross,neff,gap_list);
```

A.9. Code for Figure 4

```
1  % ///////////////////////////////////////////////////////////
2  % Figure 2.5
3  % ///////////////////////////////////////////////////////////
4
5  % DC_wavelength.lsf - Calculate directional  c o u p l e r s  wavelength
       dependence , Lumerical MODE Solutions
6  wavelength_start =1.5e -6;
7  wavelength_stop =1.6e -6;
8  wavelength_num =5;
9  gap =0.2e -6;
10 switchtolayout ;
11 setnamed ("waveguide2","y", -width_ridge /2-gap /2);
12 setnamed ("waveguide1","y", width_ridge /2+gap /2);
13 setanalysis ("wavelength", wavelength_start );
14 findmodes ;
15 selectmode (1);
16 setanalysis ("track  selected  mode",1);
17 setanalysis ("number of  test  modes",3);
18 setanalysis ("number of  points", wavelength_num );
19 setanalysis ("stop  wavelength", wavelength_stop );
20 frequencysweep ;
21 f=getdata ("frequencysweep","f"); wavelengths =c/f;
22 neff1 = getdata ("frequencysweep","neff");
23 selectmode (2);
24 setanalysis ("track  selected  mode",2);
25 frequencysweep ;
```

```
26  neff2= getdata("frequencysweep","neff");

27  plot(wavelengths*1e6,real(neff1),real(neff2), "Wavelength [micron]", "
        Effective Index","");

28  legend("Symmetric mode","Antisymmetric mode");

29  matlabsave ("DC_wavelength", neff1, neff2,wavelengths);
```

A.10. Code for Figures 7, 8, 9, and 10

```
% ///////////////////////////////////////////////////////////
% Figure 2.8, 2.9, 2.10, and 2.11
% ///////////////////////////////////////////////////////////

% Script to import YBranch GDS into Lumerical MODE or FDTD and simulate
clear;
% perform four simulations:
% 1: splitter
% 2: combiner with one input
% 3: combiner with two inputs in phase
% 4: combiner with two inputs out of phase
for (r=1:4) {
if (r==1) {
SIM_DIRECTION = 1; % 1 = splitter, 2 = combiner
} else {
SIM_DIRECTION = 2; % 1 = splitter, 2 = combiner
}
if (r<3) {
SOURCE2 = 0; % for combiner only. 0 = one source
}
if (r==3) {
SOURCE2 = 1; % for combiner only. 1 = 2nd source in phase
}
if (r==4) {
SOURCE2 = 2; % for combiner only. 2 = 2nd source pi phase
}
```

```
27  newproject ;

28  filename = " YBranch_Compact . gds ";

29  cellname = "y";

30

31  save (" YBranch ");

32  fileout = filebasename ( currentfilename ) + "_Dir" + num2str ( SIM_DIRECTION ) +
        "_Source2_" + num2str ( SOURCE2 );

33  setglobalsource (" wavelength start ",1500e-9);

34  setglobalsource (" wavelength stop ",1600e-9);

35  setglobalmonitor (" frequency points ",100);

36

37  % define materials

38  Material_Clad = " SiO2 ( Glass ) - Palik ";

39  Material_Ox = " SiO2 ( Glass ) - Palik ";

40  Material_Si = "Si ( Silicon ) - Palik ";

41  #materials ; # run script to add materials

42  Thickness_Si =0.22e-6;

43  FDTD_above =200e-9; # Extra simulation volume added

44  FDTD_below =200e-9;

45  minvxWAFER =1e9; minvyWAFER =1e9; maxvxWAFER =-1e9; maxvyWAFER =-1e9;

46  maxvzWAFER = Thickness_Si ;

47

48  n = gdsimport ( filename , cellname , 1, Material_Si , 0, Thickness_Si );

49  if (n==0) { delete ; } else {

50  groupscope (":: model :: GDS_LAYER_1 ");

51  set (" script ","");

52  selectall ;

53  set (" material ", Material_Si );
```

```
54  set("z span", Thickness_Si);

55  set("z",0);

56  selectpartial("poly");

57  minvx=1e9; minvy=1e9; maxvx=-1e9; maxvy=-1e9;

58  for (i=1:getnumber) { # find the extent of this GDS layer.

59  v=get("vertices",i);

60  a=size(v);

61  minvx = min ( [minvx, min( v(1:a(1), 1 ))]);

62  minvy = min ( [minvy, min( v(1:a(1), 2 ))]);

63  maxvx = max ( [maxvx, max( v(1:a(1), 1 ))]);

64  maxvy = max ( [maxvy, max( v(1:a(1), 2 ))]);

65  }

66  minvxWAFER = min ( [minvx, minvxWAFER]); # save the extent of overall
        design.

67  minvyWAFER = min ( [minvy-2.25e-6, minvyWAFER]);

68  maxvxWAFER = max ( [maxvx, maxvxWAFER]);

69  maxvyWAFER = max ( [maxvy+2.25e-6, maxvyWAFER]);

70  groupscope("::model");

71  }

72  % Oxide

73  addrect; set("name", "Oxide");

74  set("x min", minvxWAFER); set("y min", minvyWAFER);

75  set("x max", maxvxWAFER); set("y max", maxvyWAFER);

76  set("z min", -2e-6);

77  set("z max", 0);

78  set("material", Material_Ox);

79  set("alpha",0.2);

80  % Cladding
```

```
81  addrect; set("name", "Cladding");

82  set("x min", minvxWAFER); set("y min", minvyWAFER);

83  set("x max", maxvxWAFER); set("y max", maxvyWAFER);

84  set("z min", 0);

85  set("z max", 2.3e-6);

86  set("material", Material_Clad);

87  set("alpha",0.1);

88  set("override mesh order from material database", 1);

89  set("mesh order", 4); # make the cladding the background, i.e., "send to
        back".

90  if (fileextension(currentfilename) == "lms") {

91  addpropagator;

92  set("x min", minvxWAFER+0.5e-6); set("y min", minvyWAFER+1.5e-6);

93  set("x max", maxvxWAFER-0.5e-6); set("y max", maxvyWAFER-1.5e-6);

94  set("z min", -FDTD_below);

95  set("z max", maxvzWAFER+FDTD_above);

96  set("mesh accuracy", 3);

97  set("x0",-get("x span")/2+0.1e-6);

98  }

99  else {

100 addfdtd;

101 set("x min", minvxWAFER+0.5e-6); set("y min", minvyWAFER+1.5e-6);

102 set("x max", maxvxWAFER-0.5e-6); set("y max", maxvyWAFER-1.5e-6);

103 set("z min", -FDTD_below);

104 set("z max", maxvzWAFER+FDTD_above);

105 set("mesh accuracy", 2);

106 }

107 PointsX=get("mesh cells x");
```

```
108  PointsY=get("mesh cells y");

109  addmovie;

110  set("lock aspect ratio",1);

111  set("horizontal resolution",PointsX*2);

112  set("min sampling per cycle", 2);

113

114  set("name",fileout);

115  addmodeexpansion; set("name", "expansion_v");

116  if (fileextension(currentfilename) == "fsp") {

117  set("monitor type", "2D X-normal");

118  set("y", 0); set("y span",7e-6);

119  set("z min", -FDTD_below); set("z max", maxvzWAFER+FDTD_above);

120  set("mode selection","fundamental TE mode");

121  } else {

122  set("monitor type", "Linear Y");

123  set("y", 0); set("y span",7e-6);

124  set("mode selection","fundamental mode");

125  }

126  set("x", maxvxWAFER-0.6e-6);

127

128

129

130  if (SIM_DIRECTION==1) { # simulate splitter

131  % add mode source:

132  if (fileextension(currentfilename) == "fsp") {

133  addmode;

134  set("z min", -FDTD_below); set("z max", maxvzWAFER+FDTD_above);

135  } else { addmodesource; }
```

```
136  set("name", "source");

137  set("injection axis", "x-axis");

138  set("direction", "forward");

139  set("y", 0e-6); set("y span", 1.5e-6);

140  set("x", minvxWAFER+0.6e-6);

141  updatesourcemode;

142

143  addpower;

144  set("name", "port1");

145  set("monitor type", "2D X-normal");

146  set("y", 2.75e-6); set("y span", 1.4e-6);

147  set("x", maxvxWAFER-0.6e-6);

148

149  if (fileextension(currentfilename) == "fsp") {

150  set("z min", -FDTD_below); set("z max", maxvzWAFER+FDTD_above);

151  }

152  select("expansion_v");

153  setexpansion("expansion_monitor","port1");

154

155  %

156  addpower;

157  set("name", "port2");

158  set("monitor type", "2D X-normal");

159  set("y", -2.75e-6); set("y span", 1.4e-6);

160  set("x", maxvxWAFER-0.6e-6);

161

162

163  %if (fileextension(currentfilename) == "fsp") {
```

```
164  %set("z min", -FDTD_below); set("z max", maxvzWAFER+FDTD_above);
165  %}
166  %select("expansion_v");
167  %setexpansion("expansion_monitor","port2");
168  %
169
170  }
171
172
173  else { % simulate the combiner
174  % add mode source:
175  if (fileextension(currentfilename) == "fsp") {
176  addmode;
177  set("z min", -FDTD_below); set("z max", maxvzWAFER+FDTD_above);
178  } else { addmodesource; }
179  set("name", "source1");
180  set("injection axis", "x-axis");
181  set("direction", "backward");
182  set("y", 2.75e-6); set("y span", 1.4e-6);
183  set("x", maxvxWAFER-0.6e-6);
184  updatesourcemode;
185  if (SOURCE2>0) {
186  if (fileextension(currentfilename) == "fsp") {
187  addmode;
188  set("z min", -FDTD_below); set("z max", maxvzWAFER+FDTD_above);
189  } else { addmodesource; }
190  set("name", "source2");
191  set("injection axis", "x-axis");
```

```
192  set("direction", "backward");

193

194  set("y", -2.75e-6); set("y span", 1.4e-6);

195  set("x", maxvxWAFER-0.6e-6);

196  updatesourcemode;

197  if (SOURCE2==2) { # pi out of phase 2nd source for destructive
         interference

198  set("phase",180);

199  }

200  }

201  addpower;

202  set("name", "port0");

203  set("monitor type", "2D X-normal");

204  set("y", 0e-6); set("y span", 1.5e-6);

205  set("x", minvxWAFER+0.6e-6);

206  if (fileextension(currentfilename) == "fsp") {

207  set("z min", -FDTD_below); set("z max", maxvzWAFER+FDTD_above);

208  }

209  select("expansion_v");

210  setexpansion("expansion_monitor","port0");

211  }

212  addpower; % surface power monitor

213  set("name", "surface");

214  set("monitor type", "2D Z-normal");

215  run;

216

217

218  % Insertion loss vs. wavelength
```

```
219  Port=getresult("expansion_v","expansion for expansion_monitor");

220  wavelengths=c/Port.f;

221  T=Port.T_net;

222  plot(wavelengths*1e6, 10*log10(abs(T)),"Wavelength [micron]","Transmission
         [dB]");

223

224  % Plot field profile in the device

225  x=pinch(getdata("surface","x"));

226  y=pinch(getdata("surface","y"));

227  z=pinch(abs(getdata("surface","Ey")));

228  z=pinch(z,3,50);

229  image(x,y,z);

230  matlabsave(fileout, x,y,z,wavelengths,T);

231  }
```

A.11. Code for Figures 2.3 and 2.4

```
% ////////////////////////////////////////////////////////////
% Figure 2.21 and 2.22
% ////////////////////////////////////////////////////////////

%Make sure the recombination rate parameters found in Step 2 are set.
setnamed('materials::Ge (Germanium)::Ge (Germanium)','recombination.trap
    assisted.active model','Universal Temperature');
setnamed('materials::Ge (Germanium)::Ge (Germanium)','recombination.trap
    assisted.taun.universal temperature.A',1.5e-9);
setnamed('materials::Ge (Germanium)::Ge (Germanium)','recombination.trap
    assisted.taup.universal temperature.A',1.5e-9);
setnamed('CHARGE::boundary conditions::surface_recombination_Ge_SiO2','
    electron velocity',2250); #m/s
setnamed('CHARGE::boundary conditions::surface_recombination_Ge_SiO2','
    enable temperature model',true);
setnamed('CHARGE::boundary conditions::surface_recombination_Ge_SiO2','
    electron eta',-3.8);

%Enable optical generation rate object   gen    and set power scale
    factor to give around 1 mA short circuit current
%(remember that the optical generation rate from FDTD was normalized to 1
    W). This object already has generation
%data imported from file vertical_photodetector_generation.mat:
setnamed('CHARGE::gen','enabled',true);
setnamed('CHARGE::gen','scale factor',1.2e-3);

```

```matlab
%In    anode    object set reverse bias sweep:
setnamed('CHARGE::boundary conditions::anode','sweep type','range');
setnamed('CHARGE::boundary conditions::anode','range start',0.25);
setnamed('CHARGE::boundary conditions::anode','range stop',-2);
setnamed('CHARGE::boundary conditions::anode','range num points',26);

% ////////////////////////////////////////////////////////////
% Different code from above
% ////////////////////////////////////////////////////////////

Pin=1.2e-3; # Watts
I=-2*getdata("CHARGE", "anode.I");
I_norm=I/max(I);
V=linspace(-0.25,2,26);
Resp=I/Pin;
plot(V,I_norm,"photo detector bias voltage(v)","I_(photo,norm)=I_(photo)/
    I_(norm)   a.u ");
plot(V,Resp,"photo detector bias voltage(v)","Responsivity (A/W) ");
```

A.12. Code for Figures 2.5 and 2.6

```
1  % ////////////////////////////////////////////////////////////////
2  % Figure 2.23 and 2.24
3  % ////////////////////////////////////////////////////////////////
4
5  basefilename = "Photodetector Responsivity lateral photodetector -
       constant doping.ldev";
6
7  Iss=getdata("CHARGE", "ac_cathode.dI");
8  Vdc=getdata("CHARGE", "ac_cathode.V_anode");
9  Iss=pinch(Iss);
10 f=getdata("CHARGE", "ac_cathode.f");
11 N= length(f);
12 three_dB=f>0;
13 three_dB=three_dB*0.001;
14 plot(1e-9*f,log10(three_dB));
15 holdon;
16 leg = cell(2);
17 leg{1} = "3 dB threshold";
18 fInterp = f(1):1./1e-8:f(length(f)); #0.1GHz grid
19 bias = zeros(1);
20 f3dB = zeros(1);
21 counter = 1;
22 for(i=3;i<=size(Iss,1);i=i+1){#just last DC point
23     IssInterp = interp(Iss(i,:),f,fInterp);
24     bias(counter) = Vdc(i);
25     f3dB(counter) = 1e-9*fInterp(find(20*log10(abs(IssInterp)/max(abs(
```

```
            IssInterp))),-3));
26      freq = f*1e-9;
27      norm_resp = 20*log10(abs(Iss(i,:))/max(abs(Iss(i,:))));
28      savedata(basefilename+"_norm_resp_vs_freq_"+num2str(counter)+".ldf",
            freq,norm_resp);
29      plot(1e-9*f,20*log10(abs(Iss(i,:))/abs(Iss(i,1))));
30      leg{counter+1} = num2str(Vdc(i))+"V";
31      counter = counter + 1;
32  }
33  setplot("x label","Frequency (GHz)");
34  setplot("y label","Normalized response (dB)");
35  setplot("log10x",true);
36
37
38  legend(leg);
39
40  bandwidth = f3dB;
41  savedata(basefilename+"_bandwidth_vs_bias.ldf",bias,bandwidth);
```

A.13. Code for Figures 2.8 and 2.9

```
1   % ////////////////////////////////////////////////////////////
2   % Figure 2.26 and 2.27
3   % ////////////////////////////////////////////////////////////
4
5
6
7   %read sweep results
8
9   T= (getsweepdata("life_time","T")-273.15);
10
11  I=2*(getsweepdata("life_time","I"))*1e6;
12
13
14  err=zeros(3,3,3); #error matrix
15
16  %reference data
17
18  refdataT = 24.5:9.5:85;
19
20  refdataIuA = [0.3, 0.53, 0.8, 1.3, 2.08, 3.3, 5];
21
22  refdataIuA_interp=interp(refdataIuA,refdataT,T);
23
24  %Calculate error for each sweep compared to reference data
25
26  for(i=1:3){
```

```matlab
    for(j=1:3){

        for(k=1:3){

            for(l=1:5){

            err(k,j,i)=err(k,j,i)+abs(I(l,k,j,i)-refdataIuA_interp(l,1));

        }   }

    }

}


%find the sweep with minimum error compared to reference


minimum=min(err);


index=find(err,minimum);


matrix_size = size(err);


indices = matrix(length(matrix_size));




for (i = 1:length(matrix_size)) {


 mod_dividend = index;


 mod_divisor = matrix_size(i);


 mod_remainder = mod(mod_dividend,mod_divisor);

```

```matlab
55
56
57  if (mod_remainder == 0) { mod_remainder = matrix_size(i); }
58
59  indices(i) = mod_remainder;
60
61
62
63  index = (index+(matrix_size(i)-mod_remainder))/matrix_size(i);
64
65  }
66
67  %plot the sweep with minimum error
68
69  plot(T,I(:,indices(1),indices(2),indices(3)),refdataIuA_interp,"
        Temperature in degrees Celsius", "Dark current in uA at V=-1(v)","",".
        log10y");
70  legend("DEVICE simulation","Reference, p+ Si w/ anneal");
71
72  %find paramater values for the sweep with minimum error
73
74  load(pwd+"/Revision 3_life_time/"+"life_time_"+num2str(indices(3))+"
        Ge_SiO2_velocity_"+num2str(indices(2))+"Ge_SiO2_eta_"+num2str(indices
        (1))+"Temperature_1.ldev");
75
76  ?"eta="+num2str(getnamed("::model::CHARGE::boundary conditions::
        surface_recombination_Ge_SiO2","hole eta"));
77  ?"surface recombination velocity="+num2str(getnamed("::model::CHARGE::
```

```
    boundary conditions::surface_recombination_Ge_SiO2","hole velocity")

    *100)+" cm/s";

78  ?"tau="+num2str(getnamed("::model::materials::Ge (Germanium)::Ge (

    Germanium)","recombination.trap assisted.taup.universal temperature.A")

    )+" s";
```